Measurements of Protein Folding/Misfolding using Pulsed Electron Spin Resonance

by

Sangmi Jun

B.S., Hanyang University, KOREA, 2000

M.S., Hanyang University, KOREA, 2002

Submitted to the Graduate Faculty of

School of Arts and Sciences in partial fulfillment

of the requirements for the degree of

Doctor of Philosophy

University of Pittsburgh

2009

UNIVERSITY OF PITTSBURGH

FACULTY OF ARTS AND SCIENCES

This dissertation was presented

by

Sangmi Jun

It was defended on

December 9th, 2009

and approved by

David Waldeck, PhD., Professor, Department of Chemistry, Faculty of Arts and Sciences

Craig Wilcox, PhD., Professor, Department of Chemistry, Faculty of Arts and Sciences

Gordon S. Rule, PhD., Professor, Department of Biological Sciences and Chemistry, Mellon College of Science, Carnegie Mellon University

Dissertation Advisor: Sunil Saxena, PhD., Associate Professor, Department of Chemistry, Faculty of Arts and Sciences

Measurements of Protein Folding/Misfolding using Pulsed Electron Spin Resonance

Sangmi Jun, PhD

University of Pittsburgh, 2009

We describe a new electron spin resonance (ESR) method that measures interspin distances at *physiological conditions*. The method is used to examine the melting of a polyalanine peptide, which is of considerable current interest in the field of protein folding. One end of the peptide is tagged with a Cu(II) ion and the other with a nitroxide spin label. The rapidly relaxing electron spin, Cu(II), enhances the electron spin flip rate of the nitroxide. This change in the relaxation rate depends on the interspin distance, *r*. As the peptide unfolds, the interspin distance changes. The ESR determined interspin distance decreases from the folded to unfolded state whereas the MD simulation shows an increased distance of the peptide in the PPII geometry. Therefore, the ESR results indicate that the polyalanine peptide does not melt into an *extended* PPII structure in the unfolded state. The ESR results also show that the change in interspin distances is clearly in concordance with the change in helicity and demonstrates an important application of the pulsed ESR method to monitor unfolding transition at physiological temperatures in biomolecules.

In the second part of this research, the local environment of the Cu(II) ion in amyloid-β peptide (Aβ) is investigated by electron spin echo envelope modulation ESR spectroscopy. The aggregation of Aβ is implicated in the pathogenesis of Alzheimer's disease. Distinct differences in coordination of Cu(II) to Aβ are observed as the Cu(II) concentration increases. The overall morphology of Aβ aggregates, shown by transmission electron microscopy and atomic force microscopy images, also depends on the Cu(II) concentration. At low concentration of Cu(II),

Aβ fibrils are observed and Cu(II) is coordinated by N-terminal histidine residues. As the concentration of Cu(II) increases, the images suggest a significant increase in the proportion of granular amorphous aggregates, and ESR spectra indicate a second copper-binding site that exists in a proton-rich environment. The results strongly suggest that the misfolding mechanism of Aβ depends on the Cu(II) concentration. This research significantly enhances our understanding of the misfolding mechanism in Aβ, and elucidates the relationship between the microscopic Cu(II)-Aβ interaction and macroscopic structure.

TABLE OF CONTENTS

LIST OF TABLES

LIST OF FIGURES

PREFACE

First of all, I would like to express my sincere gratitude to my advisor, Professor Sunil Saxena. Without his advice and unique support this thesis would never had become a reality. He always showed such confidence in my ability and encouraged me to perform to the best of my abilities and supported me with his endless patience throughout my graduate research. It was a great pleasure to have a chance to work with him.

I also would like to thank all my past and present group members – Dr. Marco Bonora, Jim Becker, Andrey Tataurov, Dr. Ronny Rocha Ribeiro, Dr. Soraya Pornsuwan, Dr. Katherine Stone, Zhongyu Yang, Jessica Sarver, Byong-kyu Shin, Ming Ji, Dr. Sharon Ruthstein, Gayathri Rajapakse, Kulakulasooriyagei Ishara Silva, and Timothy Cunningham. We were more of a family rather than a research group. I cannot forget the great times that we shared in the Saxena group.

It is an honor to have Professor David Waldeck, Professor Craig Wilcox, and Professor Gordon S. Rule on my dissertation committee. I am deeply grateful to them for reading my thesis and giving me advice despite their busy schedules.

I am truly indebted to my parents in Korea and my friends in the Pittsburgh Korean community for their endless love and encouragement. Finally, I really love my husband, Yushin Kim and my son, Isaac Seongmin Kim and thank them for all their kinds of support for my entire life.

1.0 INTRODUCTION

Electron spin resonance (ESR) spectroscopy is a powerful technique that can resolve structural details as well as conformational dynamics of molecules with unpaired electrons. Since E. K. Zavoisky first developed the ESR technique in 1945 (*1, 2*), ESR has been applied to study free radicals, compounds with transition metal ions, and defect centers. For two decades, site-directed spin labeling (SDSL) has facilitated the use of ESR to investigate biological molecules (*3-8*). Using SDSL, spin labels (typically nitroxides) can be placed at virtually *any* position on a protein. In pioneering papers, Hubbell and co-workers have shown the utility of SDSL to measure the structural changes associated with function and conformational dynamics in proteins including many membrane proteins (*5, 9-12*). Recently, new Fourier Transform (FT) ESR methods in combination with SDSL have provided a unique capability for determining the interspin distances in the ~ 20-70 Å range (*8, 13-18*). These robust methods are sensitive to weak electron-electron dipolar interaction and measure interspin distances directly. However, they are applicable only at low temperatures (~ 80 K). We, therefore, developed a new ESR method based on spin-relaxation in order to measure distances between Cu(II) and nitroxide under physiological conditions. This ESR approach promises to directly resolve structural changes associated with protein folding/unfolding at any temperature. Details of these results appear in Chapter 2. Furthermore, we examined detailed information on the local environment of the Cu(II) ion in amyloid-β peptide (Aβ), and the relationship between microscopic metal ion-

peptide interaction and aggregate structure. These results are the foci of Chapters 3 and 4. The results are significant for understanding the Cu(II) concentration dependent Aβ misfolding mechanism and clearly demonstrate that the microscopic Cu(II)-Aβ interaction plays a major role in dictating the aggregated state of Aβ. In the following sections, we provide a general background on the spin labeling as well as key ESR methods that have been extensively used in this thesis.

1.1 SITE-DIRECTED SPIN LABELING

Electron spin resonance (ESR) on biomolecules has been enabled by *Site-directed spin labeling (SDSL)* (*3, 5-8*). In SDSL, a native amino acid is replaced with cysteine by site-directed mutagenesis, and a nitroxide side chain is attached to the site via a disulfide linkage. A common spin-label used for ESR experiments with proteins is (1-oxyl-2,2,5,5,-tetramethylpyrroline-3-methyl)-methanethiosulfonate spin label, which is called MTSSL. Figure 1-1 shows the reaction by which the label is attached to the cysteine residue.

The spin label (MTSSL) is very stable in solution. Hubbell and co-workers showed that it typically results in minimal perturbation in structure or function (*9, 11*). They also have shown the utility of SDSL to measure the structural changes associated with function in bacteriorhodopsin, determination of membrane protein topography, measurement of the electrostatic potential at precise position on a membrane protein, determination of the orientations and movements of individual segments of membrane proteins, and the large amplitude domain motions of the T4 lysozyme (*5, 9-12*).

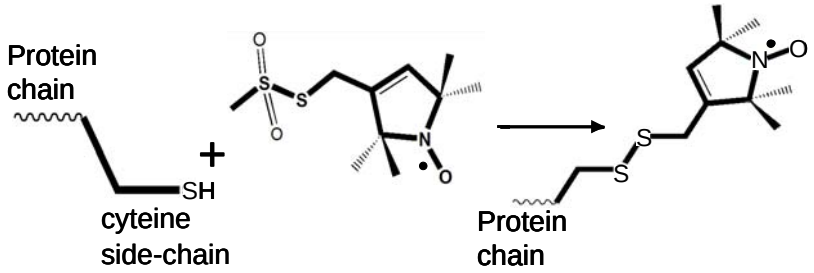

Figure 1-1: The spin-labeling reaction. (1-oxyl-2,2,5,5,-tetramethylpyrroline-3-methyl)-methanethiosulfonate spin label (MTSSL) attaches to the cysteine side chain.

1.2 ESR DISTANCE MEASUREMENTS

In recent years, there has been a significant interest in the measurement of protein structure and structural changes associated with function by ESR. For this purpose, measurements of distances between specific sites provide valuable constraints.

• *ESR methods for distance measurements*

Electron spin resonance (ESR) on biomolecules has been enabled by SDSL (*3, 5-8*) and one of the most useful aspects of SDSL is the ability to measure interspin distance between two nitroxide side chains. *Continuous Wave (CW) ESR* can measure distances between two nitroxide spin labels in the range of 8 ~ 25 Å on proteins. The magnetic dipolar interaction between two spin labels results in a small local magnetic field, which makes the spectrum of doubly spin labeled protein broader than the CW spectrum of the singly spin labeled protein. By calibrating the excess linewidth of the doubly spin labeled sample, the interspin distance and the distribution in distance are determined (*15, 18, 19*).

New Fourier Transform (FT) ESR methods, such as double electron-electron resonance (DEER) and double quantum coherence (DQC) ESR experiments, extract weak dipole-dipole interaction between two paramagnetic centers from other contributions in order to measure the interspin distances in the 20 ~ 70 Å range (*8, 13-18*). After Fourier Transform (FT) of the time domain signal from DEER and DQC methods, they contain frequencies at :

$$\omega_{12} = \frac{\kappa}{r_{12}^{3}}\left(3\cos^2\theta - 1\right) \qquad (1\text{-}1)$$

$$\text{where } \kappa = \frac{\mu_o g_1 g_2 \beta_e^{\,2}}{4\pi\hbar}$$

where ω_{12} is the splitting frequency; the subscripts *1* and *2* express the electron spin of the first and second nitroxides, respectively; μ_o is permittivity of vacuum; g is g- factor; β_e is the Bohr magneton; r_{12} is the distance between the *1* and *2* spins, and θ is the angle between the interspin vector and the external magnetic field, B_0 (*19*) (Figure 1-2). In a frozen sample, all orientations are spanned. Each orientation θ leads to a "peak" at a specific frequency in the spectrum. For example, the frequency for the case of θ = 0°, 45°, or 90° is at $\frac{2\kappa}{r_{12}^{3}}$, $\frac{\kappa}{r_{12}^{3}}$, or $\frac{-\kappa}{r_{12}^{3}}$, respectively. The intensity of each "peak" depends on the number of molecules of that orientation. The probability of being at a given orientations is sin(θ) [0° < θ < 90°]. Therefore, the highest intensity peak appears at θ = 90° where sin(θ) is a maximum. As a result, a characteristic shape called the *"Pake pattern"* is obtained (*19*). Figure 1-3 illustrates this Pake pattern. The Pake pattern can be inverted to obtain the distance distribution.

The *four-pulse DEER experiment* uses two different frequencies for extracting the dipolar interaction between two spins. Two frequencies excite the spins in two different parts of the spectrum represented as 'spin *1*' and 'spin *2*'. Pulses at one frequency excite the 'spin *1*' and generate an echo in the usual way. A π pulse at the second frequency is needed to excite 'spin *2*' and thus inversion of the 'spin *2*' reverses the local dipolar field felt by the 'spin *1*'. By stepping out the π pulse at the second frequency, the echo amplitude is modulated by a period that depends on the magnitude of the dipolar interaction. After Fourier Transform (FT) of the DEER signal, a Pake pattern is obtained.

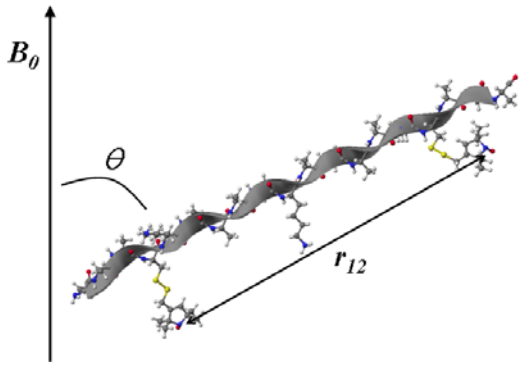

Figure 1-2: Description of the interspin distance, r_{12}, between two spins and the angle, θ, between the interspin vector and the external magnetic field.

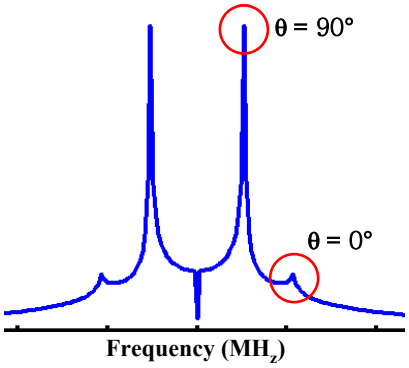

Figure 1-3: Pake pattern. The high and low intensity peaks correspond to θ = 90°and θ = 0°, respectively.

Another pulse ESR method, *DQC,* was developed by Freed and co-workers (*16, 20, 21*). A DQC experiment is based on the double quantum coherence in spin-spin interaction. The strength of the dipolar interaction between electron spins is related to the rate of formation of the DQC, and it provides the sensitivity to interspin distance. DQC uses a six pulse sequence, and an appropriate phase cycling can separate the double quantum coherence pathway from all other pathways. Fourier Transform of a time domain signal also produces the Pake pattern *(22)*.

Both the DEER and DQC methods are very novel methods for distance measurement. They are sensitive to weak spin-spin interactions and can measure interspin distances between two paramagnetic centers directly. These distance measurement methods have emerged as powerful techniques for determination of structure-function relationships in macromolecular systems (*8, 14, 16-18, 23-25*). However, these robust methods are applicable *at low temperatures (usually ≤ 80 K).* In Chapter 2, we describe one method that can remove this limitation so that a different class of phenomenon (e.g., protein folding) may be investigated.

• *Inversion recovery to measure the longitudinal relaxation time (T_1)*

To remove the limitation of working on frozen samples, one has to move away from examining the coherent effects of dipolar interaction, and instead rely on another effect. The presence of the second spin can enhance the relaxation of the first spin in a fashion that depends on distance. The effect is most dramatic when the second spin is a fast relaxing spin. Since, transition metals, such as Mn(II), Fe(III) and Cu(II), usually have a much shorter longitudinal relaxation time than the nitroxyl radical, the fast relaxing metal spin can enhance the rate of the relaxation of the more slowly relaxing nitroxide spin (*26-28*). The longitudinal relaxation time of the nitroxide in the presence and absence of the metal is measured by using an inversion

recovery experiment and the change in the relaxation rate of the nitroxide depends on r^{-6}, where r is the distance between the metal and nitroxyl spin.

The change in T_1 can be measured by the *Inversion recovery* technique (*29*). The pulse sequence and the magnetization diagram are shown in Figure 1-4 (left). The pulse sequence consists of two pulses separated by an interval t_1. At equilibrium, the net magnetization vector, M_0, lies along the direction of the applied magnetic field, B_0. In this configuration, the z-component of magnetization M_z equals M_0. The first pulse in the sequence is a π pulse and it inverts the z-magnetization. T_1 relaxation occurs during the time interval t_1, which is stepped in the experiment. Before the –z-magnetization goes to equilibrium, the second $\pi/2$ pulse is applied to rotate the remaining z-magnetization into the xy-plane. Once the magnetization is present in the xy-plane, it precesses about the z-axis and dephases giving a signal called a Free-Induction Decay (FID).

Figures 1-5a and b show the spectral data for the inversion recovery spectrum from the alanine-based peptide with a paramagnetic metal, Cu(II). The "v" dimension is the continuous wave (CW) equivalent spectral dimension and the "t_1" dimension illustrates the recovery of magnetization to equilibrium after inversion with a π pulse. This is illustrated more clearly by extracting a slice parallel to "t_1" from the 2-D data set.

In general, this recovery is related to the electron-spin-flip rate (W_e) and nuclear-spin-flip rate (W_N). For full irradiation, the signal in the inversion recovery experiment recovers with a single exponential and the recovery time $T_1 = (2W_e)^{-1}$ since the entire ESR spectrum is excited by the pulse. However, for partial irradiation, the recovery depends on both W_e and W_N. In this case, only a small part of the ESR spectrum is excited. During the longitudinal relaxation process,

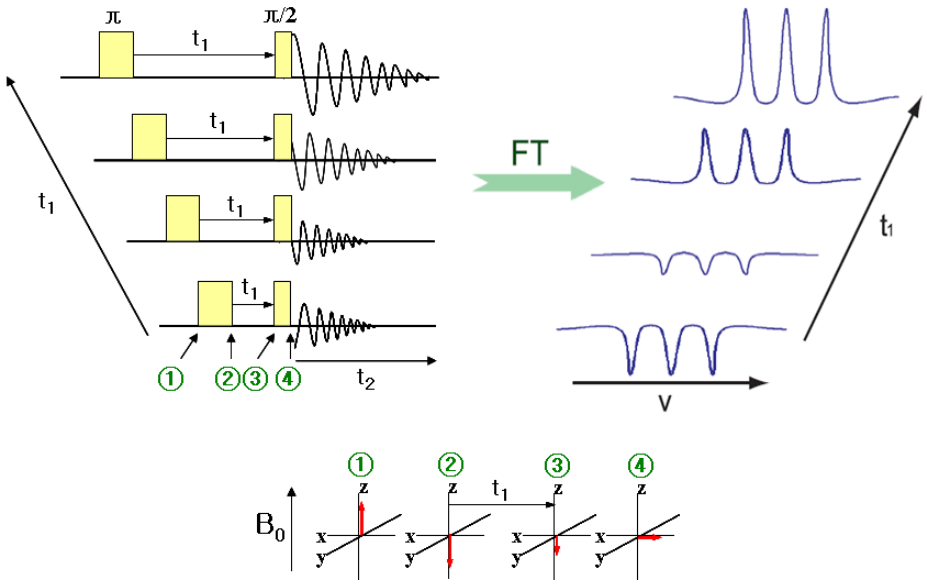

Figure 1-4: Inversion recovery pulse sequence (π and $\pi/2$ pulses) and the magnetization diagram. In the experiment, the time interval t_1 is stepped. The time domain signal is acquired with the time t_2 (left) and the frequency domain spectrum is acquired after Fourier Transform (right).

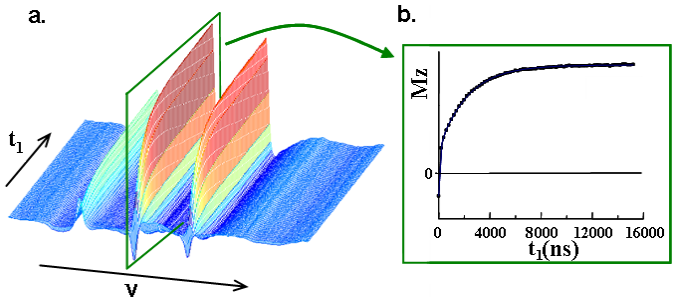

Figure 1-5: (a) Spectral data after FT of FID and (b) Trajectory of the M_z as a function of t_1 in the inversion recovery experiment. The recovery curve was fitted to a bi-exponential form.

nuclear-spin-flip can occur and this leads to the precessional frequencies of electron-spin to shift to frequencies outside the irradiated region. Some spins that undergo nuclear-spin-flips are no longer detectable. Consequently, the effect of partial irradiation is a faster recovery and experimental curves should be fitted with bi-exponential form for extracting T_1.

The equation governing this behavior as a function of the time t_1 is (*30*)

$$S(t_1) = A + B\exp(-2W_e t_1) + C\exp[-t_1 / T_A(\tau)] \qquad (1\text{-}2)$$

where $S(t_1)$ is the signal from the inversion recovery experiment; $T_1 = (2W_e)^{-1}$, and T_A depends upon a rotational correlation time, τ. The first time constant, T_1 is related to electron-spin-flips that we want to measure and the second one, T_A reflects the other relaxation pathways. Schwartz and co-workers found that T_A (τ) decreases from the slow motional regime to the fast motional regime, and finally T_A (τ) becomes constant in the fast motional regime (*31*).

• *Distance measurements using T_1 at room temperature*

A fast relaxing metal spin causes change in T_1 of slowly relaxing nitroxide spin. The effect of metal ion on the relaxation rate for a nitroxide can be described by Kulikov and Likhtenshtein (*26-28*), based on Bloembergen theory (*32-34*).

$$\frac{1}{T_{1s}} = \frac{1}{T_{1s}^{\,0}} + S(S+1)\times\left[\frac{b^2 T_{2f}}{1+(\omega_f-\omega_s)^2 T_{2f}^{\,2}} + \frac{c^2 T_{1f}}{1+\omega_s^{\,2} T_{1f}^{\,2}} + \frac{e^2 T_{2f}}{1+(\omega_f+\omega_s)^2 T_{2f}^{\,2}}\right] \qquad (1\text{-}3)$$

$$b^2 = \frac{1}{6} g_s^{\,2} g_f^{\,2} \beta_e^{\,4} \frac{(1-3\cos^2\theta)^2}{\hbar^2 r^6}$$

$$c^2 = 3g_s{}^2 g_f{}^2 \beta_e{}^4 \frac{\sin^2\theta\cos^2\theta}{\hbar^2 r^6}$$

$$e^2 = \frac{3}{2} g_s{}^2 g_f{}^2 \beta_e{}^4 \frac{\sin^4\theta}{\hbar^2 r^6}$$

where *f* and *s* denote the fast- and slowly-relaxing spins, respectively; $T_{1s}{}^0$ is T_1 for the slowly-relaxing spin in the absence of spin-spin interaction; T_{1s} is T_1 for the slowly-relaxing spin perturbed by the fast-relaxing spin; T_{1f} is the metal longitudinal relaxation time and T_{2f} is the metal transverse relaxation time. Usually for rapid relaxation of the metal ions, $T_{1f} = T_{2f} = T_f$. *S* is the electron spin on the faster-relaxing center; ω_f and ω_s are the resonant frequencies for the fast- and slowly-relaxing spins, respectively; g_f and g_s are the *g* factors for the fast- and slowly-relaxing spins, respectively; β_e is the Bohr magneton; *r* is the interspin distance between two spins, and θ is the angle between the interspin distance vector and the external magnetic field, B_0.

Kulikov and Likhtenshtein originally used this approach and determined the distance between a spin of a radical and a paramagnetic center by using the change of T_1 of the radical at low temperature (*26, 28*). The relaxation time for metal spins, which is usually short, can be measured only at low temperatures. Also, a long dead time and pulse length were limitations in performing the experiment at physiological conditions. Eaton and co-workers continued methodological development and determined interspin distances between a metal center and nitroxide such as iron [Fe(III)] – nitroxyl radical for complexes of metmyoglobin variants and methemoglobin (*35-37*). Their work also used the effect of a rapidly relaxing metal on the longitudinal relaxation rate for nitroxyl spin labels at low temperature.

In Chapter 2, we utilize the inversion recovery to develop a new method for measuring interspin distances between copper ion [Cu(II)] and nitroxide in small peptides under

physiological conditions. In order to perform the inversion recovery experiment at room temperature, short (~ 4 ~ 6 ns) and high power (~ kW) pulses that can substantially invert the entire bandwidth of the ESR spectrum are required. This challenge has been meet only recently.

Another important condition for determining the relaxation time at room temperature is achieving a short dead time (≤ 50 ns). When the experimental temperature is close to room temperature, the ESR signal decays very rapidly (10 ~ 100 ns) and the intense first part of the signal decaying is obstructed by the ring-down of the pulse. Until recently, it was not possible to get the free induction decay (FID) and measure the relaxation time at room temperature with a long dead time such as 200 ns in Eaton's works. A short dead time of 20 ~ 30 ns was achieved by Freed and co-workers with a home-built spectrometer (*38-42*). Saxena and co-workers also combined two approaches that modified the phase cycles in order to minimize the ring-down artifacts and reduce the dead time to as much as 20 ns (*43*). They obtained Correlation Spectroscopy (COSY) spectra over the entire motional regime (from 192 K to 310 K) and determined a phase memory time, as low as 20 ns for a nitroxide spin label. These results enable us to use the inversion recovery sequence at ambient temperatures.

Based on these developments, we demonstrate that the inversion recovery experiment is useful for measuring longitudinal relaxation time, T_1, at room temperature in Chapter 2. This development should allow us to determine interspin distances at each step of the folding pathway of peptides to shed light on the molecular determinants of protein folding.

1.3 CHARACTERIZATION OF METAL CENTERS BY ESR

Another important application of ESR is the determination of the local environment of the metal ion in biological systems. Electron spin echo envelope modulation (ESEEM) ESR spectroscopy is a powerful technique for probing the coordination environment of paramagnetic metal sites in proteins. In Chapters 3 and 4, we exploit ESEEM to shed light on the identification of the Cu(II) binding site in different aggregated states of amyloid-β (Aβ) peptide. The Cu(II) ion is a paramagnetic metal, which has a d^9 electron configuration. The ligands of Cu(II) ion are usually arranged in an octahedral environment with four equatorially coordinated ligands and two axially coordinated ligands. The axial ligands are much more weakly bound to Cu(II) than those in the plane.

In order to characterize the copper binding site, CW-ESR and electron spin echo envelope modulation (ESEEM) spectroscopy are performed. Figure 1-6 shows the coordination environments that can be probed with (a) CW-ESR and (b) ESEEM spectroscopy, respectively (*44*). CW-ESR measures strong interactions such as the hyperfine interaction of an electron spin with the Cu(II) nuclei. These interactions are sensitive to the nature of the directly coordinated nuclei [Figure 1-6(a), blue region]. On the other hand, ESEEM probes interactions with more distant nuclei [Figure 1-6(b), red region].

• *Continuous wave (CW)-ESR*

The CW-ESR spectra provide information on strong interactions between the Cu(II) electron and neighboring nuclei. The magnitude of $g_{||}$ (the parallel component of the axially

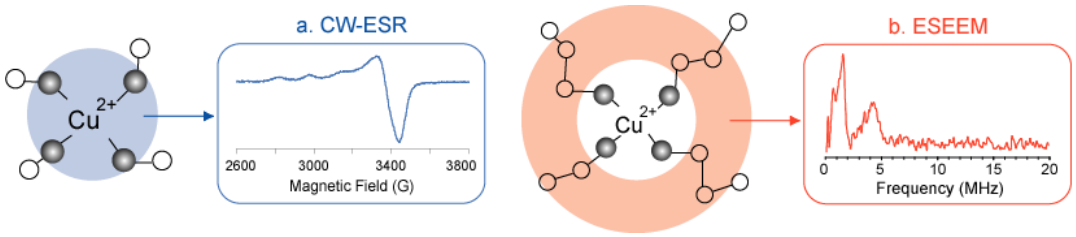

Figure 1-6: (a) CW-ESR measures strong interactions such as the hyperfine interaction of electron spin with Cu(II) nuclei (blue region). (b) ESEEM detects interactions with more distant nuclei (red region).

symmetric g tensor) and $A_{||}$ (the parallel component of the hyperfine interaction) are dependent on, among many factors, the ligand environment of Cu(II) ions (*45*). Peisach and Blumberg have demonstrated that type II copper in both natural and artificial copper proteins is ligated to nitrogen and oxygen but not to sulfur (*45*). They have also described how $g_{||}$ and $A_{||}$ can be used for the assignment of coordinating nitrogen and oxygen atoms of the copper binding site (cf. Figure 1-7). In the case of the same atoms of ligation, if the charge of the metal-ligand complex is decreased, $g_{||}$ is decreased and $A_{||}$ is increased.

The most important part of this CW-ESR analysis is that regions of overlap exist among the different types of ligation, and this overlap leads to ambiguous assignments for the copper binding site. Therefore, ESEEM spectroscopy, which can probe the atoms of the second ligation sphere, becomes useful to elucidate the structure around the Cu(II) ion.

• *Electron spin echo envelope modulation (ESEEM)*

ESEEM is a technique for measuring weak hyperfine and quadrupole interactions of the nuclei in the environment (within ~ 10 Å) of the paramagnetic center (*46-48*). In the presence of nuclear spins weakly coupled with the electron spin, the intensity of the echo is modulated at the nuclear transition frequencies of the interacting nucleus.

A simple qualitative explanation for ESEEM is described in Figure 1-8. When an electron spin (S = 1/2) is coupled with a nuclear spin (I = 1/2) in a constant external magnetic field, B_0, which is assumed as being along z-axis (an equilibrium direction of the field), the nucleus is in an effective local magnetic field, $\vec{B}_{eff}(\alpha) = \vec{B}_0 + \vec{B}_{hf}(\alpha)$, where $\vec{B}_{hf}(\alpha)$ is the magnetic field induced by the electron at the nucleus. Symbols α and β represent electron spin quantum

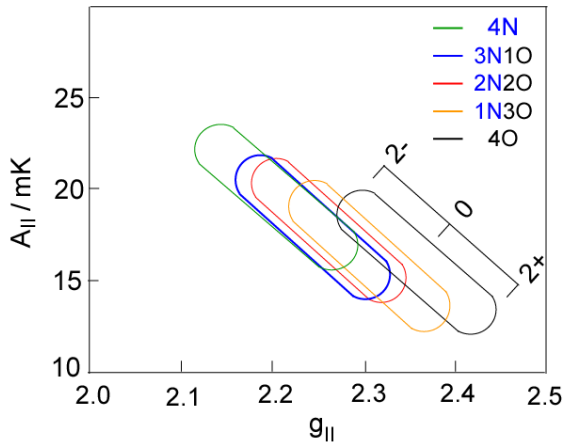

Figure 1-7: The correlation between the coordinating atoms in the copper binding site and the values, $g_{||}$ and $A_{||}$ (Taken from Peisach, J., and Blumberg, W. E. (1974) *Arch. Biochem. Biophys. 165*, 691-708 with permission of the Elsevier). The diagonal scale shows the total charge for the Cu(II)-ligand complex. In the CW-ESR spectrum, the hyperfine splitting is detected by ΔH in gauss and it is necessary to convert the units from gauss to millikaisers, using $A = 0.046686 g \Delta H$.

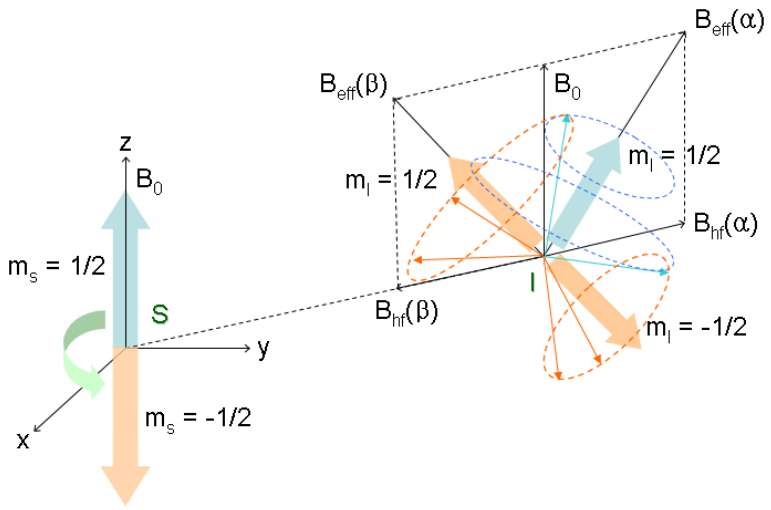

Figure 1-8: Nuclear spin precession at different electron spin orientations. An electron spin (S = 1/2) interacts with a nuclear spin (I = 1/2) in the external magnetic field B_0. Symbols m_s and m_I denote electron and nuclear spin quantum numbers, respectively.

numbers $m_s = 1/2$ and $m_s = -1/2$, respectively. Since $\vec{B}_{hf}$ is substantial, the nuclear spin precesses about the quantization axis, $\vec{B}_{eff}(\alpha)$ that differs from the direction of B_0.

If the orientation of the electron spin changes from $m_s = 1/2$ to $m_s = -1/2$ (e.g. due to a π pulse), the induced magnetic field orientation also changes from $\vec{B}_{hf}(\alpha)$ to $\vec{B}_{hf}(\beta)$ (shown in Figure 1-8), where $\vec{B}_{eff}(\beta) = \vec{B}_0 + \vec{B}_{hf}(\beta)$. The nuclear spin starts to precess about this axis, $\vec{B}_{eff}(\beta)$. In the case of $I = 1/2$, the new axis, $B_{eff}(\beta)$, can be either positive for $m_I = 1/2$ or negative for $m_I = -1/2$ depending on the initial nuclear spin states. The symbol m_I denotes the nuclear spin quantum number. As a result, the ESR transition can involve nuclear transitions, leading to selection rules, $\Delta m_s = \pm 1$ and $\Delta m_I = 0$ for the allowed transitions, or $\Delta m_s = \pm 1$ and $\Delta m_I = \pm 1$ for the "forbidden transitions" (Note that Δm_I refers to nuclear quantization along the B_0 axis.).

Figure 1-9 shows the energy levels and ESR transitions. In the absence of the external magnetic field, B_0, the energy levels are degenerate. In the presence of the external magnetic field, the electron spin energy levels are split into $m_s = -1/2$ (the lower energy, antiparallel) and $m_s = 1/2$ (the higher energy, parallel) spin states due to the electron Zeeman interaction. Each energy state is further split into 1/2 and -1/2 due to the nuclear Zeeman interaction and finally, has four energy levels with the hyperfine interaction. The allowed transitions are shown by solid arrows in Figure 1-9, and the "forbidden transitions" are shown by dashed arrows in Figure 1-9. The transitions, ω_α and ω_β are called the electron nuclear double resonance (ENDOR) frequencies.

The frequency of the four transitions in Figure 1-9 can be determined from the spin Hamiltonian. The spin Hamiltonian in an external magnetic field, B_0, is :

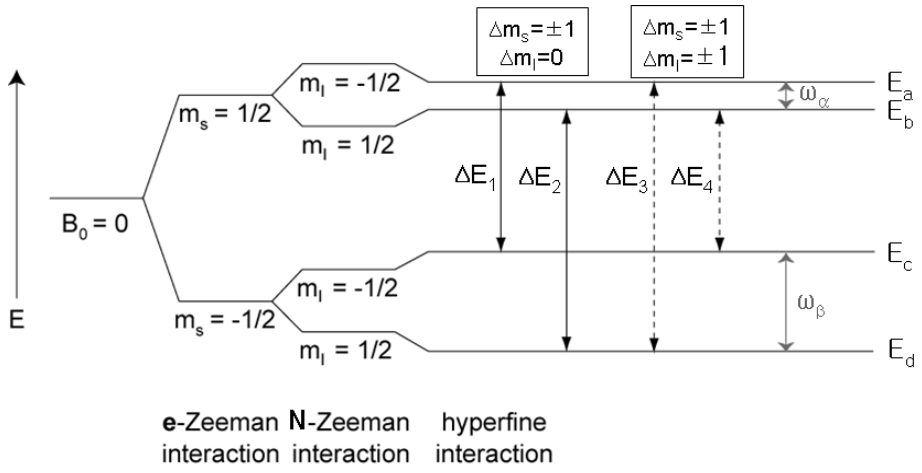

Figure 1-9: Energy levels and ESR transitions for an electron spin (S = 1/2) coupled with a nuclear spin (I = 1/2). Symbols m_s and m_I denote electron and nuclear spin quantum numbers, respectively. There are two allowed transitions ($\Delta m_s = \pm 1$ and $\Delta m_I = 0$) and two "forbidden transitions" ($\Delta m_s = \pm 1$ and $\Delta m_I = \pm 1$). The transitions, ω_α and ω_β are called the ENDOR frequencies.

$$\hat{H} = \hat{H}_{EZ} + \hat{H}_{NZ} + \hat{H}_{HF} \qquad (1\text{-}4)$$

where $\hat{H}_{EZ} = \beta_e \vec{B} \cdot \vec{\vec{g}}_e \cdot \hat{S}$

$\hat{H}_{NZ} = -\beta_N \vec{B} \cdot \vec{\vec{g}}_N \cdot \hat{I}$

$\hat{H}_{HF} = \hat{S} \cdot \vec{\vec{A}} \cdot \hat{I}$

The term $\vec{\vec{g}}$ is the *g*-tensor, β_e is the Bohr magneton, β_N is the nuclear magneton, $\vec{B}$ is the applied magnetic field, which is a vector field, $\vec{B} = (0,0,B_0)$, $\hat{S}$ and $\hat{I}$ represent electron and nuclear spin angular momentum operators, respectively, and $\vec{\vec{A}}$ is an anisotropic hyperfine tensor. The first and second terms are the electron and nuclear Zeeman interactions, respectively, describing the interaction of the electron and nuclear spins, respectively, with an external magnetic field. The third term, the hyperfine interaction, represents the interaction of the electron spin with the magnetic moments of nuclear spin.

In order to provide a simple picture, we consider the case where the Zeeman terms are isotropic. Then, at high-field, equation 1-4 is simplified to :

$$\begin{aligned} \hat{H} &= g_e \beta_e \vec{B} \cdot \hat{S} - g_N \beta_N \vec{B} \cdot \hat{I} + \hat{S} \cdot \vec{\vec{A}} \cdot \hat{I} \\ &= g_e \beta_e B_0 \hat{S}_z - g_N \beta_N B_0 \hat{I}_z + A_{zx} \hat{S}_z \hat{I}_x + A_{zy} \hat{S}_z \hat{I}_y + A_{zz} \hat{S}_z \hat{I}_z \end{aligned} \qquad (1\text{-}5)$$

The electron and nuclear frequencies of the magnetic field satisfy the resonance condition, $h\nu_s = \hbar\omega_s = g_e\beta_e B_0$ and $h\nu_I = \hbar\omega_I = g_N\beta_N B_0$, respectively. The constant $\hbar$ converts the hyperfine constant into frequency units ($A = \hbar a$).

$$\hat{H} = \hbar\omega_s \hat{S}_z - \hbar\omega_I \hat{I}_z + \hbar a_{zx} \hat{S}_z \hat{I}_x + \hbar a_{zy} \hat{S}_z \hat{I}_y + \hbar a_{zz} \hat{S}_z \hat{I}_z \qquad (1\text{-}6)$$

The Hamiltonian, $\hat{H}$, can be expressed in matrix form using a basis set consisting of the electron spin wavefunction $\{|\alpha_e\rangle, |\beta_e\rangle\}$ and the nuclear spin wavefunction $\{|\alpha_N\rangle, |\beta_N\rangle\}$.

$$\hat{H} = \frac{\hbar}{2}\begin{pmatrix} \omega_s - \omega_I + \frac{a_{zz}}{2} & \frac{a_{zx}}{2} + \frac{a_{zy}}{2i} & 0 & 0 \\ \frac{a_{zx}}{2} - \frac{a_{zy}}{2i} & \omega_s + \omega_I - \frac{a_{zz}}{2} & 0 & 0 \\ 0 & 0 & -\omega_s - \omega_I - \frac{a_{zz}}{2} & -\frac{a_{zx}}{2} - \frac{a_{zy}}{2i} \\ 0 & 0 & -\frac{a_{zx}}{2} + \frac{a_{zy}}{2i} & -\omega_s + \omega_I + \frac{a_{zz}}{2} \end{pmatrix} \qquad (1\text{-}7)$$

The Hamiltonian, $\hat{H}$, is diagonalized in order to determine the energy levels. They are given by :

$$\begin{aligned} E_a &= \frac{\hbar}{2}\omega_s + \frac{\hbar}{2}\sqrt{\frac{a_{zx}^{\,2}}{4} + \frac{a_{zy}^{\,2}}{4} + \left(\frac{a_{zz}}{2} - \omega_I\right)^2} = \frac{\hbar}{2}\omega_s + \frac{\hbar}{2}\omega_\alpha \\ E_b &= \frac{\hbar}{2}\omega_s - \frac{\hbar}{2}\sqrt{\frac{a_{zx}^{\,2}}{4} + \frac{a_{zy}^{\,2}}{4} + \left(\frac{a_{zz}}{2} - \omega_I\right)^2} = \frac{\hbar}{2}\omega_s - \frac{\hbar}{2}\omega_\alpha \\ E_c &= -\frac{\hbar}{2}\omega_s + \frac{\hbar}{2}\sqrt{\frac{a_{zx}^{\,2}}{4} + \frac{a_{zy}^{\,2}}{4} + \left(\frac{a_{zz}}{2} + \omega_I\right)^2} = -\frac{\hbar}{2}\omega_s + \frac{\hbar}{2}\omega_\beta \\ E_d &= -\frac{\hbar}{2}\omega_s - \frac{\hbar}{2}\sqrt{\frac{a_{zx}^{\,2}}{4} + \frac{a_{zy}^{\,2}}{4} + \left(\frac{a_{zz}}{2} + \omega_I\right)^2} = -\frac{\hbar}{2}\omega_s - \frac{\hbar}{2}\omega_\beta \end{aligned} \qquad (1\text{-}8)$$

The transitions, ω_α and ω_β are called the ENDOR frequencies, which are shown in Figure 1-8. As a result, four energy transitions (ΔE_1, ΔE_2, ΔE_3, and ΔE_4) between the energy levels can be obtained.

$$\begin{aligned}
\Delta E_1 &= \hbar(\omega_s + \frac{\omega_\alpha - \omega_\beta}{2}) \\
\Delta E_2 &= \hbar(\omega_s - \frac{\omega_\alpha - \omega_\beta}{2}) \\
\Delta E_3 &= \hbar(\omega_s + \frac{\omega_\alpha + \omega_\beta}{2}) \\
\Delta E_4 &= \hbar(\omega_s - \frac{\omega_\alpha + \omega_\beta}{2})
\end{aligned} \qquad (1\text{-}9)$$

• *ESEEM pulse sequence and the magnetization diagram*

The two-pulse ESEEM experiment is shown in Figure 1-10. The pulse sequence consists of two pulses ($\pi/2$ and π) separated by time, τ. At a time τ, after the second pulse, a spin echo is generated. When the time τ between the first and second pulses is increased, the intensity of the echo decays exponentially. In some cases, this decay is modulated. This modulation comes from the weak interactions with nuclei surrounding the paramagnetic center.

At equilibrium, the net magnetization vector lies along the direction of the applied magnetic field, B_0, and is called the equilibrium magnetization. The first pulse is a $\pi/2$ pulse and it rotates the magnetization by 90° to the –y direction. During the time interval τ, the magnetization dephases with a frequency ω_1 and after the time τ, a phase angle $\theta_1 = \omega_1\tau$ develops. When the π pulse is applied to the system, the magnetization vector rotates 180° about the x-axis and refocuses at time τ. The π pulse may cause the nuclear spin transition and therefore the electron spin may precess at a different frequency, ω_2. Thus, after a time τ after the π pulse, a

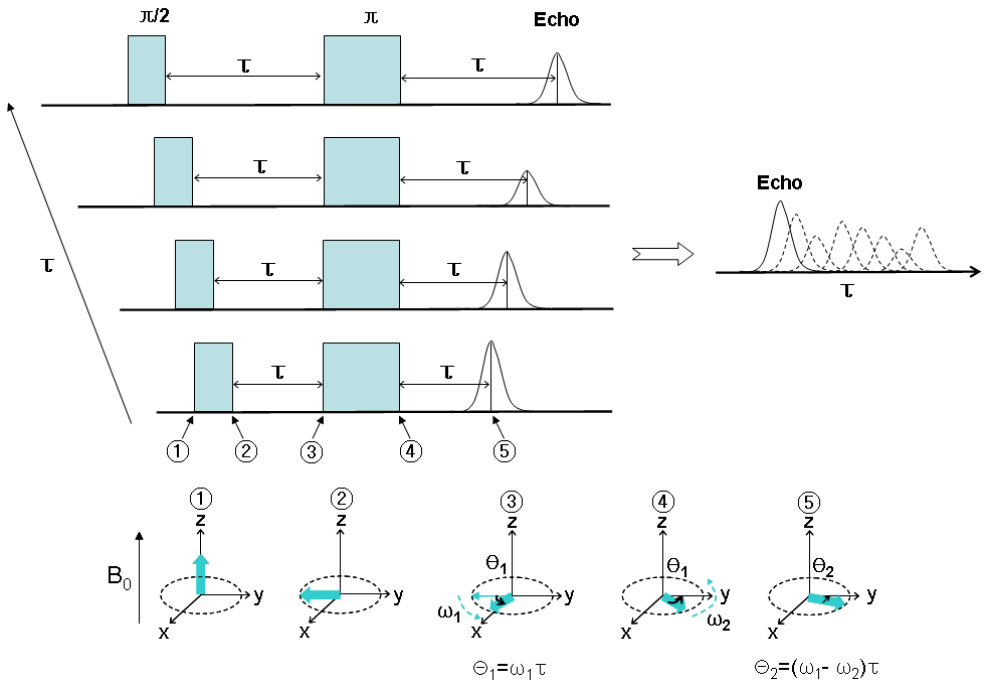

Figure 1-10: Two-pulse ESEEM pulse sequence (*π/2* and *π* pulses) and the magnetization diagram. In the experiment, the time interval τ is stepped and the echo modulation comes from the weak interactions with nuclei surrounding the paramagnetic center.

spin echo is generated with the phase angle $\theta_2 = (\omega_1 - \omega_2)\tau$.

The ESEEM signal in the time domain, V(τ), arises from the differences between the ESR transition frequencies of the spin system. In addition, the signal is proportional to cos(θ_2). For example, if $\omega_1=\Delta E_1/\hbar$ and $\omega_2=\Delta E_2/\hbar$ where ΔE_1 and ΔE_2 are given by equation 1-9.

$$\begin{aligned}\cos(\theta_2) &= \cos(\omega_1 - \omega_2)\tau = \cos(\frac{\Delta E_1}{\hbar} - \frac{\Delta E_2}{\hbar})\tau \\ &= \cos(\omega_s + \frac{\omega_\alpha - \omega_\beta}{2} - (\omega_s - \frac{\omega_\alpha - \omega_\beta}{2}))\tau = \cos(\omega_\alpha - \omega_\beta)\tau\end{aligned} \qquad (1\text{-}10)$$

The modulation frequency $\omega_\alpha - \omega_\beta$ is obtained from this equation.

If all the transitions (allowed and forbidden) between the energy levels are considered, four modulation frequencies, ω_α, ω_β, $\omega_\alpha+\omega_\beta$, and $\omega_\alpha-\omega_\beta$, are observed. Therefore, the total expression for two-pulse ESEEM is

$$V(\tau) = -\frac{k}{4}[2 - 2\cos(\omega_\alpha\tau) - 2\cos(\omega_\beta\tau) + \cos\{(\omega_\alpha + \omega_\beta)\tau\} + \cos\{(\omega_\alpha - \omega_\beta)\tau\}] \qquad (1\text{-}11)$$

where the coefficient *k* determines the modulation depth (*47, 49*). The two-pulse ESEEM method is dependent on the phase memory time which is usually short for metal spins. Therefore, the modulations for metal spins rapidly decay, providing broad lines in the spectrum.

In order to obtain narrower lines, the three-pulse experiment has been found to be more useful. The three-pulse ESEEM method is not significantly affected by the phase memory time. Furthermore, the spectrum has no sums and differences of the nuclear frequencies, providing

only nuclear frequencies, ω_α and ω_β. The three-pulse ESEEM is (*47, 49*) represented by the expression

$$V(\tau,T) = 1 - \frac{k}{4}\left\{[1-\cos(\omega_\alpha\tau)][1-\cos(\omega_\beta T)] + [1-\cos(\omega_\beta\tau)][1-\cos(\omega_\alpha T)]\right\} \quad (1\text{-}12)$$

The first and second $\pi/2$ pulses are separated by time τ and the third $\pi/2$ pulse is applied after the time interval *T*. The echo is observed at time τ after the third pulse. The echo envelope is modulated as *T* is incremented. Fourier Transform of the time domain modulation pattern yields a spectrum with frequencies directly related to the hyperfine and nuclear quadrupole interactions.

• *Interpretation of the ESEEM spectrum for characterizing the copper-binding site*

Three-pulse ESEEM spectroscopy is performed to aid the characterization of the copper coordination environment in Aβ in Chapters 3 and 4. For the case of Cu(II) ions in Aβ, the ESEEM spectroscopy detects the magnetic interactions between a paramagnetic center, Cu(II), and weakly coupled nuclei (e.g. ^{14}N or ^{1}H). For the case of the proton, ^{1}H (I = 1/2), the ESEEM spectrum has one peak around 14.3 MHz ($\omega_\alpha \approx \omega_\beta$) in the presence of an external magnetic field B_0 = 3360 G. The three-pulse ESEEM spectrum for ^{14}N (I = 1) has characteristic spectral lines associated with the nuclear quadrupole interaction.

The ^{14}N-ESEEM analysis for Cu(II) - ethylenediamine-imidazole and Cu(II) - $(imidazole)_4$ in water-glycerol glasses was first performed by Mims and Peisach in 1978 (*48*). A typical ^{14}N-ESEEM spectrum for Cu(II) – imidazole complex shows four major frequencies, three narrow lines at 0.57, 1.03, and 1.6 MHz and a broad line centered at 4.2 MHz (*50*). In

Figure 1-11A, the three low frequencies are characteristic of a weakly coupled ^{14}N nucleus where the nuclear Zeeman and electron-nuclear hyperfine interaction approximately cancel one another out. Therefore, the energy level splittings are almost completely determined by the ^{14}N nuclear quadrupole interaction (NQI) (*48, 51, 52*) and the sum of the lower two frequencies is almost equal to the highest one.

The other line around 4.2 MHz, shown in Figure 1-11A, arises from the condition where the nuclear Zeeman and electron-nuclear hyperfine interactions are additive. This frequency has much broader spectral line which is due to a double quantum (DQ) transition of the remote nitrogen of the imadazole (*46, 48, 53*).

Another feature of the ESEEM spectrum for Cu(II) - imidazole complex shown in Figure 1-11B is the presence of several components between 2 ~ 4 MHz. When the electron spin of the Cu(II) ion interacts with more than one imidazole, the combination frequencies of the three NQI frequency lines are observed. As the number of interacting ^{14}N nuclei is increased, additional lines appear in the ESEEM spectrum and interfere with the low frequency region, allowing the 4.2 MHz line to dominate the ESEEM spectrum [shown in Figure 1-11B for the complex with four imidazoles]. Based on the computer simulations, the ESEEM spectroscopy may quantify the number of coupled imidazoles associated with a paramagnetic center (*54*).

The amino acid, histidine has an imidazole side chain. When the Cu(II) ion is coordinated with one or more histidine residues in proteins, the remote nitrogen of the imidazole provides characteristic frequencies in the ESEEM spectrum (*46, 48, 53*). This strategy of ESEEM spectroscopy is useful to identify and quantify the number of interacting imidazoles at the copper-binding site.

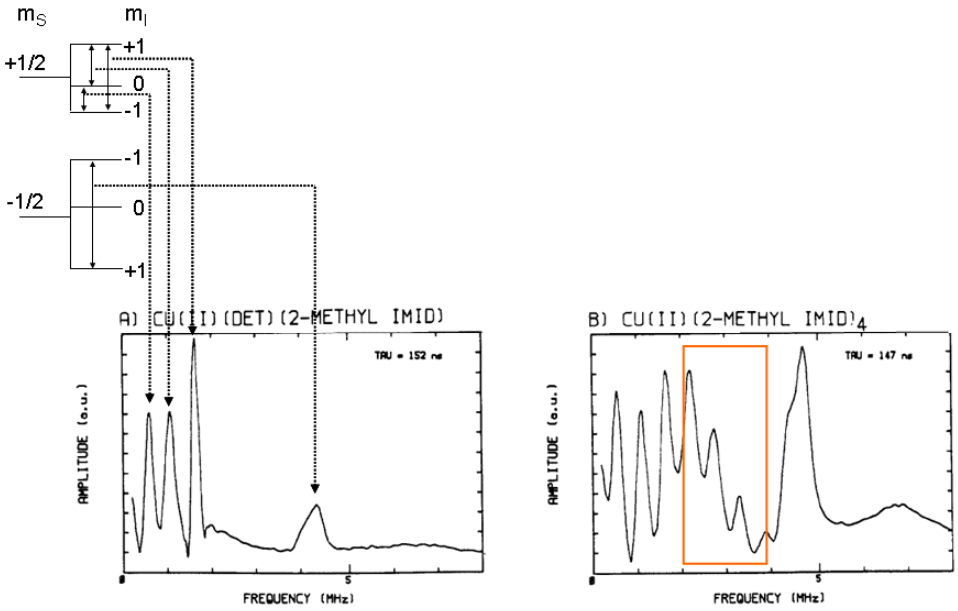

Figure 1-11: ESEEM spectra for (A) Cu(II) diethylenetriamine 2-methylimidazole and (B) Cu(II) tetrakis(2-methylimidazole) (Taken from McCracken, J., Pember, S., Benkovic, S. J., Villafranca, J. J., Miller, R. J., and Peisach, J. (1988) *J. Am. Chem. Soc. 110*, 1069-1074 with permission of the American Chemical Society). (A) The ESEEM spectrum provides characteristic frequencies when the Cu(II) ions interact with the remote ^{14}N nuclei (I = 1) of the imidazole ring. (B) The presence of spectral features between 2 ~ 4 MHz indicates that electron spin of the Cu(II) ion interacts with more than one nitrogen.

2.0 UNFOLDING OF ALANINE-BASED PEPTIDES USING ELECTRON SPIN RESONANCE DISTANCE MEASUREMENTS

This work, written in collaboration with James S. Becker, Mike Yonkunas, Rob Coalson, and Sunil Saxena, has been published in Biochemistry, 2006, V.45, pages 11666-11673 (55).

2.1 ABSTRACT

We describe a scheme for tagging an alanine-based peptide with a Cu(II) and a nitroxide to measure unfolding transitions. The enhancement in longitudinal relaxation rate of the nitroxide due to the presence of Cu(II) was measured at physiological temperatures by pulsed electron spin resonance (ESR). The change in relaxation rate provided the average interspin distance between the Cu(II) and the nitroxide. Control experiments on a proline-based peptide verify the robustness of the method. The change in interspin distances with temperature for the alanine-based peptide is in accord with the change in helicity measured by circular dichroism. The data provide an opportunity to examine the unfolding process in polyalanine peptides. The distance in the folded state is in concordance with molecular dynamics. However, the ESR experiment measures an average distance of 17 Å in the unfolded state, whereas molecular dynamics indicates a distance of 42 Å if the unfolded geometry was a polyproline type II helix. Therefore,

ESR demonstrates that the unfolded state of this alanine-based peptide is not an ideal *extended* polyproline type II helix.

2.2 INTRODUCTION

The advent of site-directed spin labeling has resulted in electron spin resonance (ESR) emerging as a useful spectroscopic technique for the measurement of protein structure and conformational dynamics (*4-7*). Using site-directed spin labeling, two spin labels (typically nitroxides) can be placed at virtually any position on the protein backbone. Concomitant methodological developments in ESR (*21, 22, 40, 56-60*) permit the measurement of interspin distance in the range of 8-70 Å in order to provide constraints for structure elucidations (*16, 61-73*). However, the distance methods are largely applicable only at very low temperatures (ca. 10-80 K), and this proves to be a disadvantage in the context of monitoring unfolding events in proteins or peptides.

We describe an approach by which distances of at least up to 25 Å can be measured using ESR at physiologically relevant temperatures. In this approach a Cu(II) binding site is generated at one end of a biomolecule. A nitroxide spin label is attached at another position using site-directed spin labeling. By exploiting methodological advances in Fourier Transform ESR (*38, 40-43, 74-76*) which enable the routine measurement of the free induction decay signal from labeled macromolecules, the enhancement of relaxation rate of the nitroxide by the presence of Cu(II) is obtained. The enhancement of relaxation rate can be used to measure metal to nitroxide interspin distances, as has been well demonstrated at low temperatures (*26, 35-37, 77, 78*). We

show that nanometer range interspin distances may also be measured at physiological temperatures. This builds on methodologies developed by Voss et al. (*79*), which showed that the changes in nitroxide line broadening and intensity may be used to measure the metal-nitroxide distance. Nitroxide-nitroxide distances at physiological temperatures may also be measured by calibrating the increase in the line broadening due to the presence of the second spin (*12*).

Significantly, we show that this methodology may be used to resolve the average distance between two units as an alanine-based peptide melts with temperature. Thus the experiments capture the average separation between two units in the ensemble of conformations that constitute a given step in the unfolding pathway. The unfolding transition of polyalanines is of paradigmatic significance in the field of protein folding. Spectroscopic experiments (*80-86*) as well as computer simulations (*80, 82, 87-89*) have recently indicated that α-helical polyalanine peptides unfold to polyproline type-II helical structures (PPII). This geometry has also been suggested to exist in the unfolded states of other peptides (*90, 91*) and some proteins (*90, 92, 93*). This is significant because, if such nativelike secondary structure elements are indeed present in the unfolded state of proteins, then the entropic cost associated with folding is vastly reduced. Our results support the conclusions of Pande and co-workers that the PPII geometry of individual alanines does not propagate into an overall *extended* polyproline II structure in the unfolded state of polyalanines (*94*).

2.3 MATERIALS AND METHODS

The alanine-based peptide PPHGGGWPAAAAKAAAAKCAAAAKA (P, proline; H,

histidine; G, glycine; W, tryptophan; A, alanine; K, lysine; C, cysteine), shown schematically in Figure 2-1, and the proline-based peptide PPHGGGWPPPPPPPCPPK were synthesized at the Molecular Medicine Institute, University of Pittsburgh. In these peptides, the lysine residues serve to confer solubility in aqueous solutions, and the PHGGGW sequence constitutes a well-characterized copper binding sequence (*46, 53, 95*). Using site-directed spin labeling (SDSL), a (1-oxy-2,2,5,5-tetramethylpyrroline-3-methyl)methanethiosulfonate spin label (MTSSL) that was purchased from Toronto Research Chemicals Inc. (Ontario, Canada) was covalently bound to the cysteine residue in both peptides.

For ESR experiments, 250 μM solutions of each peptide were prepared in an aqueous buffered solution of 10 mM potassium chloride (KCl) and 25 mM *N*-ethylmorpholine (NEM), at pH 7.6. Spectroscopic data were obtained on each peptide in the presence and in the absence of coordinated Cu(II). Experiments were also conducted in the presence of Zn(II), a diamagnetic metal. For the metal-coordinated samples, a 1 mol equivalent of Cu(II) [or Zn(II)] was added from a 0.01 M aqueous copper sulfate (or zinc chloride) solution. For ESR experiments, 6 μL of peptide solution in a 1.5 mm inner diameter Pyrex tube was degassed by freeze-pump-thaw cycles until a final pressure of 2 x 10^{-4} Torr to eliminate oxygen in the solution. The samples were bath sonicated for approximately 5 min before insertion into the ESR cavity.

● *Electron Spin Resonance (ESR) Spectroscopy*

Spectroscopic experiments were performed on a Bruker EleXsys E580 X-band CW/Pulse ESR spectrometer equipped with a Bruker ER4118X-MS3 split-ring resonator. The temperature was controlled using an Oxford 1TC605 temperature controller and an Oxford ER 4118CF gas flow cryostat.

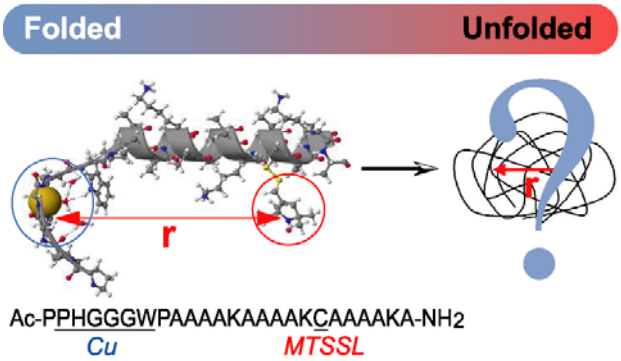

Figure 2-1: The central question of the state to which a polyalanine helix unfolds is illustrated. A schematic of the folded α-helical state of polyalanine is shown on the left. The Cu(II) center and the nitroxide spin label are also shown. The ESR experiments measure the interspin distance between Cu(II) and nitroxide, r_{ESR}, as a function of temperature.

The longitudinal relaxation time of the nitroxide in the peptide samples was measured over a temperature range of 270-315 K by using an inversion recovery sequence. The inversion recovery experiment consists of a two-pulse, π-t-$\pi/2$ sequence. The high output power of the ASE-TWTA (1 kW) combined with a quality factor, Q, much less than 100 provided $\pi/2$ and π pulses of 6 and 12 ns, respectively. The initial interpulse separation, t, was 20 ns, and the delay t was stepped out by 180-340 ns for a total 64 or 128 points according to each experimental condition. The FID after the second pulse was digitized every 4 ns for a total of 1024 points after a dead time of 50 ns. At each temperature, the experimental data were measured several times, and the errors were determined from twice the standard deviation of these measurements.

● *Circular Dichroism (CD) Spectroscopy*

The thermal stability of the peptides was assessed using CD by following the change in the spectrum with temperature. The peptides were dissolved in a 10 mM potassium phosphate buffer, a pH of 7.0, and at a peptide concentration of 250 μM. The measurements were made on an AVIV model 202 circular dichroism spectrometer. The samples contained 400 μL of peptide solution in a 0.1 cm path-length cuvette. A single wavelength, 220 nm, which measures the net α-helicity, was monitored for the alanine-based peptide as a function of temperature (*96*). The data for the peptide in the presence and absence of Cu(II) were practically identical (see Figure 2-2), indicating that Cu(II) binding does not substantially change the thermodynamics of thermal unfolding. For the proline-based peptide, a wavelength of 206 nm, which monitors the net polyproline II (PPII) helical structure, was monitored (*97, 98*). The signals at the specific wavelength were then recorded continuously as the temperature was increased from 268 to 368 K, with sampling points at every 1 K.

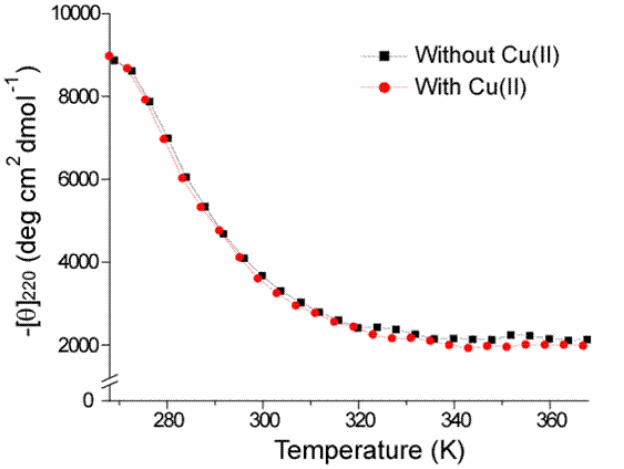

Figure 2-2: The comparison of the thermal unfolding profile for the alanine-based peptide in the absence and presence of Cu(II).

The affinity of peptide-Cu(II) complexes was verified by CD. When Cu(II) binds to peptides, weak *d-d* transitions appear in the visible region over a range of wavelengths from 500 to 750 nm (*46*). According to the CD data Cu(II) was bound to the peptide between 270 and 365 K. On the basis of the affinities of Cu(II) to the HGGGW segments (*46*), as much as 88% of the peptides bind Cu(II). A simple analysis shows that the incomplete binding leads to errors of less than 0.5 Å in the measured distances.

● *Generation of α-Helical and PPII Ensembles*

To define the α-helical conformation, the peptide without the copper binding domain (AAAAKAAAAKCAAAAKA) was constructed with Ramachandran angles, Φ and Ψ of -57° and -47°, for peptide angles Φ and Ψ, respectively. For the extended polyproline II (PPII) conformation, these angles were modified to Φ = -75° and Ψ = 145° to reflect an ideal polyproline II helical-type geometry. The copper binding domain (PPHGGGW) coordinates were obtained from the X-ray structure (*53*) and joined to the backbone through the added proline residue Pro-8. The dihedral angle Ψ between Pro-8 and Ala-9, joining the copper binding domain to the peptide, was energy minimized using the molecular mechanics (MM3) force field (*99*). Dihedrals angles of Ψ = -28° and Ψ = 46° were obtained for the α-helical and PPII-type ensembles, respectively.

A new residue was added to the CHARMM27 force field (*100*) representing the MTSSL spin label attached to a modified cysteine residue side chain. The bonds, angles, and dihedrals of the spin label were modeled according to previous research on nitroxides (*101*). In the same light, charges on MTSSL were selected on the basis of CHARMM standards and modeled from the CHARMM27 amino acid force field. Two systems were prepared for molecular dynamics (MD)

simulations: the alanine-based peptide in the α-helical conformation and the same peptide in the PPII conformation, both built up with a Cys-19-MTSSL side chain substitution. Each system was solvated in the VMD molecular graphics environment (*102*) utilizing the built-in solvate 1.2 package. The solvent box was extended to 7 Å beyond the largest dimension along each axis. This condition allows minimal protein-protein interaction upon generation of periodic boundaries during simulations. All atom simulations were performed using the NAMD2 package (*103*). A conjugate gradient energy minimization was performed over 10000 steps to relieve bad contacts, with a harmonic protein backbone restraint of 999 kcal mol^{-1} $Å^{-2}$. The α-helical system was then subjected to a short equilibration at 300 K and the PPII system at 315 K for 100 ps at constant volume. Subsequently, 250 ps of constant pressure molecular dynamics was performed with the protein backbone restrained to 500 kcal mol^{-1} $Å^{-2}$. Langevin dynamics and Langevin piston pressure (*104*) were used to maintain temperature and pressure at 300 or 315 K and 1 bar, respectively. Periodic boundary conditions and all atom wrapping were imposed for all simulations. Long-range electrostatics was calculated with the particle mesh Ewald (PME) formalism and updated every four steps. A time step of 1 fs was used with trajectories written every 0.5 ps. A van der Waals cutoff distance of 10 Å and a pair list distance of 11.5 Å were implemented at each phase of dynamics simulations.

Tcl scripting in VMD was used to determine the average distance over all trajectory frames from the copper atom to the nitroxide spin label for each simulation system. Average distances converged to a value of 25 and 42 Å for the α-helical conformation and the PPII conformation, respectively, after 100-200 ps of MD simulations.

2.4 RESULTS

● *Measurement of the relaxation rate using inversion recovery experiment*

The alanine-based peptide (PPHGGGWPAAAAKAAAAKCAAAAKA) and the proline-based peptide (PPHGGGWPPPPPPPCPPK) were designed with a Cu(II) binding PHGGGW sequence at one end (*46, 53, 95*). In both, a nitroxide spin label was covalently attached to the cysteine using site-directed spin labeling (*6, 7, 105, 106*). Transition metals, such as Cu(II), usually have a much shorter longitudinal relaxation time than the nitroxyl radical. In systems containing a nitroxide and a coordinated transition metal, the fast relaxing metal spin can enhance the rate of the relaxation of the more slowly relaxing nitroxide spin (*26-28*). The change in the relaxation rate of the nitroxide depends on r^{-6}, where r is the distance between Cu(II) and nitroxyl spin. Eaton and co-workers have demonstrated the usefulness of this effect to determine the interspin distances between an Fe(III) center and nitroxide in complexes of metmyoglobin variants and methemoglobin (*35-37*) at low temperature (ca. 10-170 K).

Methodological advances in ESR now permit the detection of the Fourier Transform ESR signal even for samples with transverse relaxation times of ~20 ns (*38, 40-43*), as is typical for spin-labeled peptides and proteins. Thus the nitroxide relaxation times can be measured even at physiological temperatures. We show that by monitoring the change in nitroxide relaxation time upon coordination of the peptide with Cu(II), the distance, r_{ESR}, can be measured as the polyalanine peptide melts with temperature.

Figure 2-3 shows the inversion recovery experimental data at 305 K for the alanine-based peptide in the absence of Cu(II) (Figure 2-3a) and in the presence of Cu(II) (Figure 2-3b).

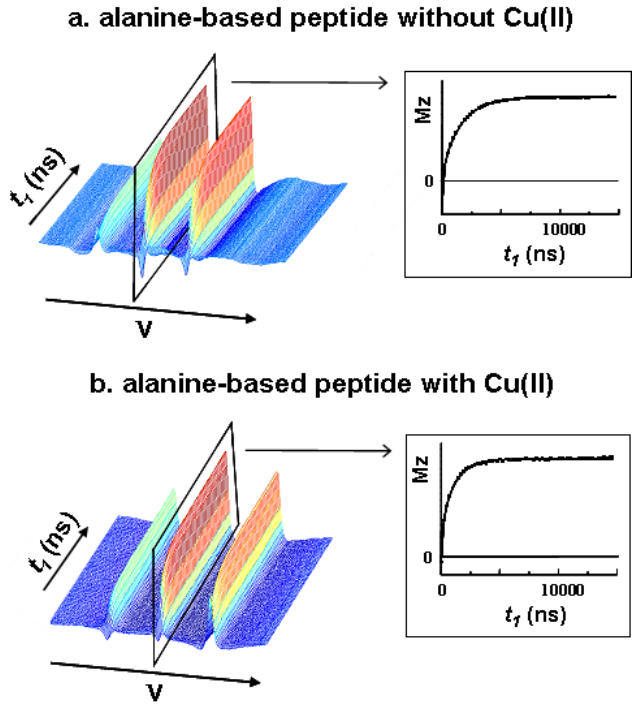

Figure 2-3: Inversion recovery spectrum of the nitroxide in the alanine-based peptide (a) without Cu(II) and (b) with Cu(II) at 305 K, respectively. The recovery curves for the central component are shown in the insets.

In Figure 2-3, the frequency dimension (v) provides the continuous wave (CW) equivalent spectrum and the time dimension (denoted by t_1) illustrates the recovery of magnetization to equilibrium after inversion of magnetization with a π pulse. The recovery of magnetization for the three hyperfine components of the nitroxide can be obtained by extracting slices parallel to "t_1" from the 2-D data set. The data for the central component are shown in the insets of Figure 2-3.

For the central nitroxide line the recovery of magnetization depends on the rate of electron spin-flips as well as on the rate of nuclear spin-flips. Schwartz and Freed (*31*) analyzed this effect theoretically, and they found that, in general, the recovery obeys a biexponential behavior of the form (*30, 31*):

$$S(t) = A + B\exp(-t/T_{1s}) + C\exp(-t/T_A) \qquad (2\text{-}1)$$

where $S(t)$ is the signal from the inversion recovery experiment, T_{1s} is the electron longitudinal relaxation time, and T_A depends on the nuclear spin-flip rates. The first time constant, T_{1s}, is related to electron spin-flips [note that subsequently we will use T_{1s}^0 and T_{1s} to denote the nitroxide longitudinal relaxation times in the absence and in the presence of Cu(II), respectively]. Schwartz and Freed found that T_A decreases from the slow motional regime to the fast motional regime, and finally T_A becomes constant in the fast motional regime (*31*).

All experimental recovery curves for both peptides fit well to equation 2-1. The value of T_A was constant at 120 ns throughout the entire experimental temperature region, as expected from theory (*30, 31*) for data in the fast motional regime. Figure 2-4 shows the longitudinal relaxation rates for the alanine-based peptide with Cu(II) and without Cu(II) between 270 and

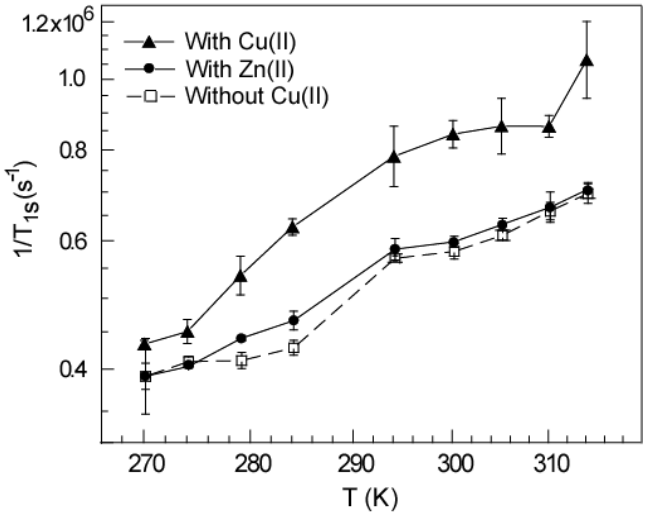

Figure 2-4: Nitroxide longitudinal relaxation rates of the alanine-based peptide in the absence (squares) and presence of Cu(II) (triangles) and in the presence of Zn(II) (circles). At each temperature, the longitudinal relaxation time was measured several times, and the error values were determined from twice the standard deviation. Addition of Cu(II), a paramagnetic metal, enhances the rate of the relaxation. Peptide concentrations were 250 μM in all experiments.

314 K. As control, the longitudinal relaxation rates for the peptide in the presence of Zn(II) (a diamagnetic metal) are also shown. In the presence of coordinated Zn(II), the nitroxide relaxation rate of the peptide does not change dramatically, demonstrating that the metal binding to the peptide does not change the peptide hydrodynamic radius. On the other hand, the nitroxide relaxation rate in the alanine-based peptide is enhanced by the addition of copper ion (a paramagnetic metal). The enhancement upon addition of Cu(II) is 11% at 270 K and 53% at 314 K, indicating that the average distance, r_{ESR}, decreases as the helix melts.

In Figure 2-5, the nitroxide relaxation rate for the proline-based peptide in the absence and presence of Cu(II) is shown as a function of temperature. The relaxation rate increases from 270 to 315 K, but the enhancement in nitroxide relaxation is fairly constant over the temperature range. At 270 K the enhancement upon addition of Cu(II) is 15%, and at 315 K it is 14%, indicating that the average distance, r_{ESR}, remains fairly constant over this temperature range.

The change in $1/T_{1s}^{0}$ can be due to two effects; (1) the fast relaxation of the paramagnetic metal, and (2) the modulation of the electron electron dipolar interaction by the overall tumbling of the peptide. As shown in appendix A, estimates of the enhancement based on the second effect overpredict the experimental enhancements, indicating that this model is incorrect. Therefore, the fast relaxation of the paramagnetic metal provides the principal mechanism for the change in $1/T_{1s}^{0}$ in these peptides.

Using this, quantitative estimates of r_{ESR} for the peptides may be obtained by using the Bloembergen theory (*32-34*) as modified by Kulikov and Likhtenshtein for application to systems containing a nitroxide and a paramagnetic metal (*26-28*). For the case of Cu(II) and in the fast motional regime:

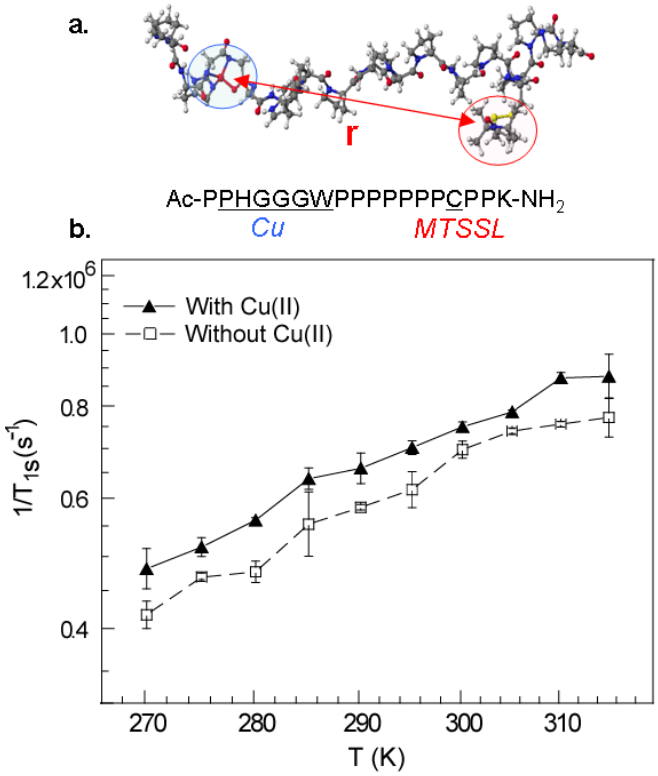

Figure 2-5: (a) A schematic of the proline-based peptide with polyproline type-II helical structure. (b) Nitroxide longitudinal relaxation rates of the proline-based peptide in the absence and presence of Cu(II). Enhancement in relaxation rate due to addition of Cu(II) is fairly constant. Peptide concentrations were 250 μM in all experiments.

$$\text{Defining } \kappa = \left(\frac{g_s{}^2 g_f{}^2 \beta_e{}^4}{10 \cdot \hbar^2} \times \left[\frac{T_{2f}}{1+(\omega_f - \omega_s)^2 T_{2f}{}^2} + \frac{3 \cdot T_{1f}}{1+\omega_s{}^2 T_{1f}{}^2} + \frac{6 \cdot T_{2f}}{1+(\omega_f + \omega_s)^2 T_{2f}{}^2} \right] \right),$$

$$r_{ESR} = \kappa^{1/6} \times \left[\left\{ \sum_{r_1}^{r_2} P(r) \cdot \left(\frac{\kappa}{r^6} + \frac{1}{T_{1s}{}^0} \right) \right\} - \frac{1}{T_{1s}{}^0} \right]^{-1/6} = \kappa^{1/6} \times \left[\frac{1}{T_{1s}} - \frac{1}{T_{1s}{}^0} \right]^{-1/6} \qquad (2\text{-}2)$$

where r_{ESR} is the ESR determined average interspin distance between Cu(II) and nitroxide, and *f* and *s* denote the electron spin of Cu(II) and nitroxide, respectively. The parameter $T_{1s}{}^0$ is the electronic longitudinal relaxation time of the nitroxide in the absence of Cu(II), and T_{1s} is the longitudinal relaxation time of the nitroxide in the presence of Cu(II). The parameters T_{1f} and T_{2f} are the electronic longitudinal and transverse relaxation times, respectively, for Cu(II). In equation 2-2, the values of g_f and g_s, which represent the *g* factors for Cu(II) and nitroxide electron spins, are 2.1166 (*107*) and 2.0061 (*43, 108*). Also, ω_f and ω_s, the resonant frequencies for Cu(II) and nitroxide, are 10.162 and 9.6317 GHz. The constant, β_e is the Bohr magneton and $\hbar$ is the Planck constant (*h*) divided by 2π. Finally, *P(r)* is the probability distribution, and r_1 and r_2 is the lower and upper range in the distribution function.

Equation 2-2 is strictly valid under the condition $\mu_0 g_s g_f \beta_e{}^2 T_{1f}/(4\pi h r_{ESR}{}^3) \ll 1$. Using a T_{1f} of 3 ns (see below), the constant yields 0.03 at r_{ESR} = 17 Å and 0.01 at r_{ESR} = 25 Å, respectively, demonstrating that equation 2-2 can be used for the distance range measured in the peptide (see below).

• *Average interspin distance measurements as peptide melts with temperature*

The values of $[1/T_{1s} - 1/T_{1s}{}^0]$ are determined experimentally for the alanine-based peptide and proline-based peptide, respectively (cf. Figures 2-4 and 2-5b). To determine r_{ESR}, the

values of T_{1f}, T_{2f} [the longitudinal and transverse relaxation times for Cu(II)] are required. Although $T_{1f} \approx T_{2f}$ in the fast motional regime, the parameters T_{1f}, T_{2f} are, in principle, temperature dependent. However, the data on the proline-based peptide suggest that for this coordination geometry T_{1f}, T_{2f} are constant over the measured temperature range.

Equation 2-2 was used to estimate the distance r_{ESR} for the proline-based peptide using the assumption that T_{1f} and T_{2f} are constant. In the analysis a value of $T_{1f} = T_{2f} = 3$ ns as reported in the literature (*109, 110*) was used. Figure 2-6 shows the measured distance r_{ESR} overlaid on the CD data for the proline-based peptide. The CD data indicate that the net PPII structure is fairly stable over this temperature range. Over the temperature range r_{ESR} changes from 24 to 21 Å, which is consistent with the stability of the PPII structure as indicated by CD. The measured value of r_{ESR} is also relatively insensitive to the exact value of T_{1f}. Changing the value of T_{1f} ($=T_{2f}$) over 2 orders of magnitude (i.e., from 0.1 to 10 ns) in equation 2-2 affects the obtained distance, r_{ESR}, by less than 10%. This is illustrated in the inset of Figure 2-6, which plots the interspin distance at 285 K as a function of T_{1f} ($=T_{2f}$). An average interspin distance of ~ 22-24 Å for proline-based peptide is also in accord with single molecule fluorescence and molecular dynamics results on polyproline peptides (*111*). Thus the assumption that $T_{1f} = T_{2f} = 3$ ns over the temperature range is reasonable.

Thus, the change in r_{ESR} for the alanine-based peptide as it melts can be determined by using $T_{1f} = T_{2f} = 3$ ns in equation 2-2. Figure 2-7 shows the CD data and the ESR determined Cu(II)-nitroxide interspin distances in the alanine-based peptide. The CD data indicate that the α-helicity is greatest at the lowest temperature and decreases as the temperature is increased. The content for three basic secondary structures, α-helix, β-sheet, and random coil, has been estimated based on the CD spectra published in the literature (*112-114*). Since many types of

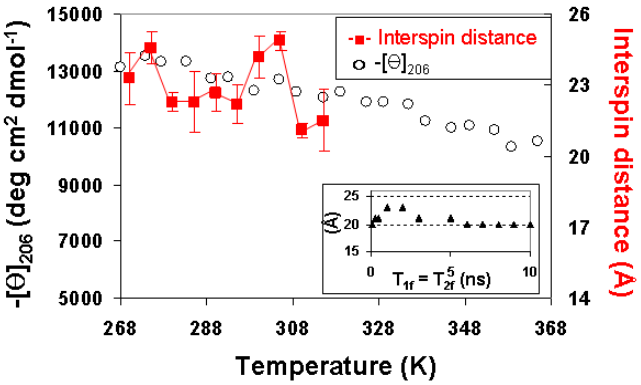

Figure 2-6: The Cu(II)-nitroxide interspin distances for the proline-based peptide from 270 K to 315 K overlaid on the thermal unfolding profile for proline-based peptide obtained using CD. Change of the interspin distance at 285 K as a function of T_{1f} ($=T_{2f}$) is shown in the inset.

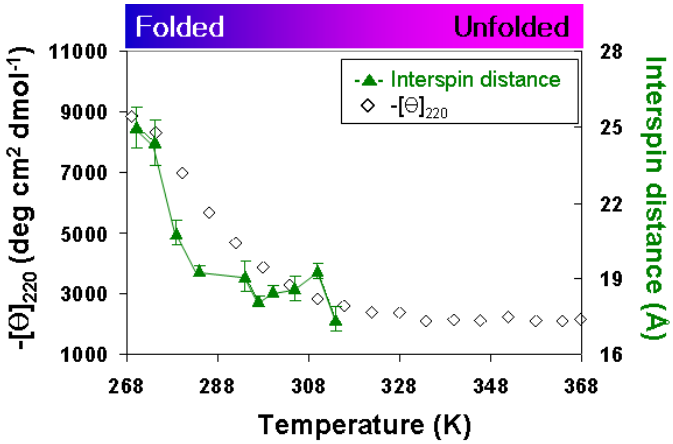

Figure 2-7: Cu(II)-nitroxide interspin distances for the alanine-based peptide from 270 K to 314 K overlaid on the thermal unfolding profile for the alanine-based peptide measured using CD. As temperature increases, the α-helical contents of the peptide decrease from ~ 25 % at 270 K to ~ 0 % at 314 K, indicating a loss of the stable structure.

structures within a particular class are grouped together, the accuracy of the estimation is not very high. Despite these uncertainties, the method is still reliable for monitoring changes in the quantity of the helicity under the unfolding experiment. The α-helical contents of the alanine-based peptide are estimated from ~ 25 % in the folded state to ~ 0 % in the unfolded state, with the CD data in Figure 2-7. The change in interspin distances is clearly in concordance with the change in helicity indicated by CD. As temperature increases, the Cu(II)-nitroxide interspin distance in the alanine-basedpeptide decreases from 25 ± 0.8 Å at 270 K to 17 ± 0.5 Å at 314 K, respectively. When the relaxation rates of the peptide with Zn(II) were used for $1/T_{1s}{}^{0}$ in equation 2-2, the Cu(II)-nitroxide interspin distances are within experimental errors at all temperatures except at 279 K. At this temperature the Cu(II)-nitroxide distance was found to be 21.8 ± 0.7 Å with the Zn(II) data instead of 20.8 ± 0.5 Å. The errors are estimated from experimental errors in the measurement of T_{1s} from multiple measurements and reflect uncertainties in the measurement of the mean distance.

● *Estimates of average measured distances in the presence of multiple conformations*

The sample is characterized by a distribution in distance due to the flexibility in the linker as well as the peptide backbone; the errors do not reflect the width of this distribution. Since the ESR observable (i.e., the change in relaxation rate) depends on r^{-6}, the ESR measured average distance is biased toward shorter conformations. In order to estimate this bias we consider that the range of interspin distances in the unfolded state of the peptide is characterized by a Gaussian function as:

$$P(r) = \frac{1}{\sigma\sqrt{2\pi}} e^{-(r-r_o)^2/2\sigma^2} \qquad (2\text{-}3)$$

where r_o is the actual average distance and σ is the standard deviation.

For a given distance, r, the change in relaxation rate due to the presence of Cu(II) may be estimated using the Bloembergen equation (cf. equation 2-2):

$$\left[\frac{1}{T_{1s}}-\frac{1}{T_{1s}{}^{o}}\right]=\left(\frac{g_s{}^2 g_f{}^2 \beta_e{}^4}{10\cdot\hbar^2 r^6}\times\left[\frac{T_{2f}}{1+(\omega_f-\omega_s)^2 T_{2f}{}^2}+\frac{3\cdot T_{1f}}{1+\omega_s{}^2 T_{1f}{}^2}+\frac{6\cdot T_{2f}}{1+(\omega_f+\omega_s)^2 T_{2f}{}^2}\right]\right) \quad (2\text{-}4)$$

The constants in equation 2-4 are defined in the equation 2-2. A value of $1/T_{1s}{}^{o}$ of 5.80 x 10^5 s^{-1}, which corresponds to the experimental value at a temperature of 300 K, was used.

A probability distribution, *P(r)*, was defined by fixing r_o and σ, and using equation 2-4 the change in $1/T_{1s}$ upon addition of Cu(II) was calculated for several r in the distribution function. Equation 2-5 was used to determine the expected average distance (r_{ESR}) from ESR distance measurements:

$$\text{Defining} \quad \kappa=\left(\frac{g_s{}^2 g_f{}^2 \beta_e{}^4}{10\cdot\hbar^2}\times\left[\frac{T_{2f}}{1+(\omega_f-\omega_s)^2 T_{2f}{}^2}+\frac{3\cdot T_{1f}}{1+\omega_s{}^2 T_{1f}{}^2}+\frac{6\cdot T_{2f}}{1+(\omega_f+\omega_s)^2 T_{2f}{}^2}\right]\right),$$

$$r_{ESR}=\kappa^{1/6}\times\left[\left\{\sum_{r_1}^{r_2}P(r)\cdot\left(\frac{\kappa}{r^6}+\frac{1}{T_{1s}{}^{o}}\right)\right\}-\frac{1}{T_{1s}{}^{o}}\right]^{-1/6} \quad (2\text{-}5)$$

where *P(r)* is the probability distribution, and r_1 and r_2 is the lower and upper range in the distribution function.

As an example, Figure 2-8 shows the distance distribution with r_o = 25 Å and with σ = 2, 3, 4, or 5 Å. Using equation 2-5, the ESR determined average distance, r_{ESR} = 24.4 Å, 23.6 Å,

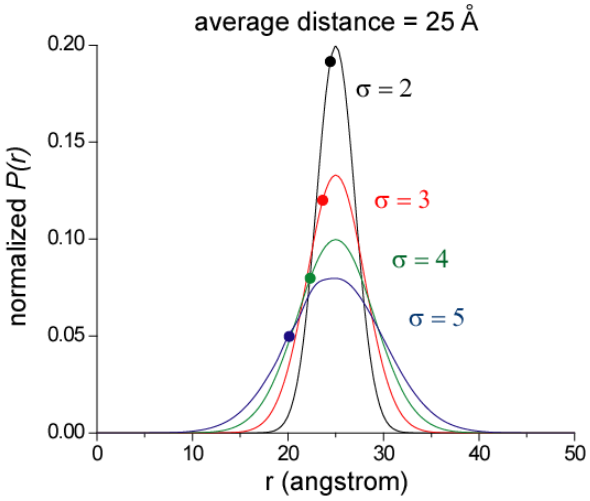

Figure 2-8: The comparison of the average distance from ESR distance measurements (shown by filled circles) for several standard deviations, σ = 2, 3, 4, or 5 Å at the actual average distance of 25 Å.

22.3 Å and 20.1 Å were obtained for σ = 2, 3, 4, and 5, respectively. These values are shown as filled circles in Figure 2-8. As the standard deviation increase, the average distance from ESR shifts to shorter distances. Results for several other average distances, r_o are summarized in Table 2-1.

A wide variety of literature suggests that for folded proteins and peptides containing two flexible MTSSL linkers, $\sigma \sim 3$ Å (*106, 115*). Therefore, in the folded state, the difference between the measured average distance from ESR and the actual mean distance is estimated to be within 7 ~ 20% for these peptides as long as the standard deviation of the distribution is within 4 Å.

• *Interpretation of ESR distances in terms of two-state models of peptide unfolding*

Unfolding in peptides is usually considered in terms of two-state cooperative or non-cooperative models. The cooperative model is an all-or-none transition, and thus the peptide is typically either completely folded or completely unfolded. If this transition is shown as an equilibrium between two states,

$$Folded \underset{k_2}{\overset{k_1}{\rightleftharpoons}} Unfolded \qquad (2\text{-}6)$$

the equilibrium constant (K) can be defined using the helicity of the peptide (θ) (*116*).

$$K = \frac{k_2}{k_1} = \frac{\theta}{1-\theta} \qquad (2\text{-}7)$$

Table 2-1: Average ESR distance with the different r_o and σ.

	r_o (Å)	r_{ESR} (Å)	r_o (Å)	r_{ESR} (Å)	r_o (Å)	r_{ESR} (Å)
$\sigma = 2$	20.0	19.3	25.0	24.4	30.0	29.6
$\sigma = 3$		18.2		23.6		28.9
$\sigma = 4$		16.0		22.3		28.0
$\sigma = 5$		10.7		20.1		26.5

For the cooperative model the expected distance at a given point of the unfolding pathway, $r_{cooperative}$ is given by:

$$r_{cooperative} = \kappa^{1/6} \times \left[\left\{ \sum_{r_1}^{r_2} \left(\theta \times \frac{1}{\sigma_f \sqrt{2\pi}} e^{-(r-r_f)^2/2\sigma_f^2} + (1-\theta) \times \frac{1}{\sigma_u \sqrt{2\pi}} e^{-(r-r_u)^2/2\sigma_u^2} \right) \cdot \left(\frac{\kappa}{r^6} + \frac{1}{T_{1s}^{\ o}} \right) \right\} - \frac{1}{T_{1s}^{\ o}} \right]^{-1/6} \quad (2\text{-}8)$$

In the non-cooperative model, folded residues and unfolded residues coexist in a peptide. The fractional helicity is then given by $\theta = k/M$ (*117*), where k is the number of contiguous helical residues in the peptide and M is the total number of residues. Todd and Millhauser (*116*) assumed that the helicity is less in the ends of a peptide compared with the central regions. This assumption is even more valid for our model system. Consequently, they defined the probability of the helical residue in the central regions, $P_H(\theta) = \frac{\theta}{1-\theta}$, when $\theta < 0.5$.

With this assumption the equilibrium constant is given by:

$$K = \frac{P_H(\theta)}{1 - P_H(\theta)} = \frac{\theta}{1-2\theta} \quad (2\text{-}9)$$

Thus, the average distance at a given temperature for the non-cooperative model, $r_{non\text{-}cooperative}$ is given by:

$$r_{non-cooperative} = \kappa^{1/6} \times \left[\left\{ \sum_{r_1}^{r_2} \left(\theta \times \frac{1}{\sigma_f \sqrt{2\pi}} e^{-(r-r_f)^2/2\sigma_f^2} + (1-2\theta) \times \frac{1}{\sigma_u \sqrt{2\pi}} e^{-(r-r_u)^2/2\sigma_u^2} \right) \cdot \left(\frac{\kappa}{r^6} + \frac{1}{T_{1s}^{\ o}} \right) \right\} - \frac{1}{T_{1s}^{\ o}} \right]^{-1/6} \quad (2\text{-}10)$$

The fractional helicity of the peptide was estimated from the mean residue ellipticity at 220 nm of the CD data (*118, 119*). The variables, r_f is a fullyfolded distance, r_u is a fullyunfolded distance and σ_f and σ_u are the standard deviation of the fullyfolded and fullyunfolded state, respectively. The other constants in equations 2-8 and 2-10 are explained in the equations 2-4 and 2-5. These four parameters were adjusted in order to fit with the measured ESR data and we found that the fullyfolded distance, r_f is correlated with σ_f and, the fullyunfolded distance, r_u is correlated with σ_u.

In general, a range of parameters provided satisfactory fit to the experimental distance changes with temperature and given that the experiments do not measure the distribution widths (σ_u and σ_f) no clear distinction between the two models could be obtained (cf. Figure 2-9).

2.5 DISCUSSION

We have been able to resolve the change in average distance as an alanine-based peptide melts with temperature. Each step of the folding pathway is encompassed by an ensemble of conformations, and these experiments capture the average separation between two units at each step. To infer the structural implications of these distances, we generated several ensembles with the polyalanine segments in α-helical conformations and in extended PPII conformations (cf. MATERIALS AND METHODS section). The average interspin distance in the α-helical ensembles was found to be ~25 Å, which is in good agreement with the experimental interspin distance of ~25 Å in the folded state of this alanine-based peptide. In the unfolded state, the ESR measured interspin distance was ~17 Å. Using single molecule fluorescence resonance energy

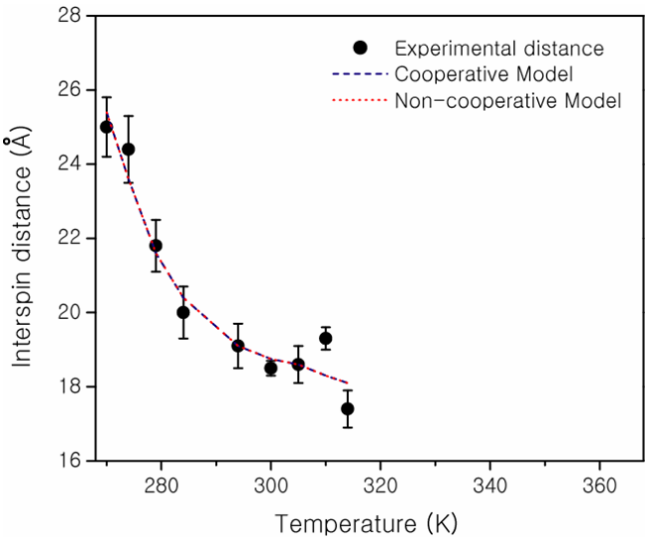

Figure 2-9: The Cu(II)-nitroxide interspin distances for the alanine-based peptide from 270 K and 314 K compared to expected distances for cooperative or non-cooperative unfolding transition model. The fitting parameters are $r_f \sim 27$ Å, $\sigma_f \sim 0.3$ Å, $r_u \sim 20$ Å, and $\sigma_u \sim 3$ Å for cooperative model, and $r_f \sim 17$ Å, $\sigma_f \sim 1.8$ Å, $r_u \sim 26$ Å, and $\sigma_u \sim 4.5$ Å for non-cooperative model, respectively. The range of parameters provides satisfactory fit to the experimental distance changes with temperature.

transfer (FRET), Gnanakaran et al. (*120*) measured the average end-to-end distance of the 20-residue alanine-based peptide to be ~30 Å in the folded α-helical conformation and ~23 Å in the unfolded state. The decrease of average distance upon unfolding observed by the FRET experiments is in agreement with the ESR results. The discrepancies in the actual distances are possibly due to differences in the amino acid sequences and in the lengths of the fluorescence tag versus the chelating residues.

The average distance should increase if the unfolded state of the alanine-based segment is in an extended PPII geometry. In fact, the average interspin distance in the PPII conformation in the molecular models is ~42 Å, which is not consistent with the experimental interspin distance of ~17 Å in the unfolded state. The presence of a distribution in distances is not sufficient to explain this discrepancy. Gnanakaran et al. (*120*) estimated that σ value of the peptide in the unfolded state is ~6.7 Å (the entire distribution ranges from 5 Å to 45 Å.). Given the smaller size of the spin label and based on this σ value, we anticipate $\sigma < 6.7$ Å for our peptide.

The average interspin distance in an extended PPII conformation in the molecular models was found to be ~42 Å. For an average distance of 42 Å, the ESR measured distances are estimated to be 40.6 Å, 39.7 Å, 38.4 Å, and 32.6 Å with $\sigma = 4$, 5, 6, and 6.7, respectively. The actual ESR measured average distance was 17 Å indicating that the peptide is not in an extended PPII conformation (cf. Figure 2-10).

Experimental evidence from NMR and UV Raman indicates that individual alanine residues sample Φ and Ψ Ramachandran angles close to those corresponding to a PPII conformation (*82, 83, 86*). However, the ESR experiments demonstrate that the PPII geometry does not propagate into an overall extended fold, at least over 10 amino acid residues. This is

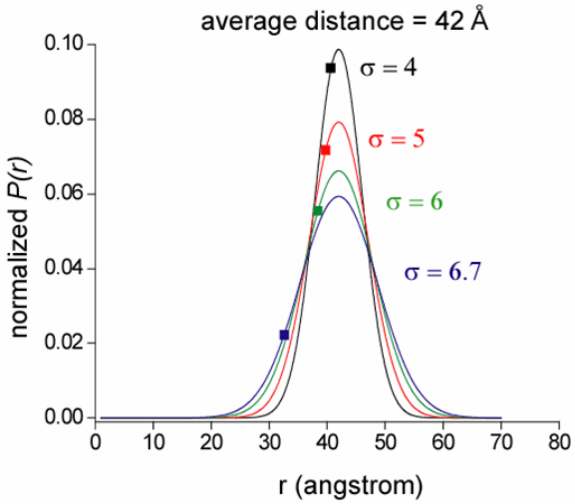

Figure 2-10: The comparison of the average distance from ESR distance measurements (shown by filled squares) for several standard deviations, σ = 4, 5, 6, or 6.7 Å at the actual average distance of 42 Å.

consistent with recent small-angle X-ray scattering results, which found that the radius of gyration of an unfolded polyalanine peptide is about 40 % lower than that expected of an extended PPII helix (*94*). Our experiments, however, do not rule out the possibility that the PPII geometry might extend over shorter stretches of amino acids. Future experiments which systematically scan the nitroxide along the chain will directly shed light on this issue. While useful in resolving the global structure of the peptides in the unfolded state, the experimental data cannot measure the full distribution in distances. Therefore, the experimental variation of average distances could not be used to provide further insight into the preferred model of folding. These results of the average interspin distances also address a critical need for ESR techniques that can measure nanometer scale distances at physiological temperatures. The experiments build on recent research that measured interspin distances by calibrating the nitroxide line broadening and line intensity due to interaction with a lanthanide (*121*), a paramagnetic metal (*79, 109, 122*), or another nitroxide (*12*). The distinct advantage of the continuous wave approaches is that widely available instrumentation and simple analysis can be used. The pulsed ESR results described in this paper are, nevertheless, encouraging. First, the method retains the advantage of a relatively straightforward analysis (*26, 35-37, 78*). Second, extension to larger distances might be possible given the enhanced sensitivity of FT-ESR to small changes in relaxation rates (especially homogeneous line widths). Third, the results describe an application of ESR to monitor unfolding transition in model peptides. They can be extended to more complicated folding processes in metalloproteins, as long as information on the relaxation rate of the metal is available. It is also instructive to compare this technique to fluorescence resonance energy transfer (FRET). While FRET can be sensitive to energy transfer over a larger length scale (ca. 10-12 nm), recent single molecule fluorescence results (*111*) clearly indicate that molecular

reorientations must be accounted for properly, to correctly interpret this energy transfer in terms of distances, even for polyproline peptides.

2.6 SUMMARY

Our pulsed ESR results demonstrate the potential for directly monitoring structural changes associated with the peptide unfolding under physiological conditions. In order to measure the unfolding transitions of the alanine-based peptide, we describe a scheme for tagging the peptide with a Cu(II) and a nitroxide and we show the enhancement in longitudinal relaxation rate of the nitroxide due to the presence of the fast relaxation of the paramagnetic metal, [Cu(II)]. This changes in relaxation rate of the nitroxide is inverted to measure the average interspin distance between Cu(II) and nitroxide. As the peptide unfolds with increasing temperature, the interspin distance, r_{ESR}, changes and we use the ESR distance measurement method to monitor structural changes associated with unfolding transitions. Data on a proline-based peptide, which forms a stable polyproline type II (PPII) structure, illustrates the robustness of the method. In the alanine-based peptide, the average interspin distance between Cu(II) and nitroxide decreases from 25 Å in the folded α-helical state to 17 Å in the unfolded state. From the molecular dynamic simulation, when the polyalanine peptides unfold to PPII structure, the average interspin distance is increased to 42 Å. As a conclusion, the ESR data shows that the unfolded state of this alanine-based peptide is not an ideal *extended* PPII geometry.

2.7 ACKNOWLEDGMENT

This work was supported by an NSF CAREER grant (MCB 0346898). We thank Prof. Sanford Asher for many helpful discussions.

3.0 THE AGGREGATED STATE OF AMYLOID-β PEPTIDE IN VITRO DEPENDS ON Cu(II) ION CONCENTRATION

Part of this work, written in collaboration with Sunil Saxena, has been published in the Angewandte Chemie International Edition, 2007, V.46, (a) pages 3959-3961 and (b) page 5263 (123).

3.1 ABSTRACT

In this work, we demonstrate a direct correlation between Cu(II) coordination in Aβ aggregates and the overall morphology of Aβ aggregates. The Cu(II) environment in aggregated Aβ was probed by continuous wave (CW) electron spin resonance (ESR) and pulsed electron spin echo envelope modulation (ESEEM) ESR spectroscopy. At the same time, transmission electron microscopy (TEM) images were obtained in order to determine overall morphology of the aggregates. At low [Cu(II)]:[Aβ] ratios the Cu(II) is coordinated to at least one histidine in the Aβ peptide in the aggregated state. This coordination weakens as the [Cu(II)]:[Aβ] ratio increases and the metal becomes increasingly exposed to either exchangeable hydrogens or water. These results were obtained on a Tris buffer. Images obtained using TEM indicate that at low concentrations of Cu(II) the aggregates are mature fibrils while at high Cu(II) concentration granular aggregates result whose morphology resembles that of early stage aggregates. Both ESR

and TEM results suggest that the misfolding mechanism of Aβ is dependent on Cu(II) ion concentration.

3.2 INTRODUCTION

Despite significant progress, there is still uncertainty about the molecular basis for the onset of Alzheimer's disease (AD). The misfolding of amyloid-β peptide (Aβ), wherein soluble peptide aggregates form plaques in the neuropil, is central to this process. Recent research indicates that intermediates of Aβ formed at the early stages of aggregation of Aβ are more toxic than the fully formed fibrils (*124, 125*). A leading hypothesis for the toxicity is the generation of hydrogen peroxide during the early stages of aggregation (*125*). Results in vitro indicate that metal ions like Cu(II) and Zn(II) ions affect the rate of formation of fibrils (*126, 127*). Even more intriguingly, it is believed that Cu(II) ions stabilize the toxic early-stage aggregates of Aβ (*128-130*), whereas Zn(II) ions rapidly induce the Aβ amyloid formation (*126*). The concentrations of Cu(II) and Zn(II) ions in plaques found in the brains of Alzheimer's patients are as high as 400 - 1000 μM (*131, 132*), which suggests that the results in vitro have real significance in vivo (*131*). Given that the physiological concentration of Aβ(1−40) is believed to be 15 μM (*133*), it is interesting to systematically examine the role of metal ions in Aβ aggregation, especially at high copper concentrations. Herein, we show that the copper-binding geometry in aggregated Aβ changes with copper concentration. The overall morphology of the aggregates also depends on the concentration of Cu(II) ions. Together, the data suggest that microscopic metal–Aβ

interactions play a major role in dictating the aggregated state of Aβ. Our results also indicate that the misfolding mechanism of Aβ is dependent on the concentration of Cu(II) ions.

3.3 MATERIALS AND METHODS

● *Sample Preparation*

Hexafluoroisopropanol (HFIP) treated Aβ(1–40) (Asp-Ala-Glu-Phe-Arg-His-Asp-Ser-Gly-Tyr-Glu-Val-His-His-Gln-Lys-Leu-Val-Phe-Phe-Ala-Glu-Asp-Val-Gly-Ser-Asn-Lys-Gly-Ala-Ile-Ile-Gly-Leu-Met-Val-Gly-Gly-Val-Val) was purchased from rPeptide and was > 97% pure. The peptide was resuspended in 1% NH_4OH, at a concentration of 1mg/ml. After resuspension, sample of soluble Aβ was prepared by adding buffer containing 100 mM Tris, 150 mM NaCl, and a pH of 7.4. The peptide concentration was determined using a calibration curve generated with BSA (bovine serum albumin) standards. To prepare aggregates, Aβ(1–40) was incubated at 37 °C for 4 - 5 days in the presence of appropriate Cu(II) concentration. Based on the circular dichroism data, the 4 - 5 days were sufficient to form aggregates.

● *Circular Dichroism (CD) Spectroscopy*

The β-sheet conformation of Aβ(1–40) aggregates was monitored with CD spectroscopy. The peptide was dissolved in 25 mM MES buffer, a pH of 6, and at peptide concentration of 29 μM. Spectra were recorded on an AVIV model 202 circular dichroism spectrometer over the wavelength range of 195–255 nm with a step size of 1 nm, a 1 nm bandwidth, and a scan rate of

2 nm/sec. The first spectral curve was obtained 26 minutes after starting fibril formation and the formation of Aβ fibrils under this condition takes ~ 1500 min. (cf. Figure 3-6a).

● *Thioflavin-T (ThT) Fluorescence Measurements*

In order to determine Aβ(1−40) fibril growth endpoints, fluorescence measurements were performed on HORIBA Jobin Yvon FluoroMax-3 fluorescence spectrometer at an excitation of 440 nm and emission of 483 nm. A 1.5 μM ThT solution at pH 7.4 was prepared by dissolving solid ThT (Acros Organics) in a Tris buffer and the 100 μM Aβ solution in the presence of a range of Cu(II) ion concentrations of 15 μl was added to 2 ml of the ThT solution. The sample was placed in a quartz cell with a 1 cm path length for the measurements.

● *Electron Spin Resonance (ESR) Spectroscopy*

Spectroscopic experiments were performed on a Bruker EleXsys E580 X-band CW/Pulse ESR spectrometer equipped with a Bruker ER 4118X-MS3 split-ring or a ER 4118X-MD5 dielectric resonator. The temperature was controlled using an Oxford ITC503 temperature controller and an Oxford ER 4118CF gas flow cryostat.

All continuous wave (CW) – ESR spectra were collected at 80 K, with microwave power = 1.993 mW, modulation amplitude = 1 G, time constant = 40.96 ms, conversion time = 81.92 ms, and a sweep width of 1200 G. Three-pulse electron spin echo envelope modulation (ESEEM) ESR spectra of aggregated Aβ(1–40) were collected at 20 K by using a $\pi/2–\tau–\pi/2–T–\pi/2$ pulse sequence with a $\pi/2$ pulse width = 16 ns, τ = 120 ns, T increment = 16 ns, and 100 averages per point.

● *Transmission Electron Microscopy (TEM)*

Samples were prepared on 200-mesh formvar films coated with a layer of carbon and negatively stained with 1% uranyl acetate. The images were collected with a FEI Morgagni 268 transmission electron microscope at University of Pittsburgh, Department of Biological Sciences.

3.4 RESULTS AND DISCUSSION

Figure 3-1 shows the continuous wave (CW) electron spin resonance (ESR) spectra of Cu(II) ions bound to Aβ(1–40) aggregates at three different metal/peptide ratios. To prepare aggregates, Aβ(1–40) was incubated at 37 °C for 4 – 5 days in the presence of an appropriate concentration of Cu(II) ions. The CW-ESR spectra provide information on strong interactions between the Cu(II) electron and neighboring nuclei (cf. Figure 1-6a). The magnitude of $g_{||}$ (the parallel component of the axially symmetric g tensor) and $A_{||}$ (the parallel component of the hyperfine interaction) are dependent on, among many factors, the ligand environment of Cu(II) ions (*45*). Peisach and Blumberg have described how $g_{||}$ and $A_{||}$ are used for the assignment of coordinating nitrogen and oxygen atoms of the copper binding site (cf. Figure 1-7) (*45*).

At low [Cu(II)]:[Aβ] ratios (shown in Figure 3-1a), the spectrum has the value, $g_{||} = 2.27$ and $A_{||} = 160$ G (= 15 mK), which suggests that the Cu(II) ion has a three nitrogen and one oxygen coordination environment (3N1O) (*45, 46, 53*). Recently, Shin and Saxena used isotopic ^{15}N labeled peptides to demonstrate that this site is coordinated by all three histidine residues (H6, H13, and H14) (*134*). With increasing amounts of Cu(II) ions, a new set of hyperfine lines, shown by the dashed lines in Figure 3-1, is observed. These lines have a $g_{||} = 2.24$ and $A_{||} = 190$

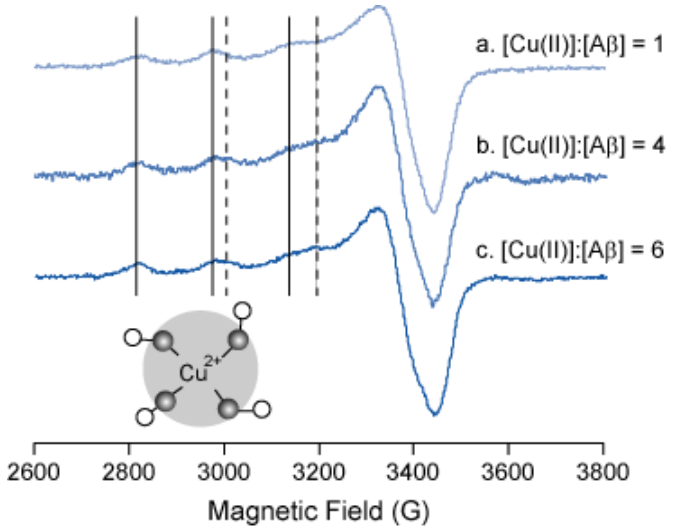

Figure 3-1: CW-ESR spectra of Cu(II) ions in aggregates of Aβ(1–40). The spectra are at [Cu(II)]:[Aβ] molar ratios of (a) 1, (b) 4, and (c) 6. With increasing amounts of Cu(II) ions, a new set of hyperfine lines, shown by the dashed lines, is observed. Peptide concentrations are 100 μM in all experiments.

G (= 17.8 mK) (Figure 3-1b and c), which can be assigned within any range of the four different coordinating environments, 4N, 3N1O, 2N2O, or 1N3O (*45, 46, 53*) (cf. Figure 1-7). This potential ambiguity was overcome by Barnham and co-workers. In a recent paper, they have used multifrequency CW-ESR spectroscopy using site-specific ^{15}N-labeling in order to demonstrate two different 3N1O Cu(II) coordinations in Aβ (*135*). Kowalik-Jankowska and co-workers also supported two different 3N1O Cu(II) binding sites using potentiometric and spectroscopic methods (*136*).

The CW-ESR results are complemented by pulsed electron spin echo envelope modulation (ESEEM) ESR spectroscopy, which probes the interactions of the electron spin with more distant nuclei (cf. Figure 1-6b). The field-swept echo-detected experiment was performed in order to determine the appropriate magnetic field position for the ESEEM experiment. Three pulse ESEEM spectra obtained at 20 K at the $g_{\perp}$ region (corresponding to the absorption maximum) of the field-swept echo-detected spectra are shown in Figure 3-2. Figure 3-3 shows the three-pulse ESEEM spectra of five different Cu(II) ion concentrations on Aβ(1–40). In Figure 3-3a, the ESEEM spectrum of [Cu(II)]:[Aβ] at a ratio of 0.2 contains peaks below 5 MHz. The three-pulse ESEEM experiment detects the modulation of the Cu(II) spin echo from the ^{14}N nuclei (I = 1) of surrounding amino acids, and the remote nitrogen of the histidine imidazole provides characteristic frequencies in the ESEEM spectrum (*46, 48, 53*). In Figure 3-3a, the peaks below 2 MHz can be assigned to a nuclear quadrupole interaction and the peak around 4 MHz is due to a double quantum transition of the remote nitrogen of the histidine imadazole (*46, 48, 53*). This is direct evidence that the Cu(II) ion is bound to the N-terminal region of Aβ(1–40), which includes three histidines (H6, H13, and H14), as has been proposed before by the work of Syme et al. and Karr et al (*137, 138*).

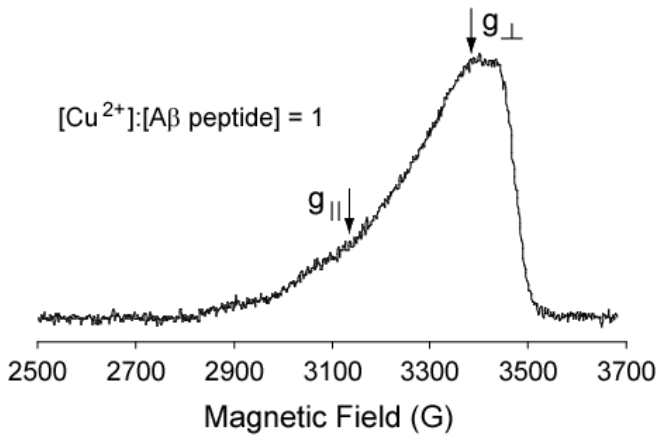

Figure 3-2: Field-swept echo-detected spectrum at a [Cu(II)]:[Aβ] ratio of 1. The $g_{\|}$ and $g_{\perp}$ regions of the absorption spectrum are roughly indicated.

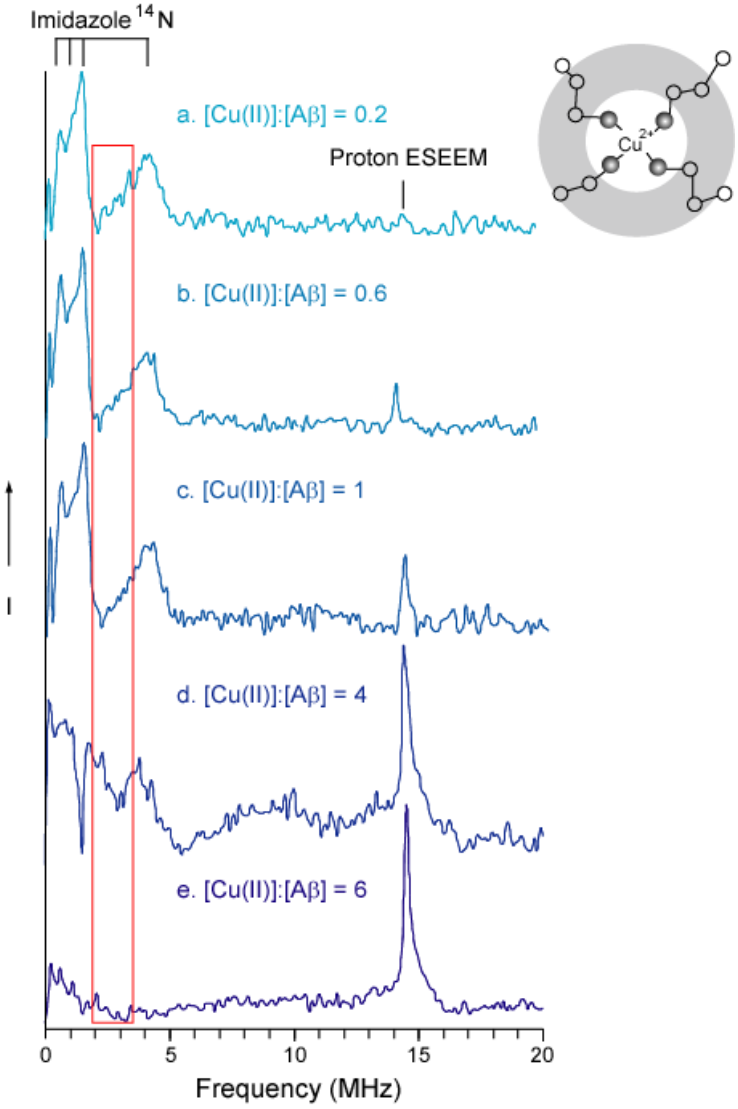

Figure 3-3: Three-pulse ESEEM spectra of aggregated Aβ(1–40). The data are at Cu(II) ion to peptide ratios of (a) 0.2, (b) 0.6, (c) 1, (d) 4, and (e) 6. At low [Cu(II)]:[Aβ] ratios, the peaks below 5 MHz indicate that the Cu(II) ion is coordinated to at least one histidine of the Aβ peptide. This coordination weakens as the [Cu(II)]:[Aβ] ratio increases. Peptide concentrations are 100 μM in all experiments.

The presence of spectral features between 2 – 4 MHz indicates that electron spin of the Cu(II) ion interacts with more than one nitrogen, which is consistent with interaction with multiple histidines (*50*). The Cu(II) ion coordination might also be associated with the ^{14}N of the neighboring amide bonds (*53*). Indeed, NMR experiments suggest that the amide bond between E3 - V18 may be involved in metal binding (*139*). The large line widths indicate that the Cu(II) ion coordination environment is heterogeneous.

Systematic ESEEM experiments indicate that the peaks below 5 MHz become broader as the Cu(II) ion concentration increases, and the peaks therefore have increasingly lower amplitudes. Figure 3-4 shows the three pulse ESEEM spectra obtained at three different magnetic fields for Aβ(1–40) assembled with a [Cu(II)]:[Aβ] ratio of 6. These data provide more evidence for peak broadening below 5 MHz. The peaks below 5 MHz are very broad indicating that the 3N1O coordination becomes more heterogeneous at this ratio. Furthermore, another peak at approximately 14 MHz emerges clearly. Figure 3-3d shows the results at a [Cu(II)]:[Aβ] ratio of 4. The peak at 14 MHz, in addition to the peaks below 5 MHz, is clear. In Figure 3-3e, where the [Cu(II)]:[Aβ] ratio is 6, the peak at approximately 14 MHz is dominant. The 14 MHz peak is characteristic of electron–nuclear interactions between the unpaired electron and proton spins (note that ESEEM does not probe directly coordinated nuclei, shown in red region in Figure 1-6b) (*140*). The 14 MHz proton ESEEM peak in Figure 3-3e is eliminated when the sample is prepared in D_2O, indicating that the peak is due to the interaction with hydrogen from the solvent or from exchangeable protons (cf. Figure 3-5). Together, the CW-ESR and ESEEM results suggest that the 3N1O coordination becomes more heterogeneous and water accessible as the [Cu(II)]:[Aβ] ratio increases.

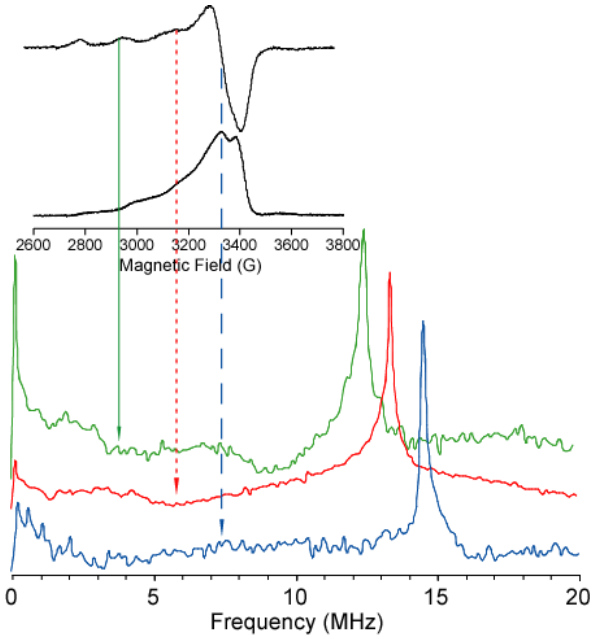

Figure 3-4: Three pulse ESEEM spectra at three different magnetic fields with a [Cu(II)]:[Aβ] ratio of 6. The ESEEM peaks are broader at this ratio compared with at low Cu(II) concentration indicating that the Cu(II) coordination in Aβ(1−40) weakens as the [Cu(II)]:[Aβ] ratio increases.

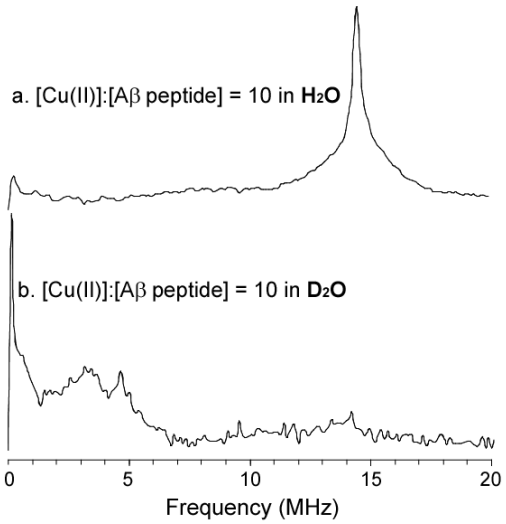

Figure 3-5: Three pulse ESEEM spectra of Aβ(1−40) assembled with Cu(II) to peptide ratio of 10 in (a) H_2O and (b) D_2O. The 14 MHz proton ESEEM peak is eliminated in D_2O suggesting that the peak is from the interaction with hydrogen of solvent.

In order to investigate the formation of the β-sheet structures in Aβ(1–40), the secondary structure of Aβ in the absence of Cu(II) was monitored using circular dichroism (CD) spectroscopy. Initially, the spectral curve of Aβ has a minimum mean residue ellipticity at 197 nm as shown in Figure 3-6a. This peak is characteristic of an unordered backbone structure. As time increases the peak at 197 nm grows more positive and the peak at 220 nm becomes more negative, indicating that Aβ undergoes a conformational transition into a β-sheet structure. In addition, the formation of β-sheet structure for Aβ at different Cu(II) ion concentrations as a function of time was examined at a single wavelength, 220 nm. As shown in Figure 3-6b, Aβ(1−40), in the absence of Cu(II), forms significant β-sheet content over a slower timescale. At high Cu(II) ion concentrations the rapid assembly is accompanied with a decreased amount of β-sheet content. This result indicates that at high concentration of Cu(II) ions, such as a [Cu(II)]:[Aβ] ratio of 6 or 10, the Cu(II) ion affects the formation of the β-sheet structures in Aβ aggregates.

TEM images of the aggregated state of Aβ demonstrate a transition with an increasing Cu(II) ion concentration. In Figures 3-7a,b and c, at low concentrations of Cu(II) ions, the TEM image shows that Aβ(1–40) forms fibrillar precipitates that have an extensive linear shape. At high Cu(II) ion concentrations (Figure 3-7f), short and granular aggregates result, and this morphology resembles that of previously described early-stage intermediates (*125, 141*). At 2 mol equivalents of Cu(II) to the peptide (see Figure 3-7d) both linear fibrils and granular aggregates are observed. The total Aβ(1–40) fibril content was also assessed with the thioflavin-T (ThT) fluorescence measurements. When the Aβ(1–40) forms the aggregates with increasing concentration of Cu(II) ions, ThT fluorescence intensity is decreased, indicating a loss of Aβ(1–40) fibrils (cf. Figure 3-8).

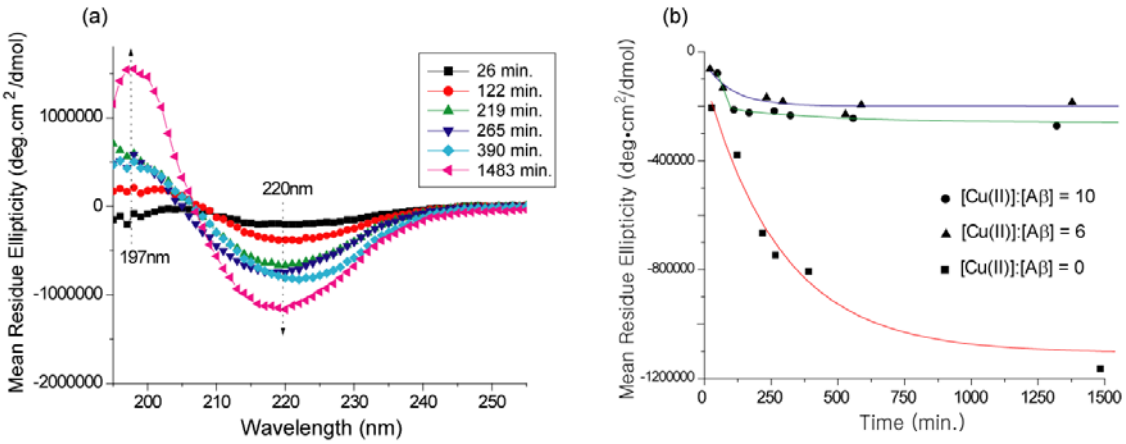

Figure 3-6: (a) CD spectra of Aβ(1–40) in the absence of Cu(II) over time. (b) Mean residue ellipticity at 220 nm as a function of time for Aβ in the presence of different Cu(II) ion concentrations. Aβ undergoes a conformational transition from a random coil to a β-sheet structure. Peptide concentrations are 29 μM in all experiments.

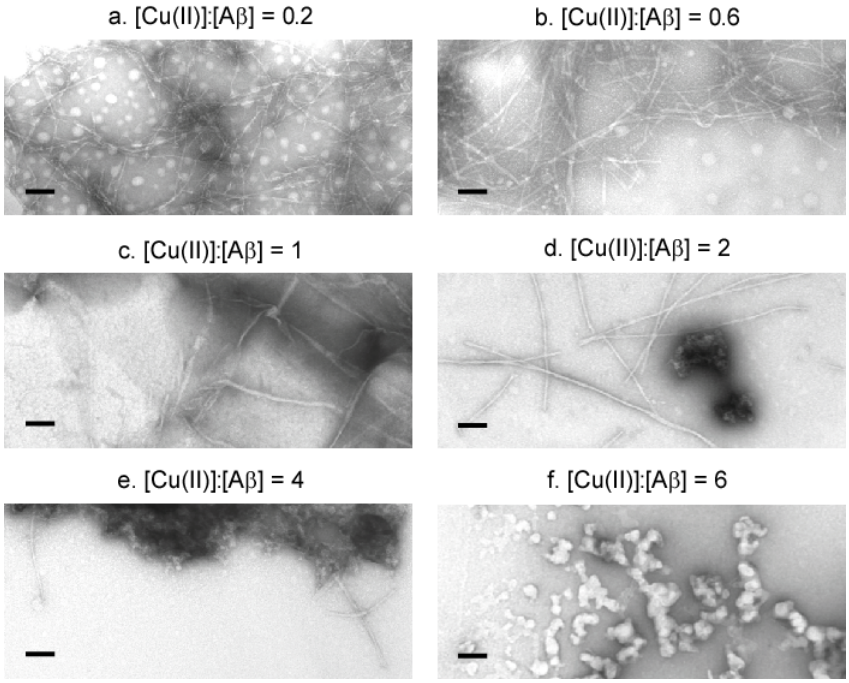

Figure 3-7: Negatively stained TEM images of aggregated Aβ(1–40). The scale bars correspond to 100 nm. The images are for aggregates prepared at [Cu(II)]:[Aβ] ratios of (a) 0.2, (b) 0.6, (c) 1, (d) 2, (e) 4 and (f) 6 at 37 °C for 4–5 days. The overall morphology changes as the concentration of the Cu(II) ions increases.

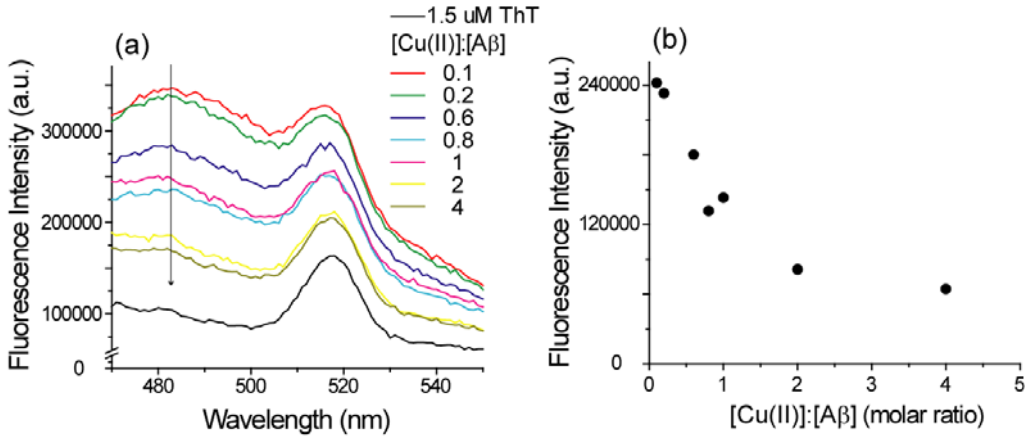

Figure 3-8: (a) ThT fluorescence emission spectra of Aβ(1–40) and (b) ThT fluorescence intensity at 483 nm of Aβ(1–40) at a range of [Cu(II)]:[Aβ] ratio. ThT fluorescence intensity at 483 nm is decreased as the Cu(II) concentration increases, indicating a loss of fibril.

The phase memory time, T_m, was also obtained from Aβ(1–40) aggregates at different Cu(II) ion concentrations. As shown in Figure 3-9, the T_m substantially increases up to 2 equivalents of Cu(II) ion and then plateaus with a T_m value of approximately 4000 ns. In the presence of an equimolar or subequimolar amount of Cu(II), the TEM images showed only fibrils. However, at [Cu(II)]:[Aβ] ratio of 2 or greater, both fibrils and granular aggregates were observed in the TEM images. Together, the data suggests that the T_m of the granular aggregates is longer than that of the fibrils and demonstrates the correlation between the T_m and overall morphology of Aβ(1–40).

The changes in morphology of aggregated Aβ with Cu(II) ions are different from those observed for the case of Zn(II) ions. Lynn and co-workers showed that the fibril morphology changes from a thin-linear shape to thick ribbons as the [Zn(II)]:[Aβ] ratio increases (*142*). These differences in morphology might be due to the different coordination environments of the two metals. At a pH value of 7.4, the Zn(II) ion binding site involves inter-peptide interactions and is believed to lie between two different peptide sheets (*128, 143*). The Cu(II) ion binding geometry is largely intra-peptide in nature (*128, 143*), especially at low Cu(II) ion concentrations as demonstrated by the ESR results (Figures 3-1 and 3-3).

As a conclusion, our ESR and TEM results demonstrate a correlation between specific Cu(II) ion coordination and the overall morphology of aggregates. At low [Cu(II)]:[Aβ] ratios, the Cu(II) ion is coordinated to the histidine(s) of the Aβ peptide. As the [Cu(II)]:[Aβ] ratio increases, this coordination becomes more heterogeneous and the metal becomes exposed to water or to exchangeable protons on the peptide. Images obtained by using TEM indicate that at low concentrations of Cu(II) ions, the aggregates are mature fibrils, whereas at high Cu(II) ion concentrations, granular aggregates result. Together, these data suggest that the misfolding

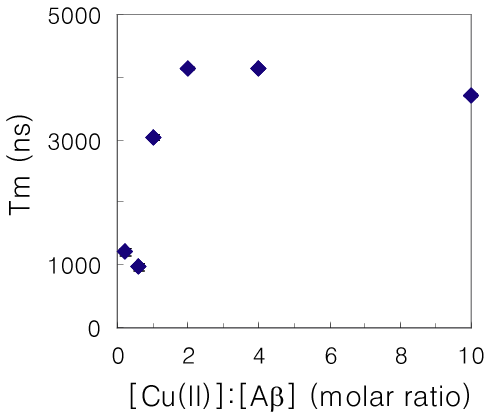

Figure 3-9: The phase memory time, T_m plotted versus molar ratio of Cu(II) ions to Aβ(1–40).

mechanism is dependent on Cu(II) ion concentration.

It is believed that the misfolding of Aβ proceeds via the rapid formation of early stage intermediates (*141*). Over a slower timescale these intermediates aggregate to form mature fibrils. The sequence is shown in Figure 3-10. Metal ions like Zn(II) and Cu(II) are believed to stabilize the early stage intermediates. Our results, illustrated in Figure 3-10, indicate that the eventual morphology of the aggregates depends on the concentration of Cu(II) – granular aggregates form at high Cu(II) concentrations while mature fibrils at low metal concentrations. The overall morphology as revealed by TEM images of the granular aggregates is similar to the morphology of early stage toxic intermediates. Our data also indicates that the Cu(II) binding environment in the granular early stage aggregates is distinctly different from the binding environment in mature fibrils. This suggests that microscopic metal - Aβ interactions play a major role in dictating the eventual morphology of Aβ aggregates. A systematic understanding of the atomic level structural details of Cu(II) - Aβ interactions is necessary in order to shed light on the mechanism of Aβ misfolding. The results will aid in the development of chelation approaches for therapy as well as improve our understanding of the biochemical basis for toxicity.

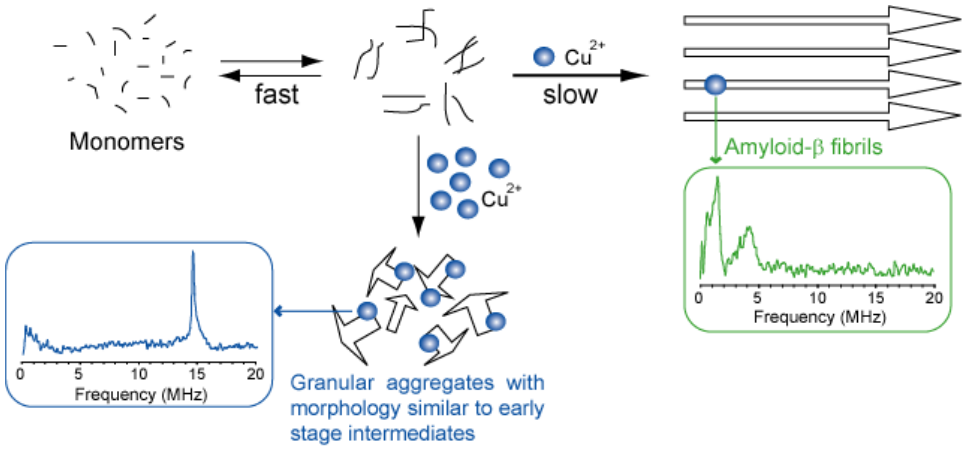

Figure 3-10: Aβ monomers rapidly form early stage aggregates which eventually form mature fibrils. Our results indicate that Cu(II) binds in different environments in the early stage intermediates versus fully formed fibrils.

3.5 ACKNOWLEDGMENT

This work was supported by an NSF CAREER grant (MCB 0346898). We also thank Tom Harper for access to a transmission electron microscope.

4.0 THE SECOND Cu(II)-BINDING SITE IN A PROTON-RICH ENVIRONMENT INTERFERES WITH THE AGGREGATION OF AMYLOID-β (1–40) INTO AMYLOID FIBRILS

This work, written in collaboration with Joel R. Gillespie, Byong-kyu Shin, and Sunil Saxena, has been published in Biochemistry, 2009, V.48, pages 10724-10732 (144).

4.1 ABSTRACT

The overall morphology and Cu(II) ion coordination for the aggregated amyloid-β(1–40) [Aβ(1–40)] in N-ethylmorpholine (NEM) buffer are affected by Cu(II) ion concentration. This effect is investigated by transmission electron microscopy (TEM), atomic force microscopy (AFM), and electron spin echo envelope modulation (ESEEM) spectroscopy. At lower than equimolar concentrations of Cu(II) ions, fibrillar aggregates of Aβ(1–40) are observed. At these concentrations of Cu(II), the monomeric and fibrillar Aβ(1–40) ESEEM data indicate that the Cu(II) ion is coordinated by histidine residues. For aggregated Aβ(1–40) at a Cu(II):Aβ molar ratio of 2:1, TEM and AFM images show both linear fibrils and granular amorphous aggregates. The ESEEM spectra show that the multi-histidine coordination for Cu(II) ion partially breaks up and becomes exposed to water or exchangeable protons of the peptide at a higher Cu(II)

concentration. Since the continuous-wave electron spin resonance results also suggest two copper-binding sites in Aβ(1–40), the proton ESEEM peak may arise from the second copper-binding site, which may be significantly involved in the formation of granular amorphous aggregates. Thioflavin T fluorescence and circular dichroism experiments also show that Cu(II) inhibits the formation of fibrils and induces a nonfibrillar β-sheet conformation. Therefore, we hypothesize that Aβ(1–40) has a second copper-binding site in a proton-rich environment and the second binding Cu(II) ion interferes with a conformational transition into amyloid fibrils, inducing the formation of granular amorphous aggregates.

4.2 INTRODUCTION

Amyloid-β (Aβ) peptide, a small peptide that is composed of 39–43 amino acids, is the main constituent of amyloid deposits found in Alzheimer's Disease (AD) (*145*). This peptide exists as a normal soluble random coil and undergoes a conformational transition to an insoluble aggregated, fibrillar β-sheet-rich form. It is believed that the progression of AD is correlated with the Aβ intermediates rather than the amyloid plaques (*141, 145-148*) and that Cu(II) stabilizes the neurotoxic early-stage intermediates of Aβ (*128-130*). Since this neurotoxicity is dependent partly on the state of aggregation in Aβ, one of the goals in Aβ research is focused on characterizing the copper coordination, which can be involved in promoting (*132*) or inhibiting (*127, 129, 130*) amyloid fibril formation.

Electron spin resonance (ESR) spectroscopy has shown that Cu(II) is coordinated with histidine residues in the flexible N-terminal region of Aβ. A smaller fragment, Aβ(1–16), has

been considered as a suitable model for investigation of Cu(II) ion coordination (*149, 150*). The peptide, Aβ(1–16), is not aggregated at physiological pH and is traditionally believed to have a copper coordination geometry identical to that of the longer, fibril-forming peptides, Aβ(1–40) and Aβ(1–42). We have used isotopic ^{15}N-labeled peptides to demonstrate that the copper-binding site in Aβ(1–16) is coordinated by all three histidine residues (H6, H13, and H14), providing three nitrogen donors to the Cu(II) ion (*134*). Barnham and co-workers have used multifrequency continuous-wave (CW) ESR spectroscopy to resolve the superhyperfine interaction between the Cu(II) ion and the ligand nuclei of Aβ via selective ^{15}N labeling of specific ligand nuclei. They have also demonstrated two different 3N1O Cu(II) coordination environments involving D1, H6, H13, or H14 in Aβ(1–16) (*135*). However, the longer peptide, Aβ(1–40), includes Aβ(17–21), which is known to be crucial for fibril formation (*151-155*). In recent reports, there has been evidence of additional binding sites in longer sequences of Aβ. In particular, Viles and co-workers reported that Aβ(1–28) has two copper-binding sites for a single peptide (*137*) and, recently, demonstrated that two copper-binding sites are present in Aβ(1–42) in a water/methanol mixture (80:20, v/v) (*150*). Bush and co-workers also demonstrated two cooperative copper-binding sites in Aβ(1–40) at pH 7.4 (*156*). Intriguingly Aβ(1–40) forms granular amorphous aggregates instead of amyloid fibrils at greater than equimolar Cu(II) ion concentrations (*123, 157*).

In this study, we suggest two copper-binding sites in the Aβ(1–40) aggregates and provide evidence that the second copper-binding site interferes with the conformational transition into amyloid fibrils. By preparing aggregates at different Cu(II) concentrations, we systematically examine different morphological species of Aβ(1–40), such as monomers, fibrils and amorphous aggregates, by a variety of spectroscopic and imaging techniques. We

demonstrate that greater than equimolar Cu(II) concentrations disrupt the formation of regular amyloid fibrils in favor of granular amorphous aggregates based on transmission electron microscopy (TEM) and atomic force microscopy (AFM) images, reduced thioflavin T (ThT) fluorescence emission, and alterations of the far-UV circular dichrosim (CD) spectrum of the peptide. The electron spin echo envelope modulation (ESEEM) spectra for different aggregated stages of Aβ(1–40) in *N*-ethylmorpholine (NEM) buffer suggest that the copper coordination environments of monomers and mature fibrils are identical (*149, 150*). On the other hand, distinct differences between the copper coordination environment of monomers and amorphous aggregates of Aβ(1–40) exist. The aggregates of Aβ(1–40) have a second copper-binding site, which is exposed to a proton-rich environment. Potentially this site disrupts protein–protein interactions that lead to formation of fibrils.

4.3 MATERIALS AND METHODS

● *Sample Preparation*

Aβ(1–40) (DAEFRHDSGYEVHHQKLVFFAEDVGSNKGAIIGLMVGGVV) was synthesized at the Molecular Medicine Institute, University of Pittsburgh, using standard fluorenylmethoxycarbonyl chemistry. Aβ(1−40) was purified by high-performance liquid chromatography and characterized by mass spectrometry. The peptide was dissolved in 1% NH_4OH, and the pH value was adjusted to 7.4 with hydrochloric acid. The Aβ(1–40) solution was diluted to the final concentration of 300 μM with a pH 7.4 buffer solution containing 50 mM NEM and 25% (v/v) glycerol. Isotopically enriched (98.6%) $^{63}CuCl_2$ was purchased from

Cambridge Isotope Laboratory (Andover, MA) and a Cu(II) solution was prepared in the same NEM buffer. The enriched isotope was used to minimize inhomogeneous broadening of the Cu(II) ESR spectra. To prepare aggregates, Aβ(1–40) was incubated at 37 °C for several days in the presence of appropriate Cu(II) concentration.

● *Electron Spin Resonance Spectroscopy*

For pulsed ESR experiments, 150 μL of peptide solution was transferred into a quartz tube with an inner diameter of 3 mm. All experiments were performed on a Bruker EleXsys E580 X-band CW/Pulse ESR spectrometer equipped with a Bruker ER4118X-MD5 dielectric ring resonator. The temperature was controlled using an Oxford ITC503 temperature controller and an Oxford ER 4118CF gas flow cryostat.

Three-pulse ESEEM spectra of the Aβ(1–40) were recorded at 20 K by using a $\pi/2 - \tau - \pi/2 - T - \pi/2$ pulse sequence with a $\pi/2$ pulse width of 16 ns. The first pulse separation, τ, was set at 200 ns, and the second pulse separation, T, was varied from 400 ns with a step size of 16 ns for a total of 1024 points with 100 averages collected per point. The unwanted signals were eliminated by a four-step phase cycle (*158, 159*). The data were baseline-corrected and Fourier-transformed to produce the ESEEM spectra. The magnitude of the FT data is shown for all ESEEM spectra.

Hyperfine sublevel correlation (HYSCORE) experiments were also performed with Aβ(1–40) at 20 K by using a $\pi/2 - \tau - \pi/2 - t_1 - \pi - t_2 - \pi/2$ pulse sequence with $\pi/2$ and π pulse widths of 16 ns and 32 ns, respectively. The first pulse separation, τ, was set at 200 ns, and both the second and third pulse separations, t_1 and t_2, respectively, were varied from 200 ns with a step size of 16 ns and 100 averages per point. The final data consisted of 256 points in both t_1

and t_2. The data were baseline-corrected, zero-filled to 512 points, and Fourier-transformed to produce the HYSCORE spectra.

For CW ESR experiments, 30 μL of suspended aggregated peptide was transferred into a quartz tube with an inner diameter of 2 mm (Vitrocom, Mountain Lakes, NJ). All CW ESR spectra were recorded at 80 K with a microwave power of 0.1993 mW, a modulation amplitude of 4 G, a time constant of 40.96 ms, a conversion time of 81.92 ms, and a sweep width of 2000 G.

● *Thioflavin T Fluorescence Assays*

To determine the Aβ(1–40) fibril growth endpoints, fluorescence measurements were performed on a HORIBA Jobin Yvon FluoroMax-3 fluorescence spectrometer at an excitation of 440 nm (bandwidth of 5 nm) and emission of 485 nm (bandwidth of 5 nm). A 3 μM ThT solution at pH 8.6 was prepared by dissolving solid ThT (Acros Organics USA, Morris Plains, NJ) in a 50 mM glycine-NaOH buffer (*160*) and stored in a brown bottle to prevent degradation by light. A 13 μL aliquot of the 300 μM Aβ(1–40) solution in the presence of a range of Cu(II) ion concentrations was added to 3 mL of the ThT solution. The sample was placed in a quartz cell with a path length of 1 cm (NSG Precision Cells Inc., Farmingdale, NY) for the measurements.

● *Circular Dichroism Spectroscopy*

The β-sheet conformation of Aβ(1–40) was monitored with CD spectroscopy. The Aβ(1–40) sample was diluted to a final concentration of 28 μM with NEM buffer. Spectra were recorded on an AVIV model 202 circular dichroism spectrometer over the wavelength range of 198–270 nm with a step size of 1 nm, a 1 nm bandwidth, and a scan rate of 2 nm/s. The temperature was fixed at 25 °C using the temperature control. The samples contained 400 μL of

the peptide solution in a 0.1 cm path length quartz cuvette. The background was subtracted from each spectrum, but no additional filtering or noise reduction was applied.

● *Transmission Electron Microscopy*

Peptide samples were prepared on 200 mesh copper grids coated with Formvar support films stabilized with a layer of carbon (Ted Pella, Inc., Redding, CA). Samples were applied either with a jet sprayer or by the droplet method (*161*) and were negatively stained with a solution of 1% uranyl acetate. Images were collected with a FEI Morgagni 268 transmission electron microscope operating at 80 keV at the Department of Biological Sciences (University of Pittsburgh) or a JEOL JEM-2100F high-resolution field emission transmission electron microscope operating at 200 keV at the Peterson Institute for Nanoscience Nanoscale Fabrication and Characterization Facility.

● *Atomic Force Microscopy*

Each of the Aβ(1–40) samples was diluted to ~ 1 or 2 μM with deionized water in an Eppendorf tube, and aliquots of 5 μL were removed from the diluted solution and placed on a freshly cleaved mica surface and air-dried. All images were obtained under ambient conditions with a Veeco Nanoscope IIIA atomic force microscope with a Dimension 3100 controller (Veeco Metrology Inc., Santa Barbara, CA) operating in tapping mode using sharp diamond probes (series DP15, MikroMasch USA, San Jose, CA). Scanning parameters varied with individual tips and samples, but typical values were as follows: setpoint, 1.1–1.3 V; tapping frequency, 290–330 kHz; scan rate, 1 Hz. The AFM image processing and analysis were performed using ImageJ (*162*).

4.4 RESULTS AND DISCUSSION

● *The morphology of Aβ (1–40) aggregates is altered by the Cu(II) ion concentration in NEM buffer.*

We have already demonstrated a direct correlation between the overall morphology of Aβ(1–40) aggregates and the specific Cu(II) coordination in the Aβ(1–40) aggregates in our previous work (*123*). The ESR results were all obtained from Aβ(1–40) in Tris buffer, which might contain a signal from aqueous Cu(II). To investigate the effect of buffer on the overall morphology and the ESEEM signal of Aβ(1–40), we prepared the peptide samples in *N*-ethylmorpholine (NEM), and compared the data with those collected in Tris buffer. It is known that NEM buffer minimizes the ESR signal from aqueous Cu(II) ions at neutral pH (~ 7.4) (*46*).

The overall morphology of mature aggregated Aβ(1–40) in NEM buffer was examined by high-resolution transmission electron microscopy (TEM) and atomic force microscopy (AFM) imaging. To prepare aggregates, Aβ(1–40) was incubated at 37 °C for 5–6 days in the presence of an appropriate Cu(II) concentration. In the presence of an equimolar or subequimolar amount of Cu(II), the peptide exclusively forms fibrillar precipitates that have an extensive nonbranching linear shape. Representative fibril images are shown in panels a and b of Figure 4-1 (TEM images) and panels e and f of Figure 4-1 (AFM images). Figure 4-1d (TEM image) and Figure 4-1h (AFM image) show the Aβ(1–40) aggregates at a Cu(II):Aβ molar ratio of 6:1. At this Cu(II) ion concentration, only amorphous aggregates rather than well-ordered fibrils exist. When the peptide was prepared with a Cu(II):Aβ molar ratio of 2:1, both linear fibrils and granular amorphous aggregates were observed (cf. Figure 4-1c, g). Note that in Figure 4-1g the fibril

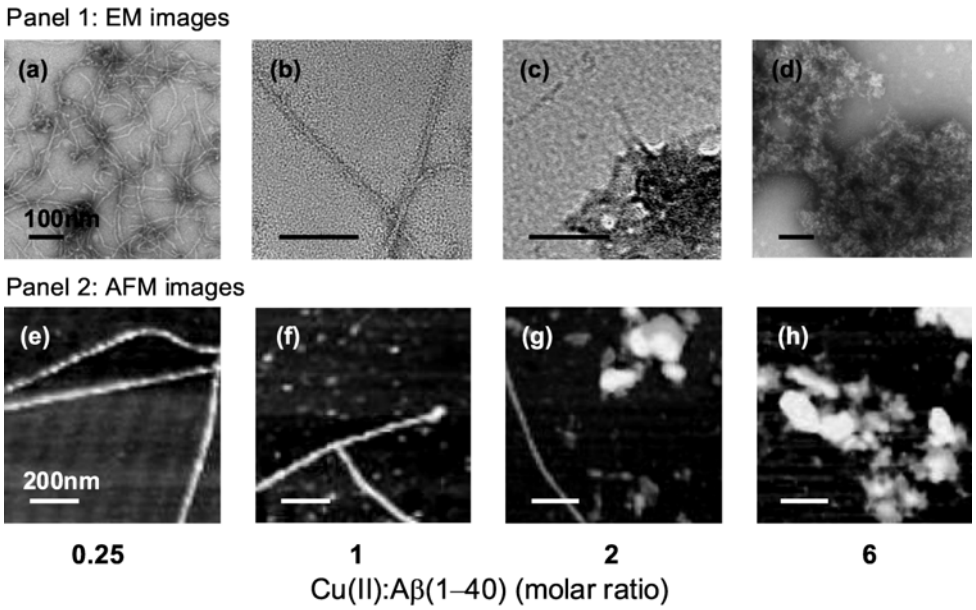

Figure 4-1: (a–d) TEM images of aggregated Aβ(1–40) with Cu(II):Aβ ratios of (a) 0.25:1, (b) 1:1, (c) 2:1, and (d) 6:1. The scale bar is 100 nm. (e–h) Corresponding AFM images of aggregated Aβ(1–40) with Cu(II):Aβ ratios of (e) 0.25:1, (f) 1:1, (g) 2:1, and (h) 6:1. The scale bar is 200 nm. The aggregates are prepared in NEM buffer, and the images suggest a significant increase in the proportion of granular amorphous aggregates as the concentration of Cu(II) is increased.

structure is not as clear as the Aβ fibrils in Figures 4-1e, f because the amorphous aggregates have relatively higher heights than the fibrils. These images suggest that the change in the morphology of aggregated Aβ(1–40) in NEM buffer, with an increasing Cu(II) ion concentration, is quite similar to that of the Aβ in Tris buffer, which has been reported previously (*123*).

The use of AFM complements imaging by TEM and has an advantage in that samples do not have to be either stained with heavy metals or visualized under high-vacuum conditions. In particular, AFM directly provides three-dimensional images whereas TEM of negatively stained specimens provides projection images that cannot show the detailed three-dimensional morphology of the objects being studied. With this advantage, we have examined the topology of the fibril formed by Aβ(1–40) with a Cu(II):Aβ molar ratio of 1:1 using tapping-mode AFM. Figure 4-2 shows the AFM image of the helical fibril from Aβ(1–40), demonstrating a clearly periodic substructure in the fibril. In a recent paper, Addadi and co-workers determined the fibril handedness for three disease-related amyloids, including Aβ(1–40), using scanning electron microscopy (SEM) and cryo-SEM (*163*). They found that amyloids of Aβ(1–40) invariably form left-handed helical fibrils. Here, we performed AFM to examine whether Cu(II) ions affect the handedness of amyloid fibrils. We observed the suprastructure of a helical fibril from the Aβ(1–40) at a Cu(II):Aβ molar ratio of 1:1. Aβ(1–40) fibrils were characterized by a clearly periodic substructure, spaced at intervals of approximately 25 nm along the Aβ fibril axis (cf. Figure 4-2b). As reported earlier, the difference between the maximum and minimum heights along the axis in the substructure is at least 1 nm (*164, 165*). The fibril has a height of ~ 7 nm and a width of ~ 40 nm. For Aβ(1–40) with Cu(II), the fibril helicity is left-handed, showing that the helix handedness of the peptide is not affected by Cu(II). Recently, scientists have exploited the amyloidogenic property of Aβ in assembling metallic nanowires (*166-168*). The formation of

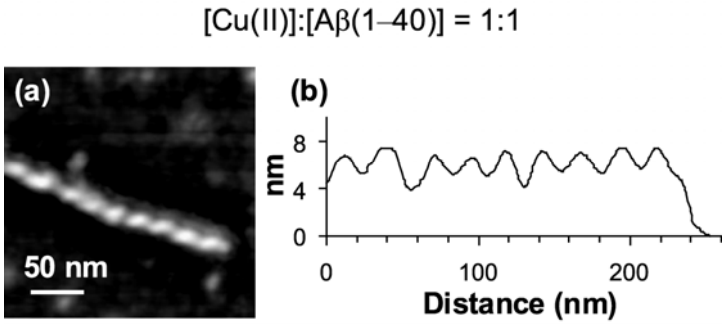

Figure 4-2: (a) AFM image of a helical fibril from Aβ(1–40) at a Cu(II):Aβ ratio of 1:1. (b) Fibril height profile along the fibril axis, showing the regular height variations from the pitch of the fibril with a single repeat period of approximately 25 nm.

fibrils even in the presence of Cu(II) implies that Aβ might be used as a template for the formation of copper nanowires in an appropriate condition.

● *ESEEM spectra of Aβ(1–40) aggregates are dependent on the Cu(II) ion concentration.*

We performed ESEEM experiments on Aβ(1–40) samples containing varying concentrations of Cu(II). ESEEM spectroscopy measures weak hyperfine and quadrupole interactions of the nuclei in the environment (within ~ 10 Å) of the paramagnetic center (*46-48*). Three-pulse ESEEM spectra of the mature aggregated Aβ(1–40) at Cu(II):peptide ratios of (a) 0.25:1, (b) 1:1, (c) 2:1, and (d) 4:1 in NEM buffer are shown in Figure 4-3. All spectra show three narrow peaks at ~ 0.55, ~ 1.04, and ~ 1.46 MHz and a broad peak centered at ~ 4.4 MHz. With increasing Cu(II) ion concentration, a peak at 14.3 MHz also emerges. The three peaks at 0.55, 1.04, and 1.46 MHz are characteristic of a weakly coupled ^{14}N nucleus where the nuclear Zeeman and electron-nuclear hyperfine interaction approximately cancel one another out. Therefore, the energy level splittings are almost completely determined by the ^{14}N nuclear quadrupole interaction (NQI) (*48, 51, 52*). The ESEEM frequencies for these three transitions are given by (*51*)

$$\nu_0 = \frac{2\eta e^2 qQ}{4h}$$

$$\nu_- = \frac{e^2 qQ(3-\eta)}{4h} \qquad (4\text{-}1)$$

$$\nu_+ = \frac{e^2 qQ(3+\eta)}{4h}$$

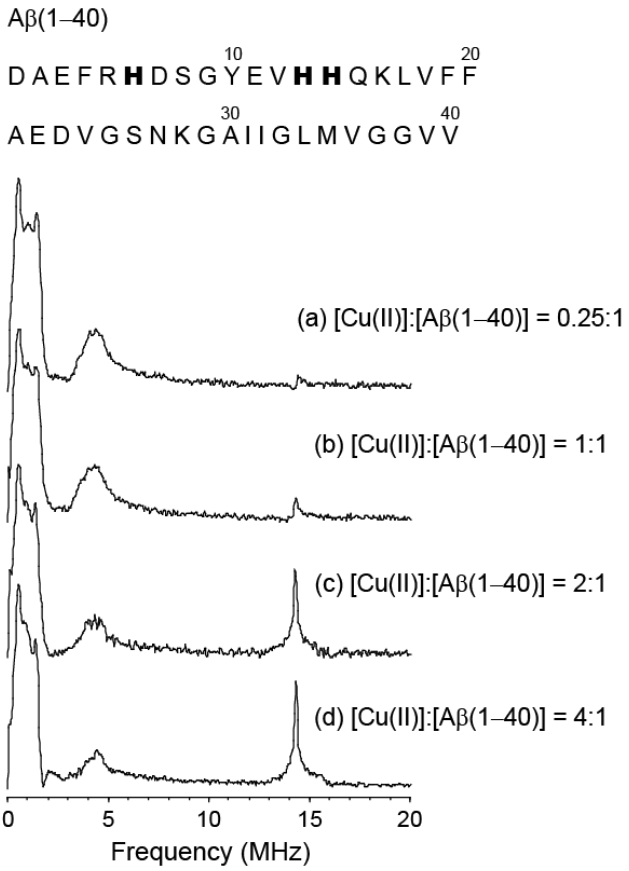

Figure 4-3: Amino acid sequence for Aβ(1–40) and three-pulse ESEEM spectra of aggregated Aβ(1–40) in NEM buffer. The data were collected at Cu(II):peptide ratios of (a) 0.25:1, (b) 1:1, (c) 2:1, and (d) 4:1. Peptide concentrations were 300 μM in all experiments.

where e is the electron charge, q is the z-component of the electric field gradient across the nucleus, Q is the ^{14}N nuclear quadrupole moment, η is the asymmetry parameter, and h is Planck's constant. Use of equation 4-1 to determine the nuclear quadrupole parameters, e^2qQ/h and η, yields values of 1.67 ± 0.08 MHz and 0.66 ± 0.03, respectively.

The broader spectral line at ~ 4.4 MHz arises from the condition in which the nuclear Zeeman and electron–nuclear hyperfine interactions are additive. This frequency is due to a double-quantum (DQ) transition of the remote nitrogen of the imidazole (*46, 48, 53*). Together, the frequencies at or around 0.55, 1.04, and 1.46 MHz as well as the nuclear quadrupole parameters are consistent with histidine coordination.

Several groups have demonstrated that the copper-binding site in Aβ is coordinated by at least two histidine residues (*134, 135, 137, 169*). When the electron spin of the Cu(II) ion interacts with more than one imidazole, the combination frequencies of the three NQI lines may be observed (*46, 48, 170-172*). These peaks, however, have a weak intensity which can be difficult tomeasure, especially in the magnitude mode on samples that display a high degree of heterogeneity (*170*). In Figure 4-3, combination peaks are not clearly seen, which is consistent with our results on truncated sequences of Aβ (*134*). This does not, by itself, rule out the possibility of two or more Cu(II)-coordinating histidine residues (*170*).

At higher Cu(II) ion concentrations, another peak in the ESEEM spectra for Aβ(1–40) with Cu(II) ions is present at 14.3 MHz. This peak is characteristic of interactions between the unpaired electron and proton spins. In Figure 4-3, the proton ESEEM peak may result from the interaction of the Cu(II) ion with remote hydrogen atoms or the axially coordinated water (*51*).

The fundamental peaks from the ESEEM spectra of Aβ(1–40) with Cu(II) ions in NEM buffer are similar to those in Tris buffer, which are described in our previous work (*123*). The

ESEEM spectra of Aβ(1–40) in Tris buffer become broad and heterogeneous as the Cu(II):Aβ molar ratio increases (*123*). The ESEEM spectra of Aβ(1–40) in the NEM buffer show that the intensity of the DQ transition peak at 4.4 MHz is decreased as the Cu(II) ion concentration increases. This result may suggest that the initial multi-histidine coordination for the copper-binding site on the N-terminal region of Aβ(1–40) (cf. Figure 4-3) may be breaking up at a higher Cu(II) concentration because the height of the 4.4 MHz line is proportional to the number of interacting ^{14}N nuclei (*171*). In addition, the proton ESEEM intensity at 14.3 MHz is significantly attenuated relative to that of Aβ(1–40) with Cu(II) ions in Tris buffer at a higher Cu(II) concentration.

Figure 4-4 shows the HYSCORE spectra for Aβ(1–40) assembled at Cu(II):peptide ratios of (a) 1:1, and (b) 2:1. Hyperfine sublevel correlation spectroscopy is a two-dimensional ESEEM technique and provides enhanced resolution of ESEEM spectra that may have broadened lines (*173-175*). As previously assigned in the three-pulse ESEEM spectra, the NQI and DQ transitions for the remote nitrogen of histidine imidazole are obtained. In addition, cross-peaks, (ν_-, ν_{dq}) and (ν_+, ν_{dq}), are observed due to the correlations between the imidazole ^{14}N NQI and DQ transitions for both spectra. The cross-peaks for Aβ(1–40) at a Cu(II):Aβ molar ratio of 2:1 are more diffuse, suggesting a more heterogeneous copper binding environment at the higher Cu(II) concentration.

● *Characterization of the origin of the proton ESEEM peak.*

Recently, our group has reported the ESEEM spectra of Aβ(1–16) with three different molar ratios of Cu(II) ions to the peptide in NEM buffer (*134*). The ESEEM spectra of Aβ(1–16) are quite similar to those of aggregated Aβ(1–40) with an equimolar or subequimolar amount of

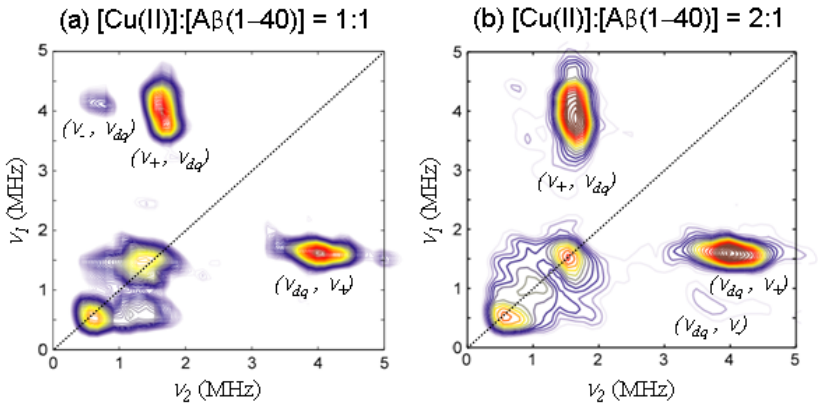

Figure 4-4: HYSCORE spectra of aggregated Aβ(1–40) at Cu(II):peptide ratios of (a) 1:1 and (b) 2:1. The spectra show the correlations between the imidazole ^{14}N nuclear quadrupolar and double-quantum transitions.

Cu(II). The spectra show the three NQI peaks below 2 MHz and a broad DQ transition peak at ~ 4 MHz, indicating that histidine residues coordinate to Cu(II) in both Aβ(1–16) and Aβ(1–40). Aβ(1–16) does not form aggregates and has a soluble form, which is a highly flexible monomer. Therefore, the almost unchanged ESEEM spectra from Aβ(1–16) and the aggregated Aβ(1–40) at an equimolar or subequimolar Cu(II):Aβ ratio suggest that the Aβ fibrils are able to bind Cu(II) ions with a coordination geometry identical to that of monomeric Aβ (*149, 169, 176*). Recently, fluorescence quenching and circular dichroism experiments have revealed that the binding affinity of Cu(II) for the monomeric and fibrillar forms is almost identical. These results also suggest that the fibrillar Aβ has the same Cu(II) coordination geometry as monomeric Aβ (*150*).

When Aβ(1–16) was prepared at a high Cu(II) ion concentration [at a Cu(II):Aβ(1–16) ratio of 4:1], the ESEEM spectrum is almost identical to that of the peptide in the presence of equimolar or subequimolar Cu(II) (*134*), indicating that the primary copper-binding site in Aβ(1–16) is preserved and not significantly affected by the Cu(II) ion concentration (*150*). These ESEEM results do not, by themselves, rule out a second copperbinding site in Aβ(1–16), especially if the second site primarily involves oxygen ligands from aspartate and/or glutamate and non-imidazole nitrogen ligands, which has been suggested by Viles and co-workers (*150*). Also, our CW ESR experimental results for Aβ(1–16) are consistent with their work in that at least two components are present at greater than equimolar Cu(II) concentrations (data not shown). However, the ESEEM results on Aβ(1–16) are in contrast to those of Aβ(1–40), for which the 14.3 MHz proton ESEEM peak in the ESEEM spectra increase at greater than equimolar Cu(II) ion concentrations (cf. Figure 4-3c, d).

To confirm additional copper-binding sites in aggregated Aβ(1–40), we collected

continuous wave (CW) ESR spectra at Cu(II):peptide ratios of 0.25:1, 1:1, 2:1, 4:1, 6:1, and 8:1 have been collected (cf. Figure 4-5a). Double integration of the first-derivative CW ESR spectra was used to identify the number of Cu(II) ions binding to the peptide. As shown in Figure 4-5b, the magnitude of the signal increases linearly and plateaus at 2 equivalents of Cu(II) ions. No significant increase in the intensity of the CW ESR spectrum of Aβ(1–40) at a Cu(II):Aβ ratio of 8:1 is observed. Free Cu(II) ions have a dramatically attenuated ESR signal relative to the Cu(II) bound to Aβ in NEM buffer at pH 7.4 (*46*). Therefore, this data show that Aβ(1–40) binds two Cu(II) ions. A second set of Cu(II) hyperfine peaks at a Cu(II):Aβ(1–40) ratio of 2:1 is observed, and this may be additional evidence of the second copper-binding site in Aβ(1–40). Szalai and co-workers have also reported a second component in CW ESR spectra for both soluble and fibrillar Aβ(1–40) (*169*). Bush and co-workers have demonstrated two cooperative copper-binding sites in Aβ(1–40) at pH 7.4 (*156*). A second copper-binding site of Aβ(1–42) has been revealed in the presence of methanol (20 %, v/v) by Viles and co-workers (*150*). They have suggested that alcohols such as methanol disturb tertiary interactions of the hydrophobic tail and expose some residues that would otherwise be cryptic or hidden (*150, 177*). In the previous paper, they also demonstrated that Aβ(1–28) has two copper-binding sites for a single peptide (*137*).

It is certain that the ESR data are representative of bound copper ions, based on a variety of factors. Different binding affinities of Cu(II) for Aβ peptide, ranging from micromolar to attomolar, have been reported (*178, 179*). To gain information about the fraction of Cu(II) bound to Aβ at equimolar concentrations, the double-integrated intensities of CW ESR spectra obtained at different concentrations, including 300, 150, and 75 μM, were compared (data not shown). The double integration is almost proportional to the concentration, signifying that the fraction of Cu(II) bound to Aβ is not significantly affected by dilution. Also, it is certain that the fraction is

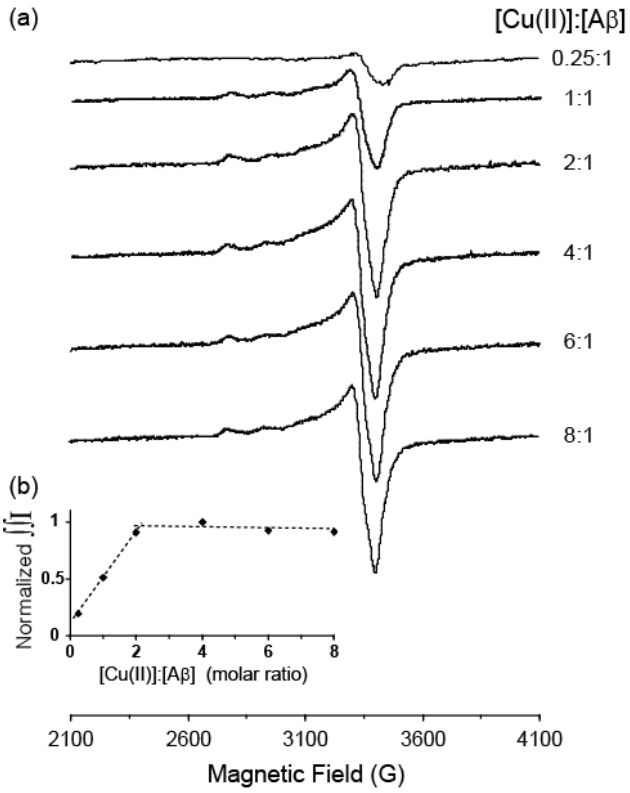

Figure 4-5: (a) The CW ESR spectra obtained at Cu(II):Aβ(1–40) ratios of 0.25:1, 1:1, 2:1, 4:1, 6:1, and 8:1. (b) Double integration of ESR spectra plotted vs the molar ratio of Cu(II) ions to peptide, indicating two Cu(II) ions binding a single Aβ(1–40). The maximum point of the data was normalized to 1. Peptide concentrations were 300 μM in all experiments.

greater than 83 % for the 300 μM sample even if the dissociation constant is the largest reported value (~ 10 μM) for the first binding site (*179*). The dissociation constant of the second binding site has been reported to be on the order of 10 μM (*178*).

The ESEEM and CW ESR results, taken together, indicate that there are two binding sites at high Cu(II) ion concentrations. The binding site for the first molar equivalent of Cu(II) ions is definitely located on the N-terminal region of the peptide, which includes three histidine residues. On the other hand, the second binding site is significantly associated with hydrogen atom(s) (cf. Figure 4-3c, d).

To further investigate the second copper-binding site in Aβ(1–40) and to determine whether the proton ESEEM peak is due to the interaction with solvent protons, the ESEEM spectra were collected on aggregated Aβ(1–40) prepared in D_2O. Figure 4-6 shows three-pulse ESEEM spectra for Aβ(1–40) assembled with a Cu(II):peptide ratio of 2:1 in (a) H_2O and (b) D_2O.

The large 14.3 MHz proton ESEEM peak was eliminated when the solvent was switched to D_2O, and a new peak was observed at ~ 2 MHz as shown in Figure 4-6b. The 2 MHz peak arises from the interaction between deuterium nuclei and the unpaired electron of the Cu(II) ion. The analysis of the ESEEM spectrum with the peptide in D_2O indicates that the second copper-binding site in Aβ(1–40) is in proximity of water or solvent-exchangeable peptide protons. This result is consistent with work by Faller and co-workers (*178*). In addition, a small proton ESEEM peak at 14.3 MHz still remains, which suggests that water may not be the sole source of the oxygen donor in 3N1O Cu(II) coordination in the equatorial plane. Szalai and co-workers also supported the possibility that water is not an equatorial ligand to the Cu(II) ion using CW ESR with the substitution of $H_2{}^{16}O$ with $H_2{}^{17}O$ (*138*).

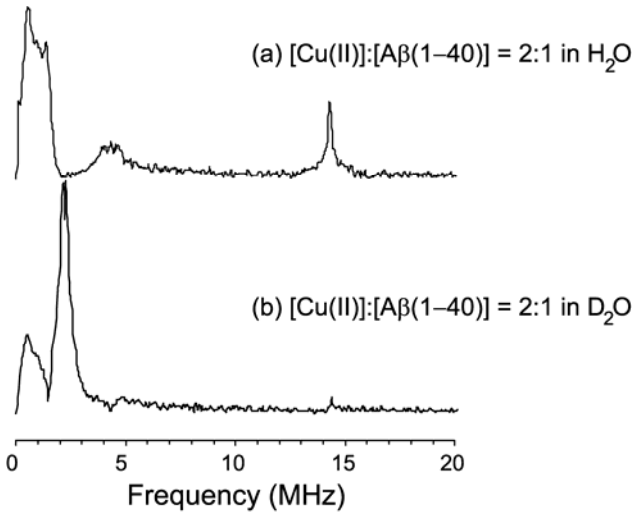

Figure 4-6: Three-pulse ESEEM spectra of Aβ(1–40) assembled with a Cu(II):peptide ratio of 2:1 in (a) H_2O and (b) D_2O. The 14.3 MHz proton ESEEM peak is strongly attenuated, and the deuterium ESEEM peak is observed near 2 MHz in spectrum b.

● *Incubation time dependence of the ESEEM spectra for Aβ(1–40) with Cu(II) ion.*

We investigated the incubation time dependence of the ESEEM spectra for Aβ(1–40) at Cu(II):Aβ(1–40) molar ratios of 1:1 and 2:1. Figure 4-7 shows the ESEEM spectra (a and b) and AFM images (c and d) for Aβ(1–40) at a Cu(II):Aβ(1–40) ratio of 1:1 sampled at 0 h (an initial state) and 10 days (a fully aggregated state). At 0 h, Aβ(1–40) forms dispersed monomers or oligomers, with a very weak ThT fluorescence signal (cf. below and Figure 4-9). After 10 days, the AFM image for Aβ(1–40) aggregates shows mature fibrils (cf. Figure 4-7d). However, there are no significant differences in the peak positions, shapes, or intensities in the ESEEM spectra between monomeric and fibrillar Aβ(1–40), supporting again the possibility that the copper coordination environments in Aβ(1–40) between monomers and mature fibrils are not dramatically different from each other (*149, 150*).

In contrast, the ESEEM spectra for Aβ(1–40) at a Cu(II):Aβ(1–40) ratio of 2:1 have a significant difference in the proton ESEEM peak at 14.3 MHz between the incubation times of 0 h (Figure 4-8a) and 10 days (Figure 4-8b). At 0 h, the Aβ(1–40) at a Cu(II):Aβ(1–40) ratio of 2:1 exhibits the same ESEEM spectrum as Aβ(1–40) at a ratio of 1:1 at 0 h, suggesting that the peptide also exists as monomers or oligomers at the initial point (cf. Figure 4-8a). After 10 days, however, a proton ESEEM peak at 14.3 MHz emerges while the ^{14}N ESEEM peaks below 3 MHz remains practically unchanged, which implies that the second copper-binding site is exposed to a hydrogen-rich condition. In addition, the AFM image for Aβ(1–40) aggregates after 10 days shows mature fibrils and amorphous aggregates together, as shown in Figure 4-8c. Although our results suggest that the second copper-binding site in Aβ(1–40) is exposed to a proton-rich environment, the structure of the binding site is not yet clear and could be elusive to determine because the binding site may form during the aggregation of the peptide.

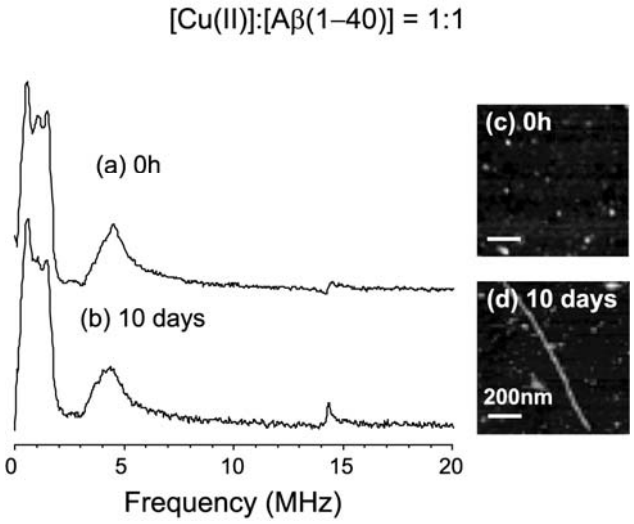

Figure 4-7: (a and b) Three-pulse ESEEM spectra of Aβ(1–40) at a Cu(II):Aβ molar ratio of 1:1 at incubation times of (a) 0 h (an initial state) and (b) 10 days (a fully aggregated state) in NEM buffer. (c and d) AFM images of Aβ(1–40) at incubation times of (c) 0 h and (d) 10 days.

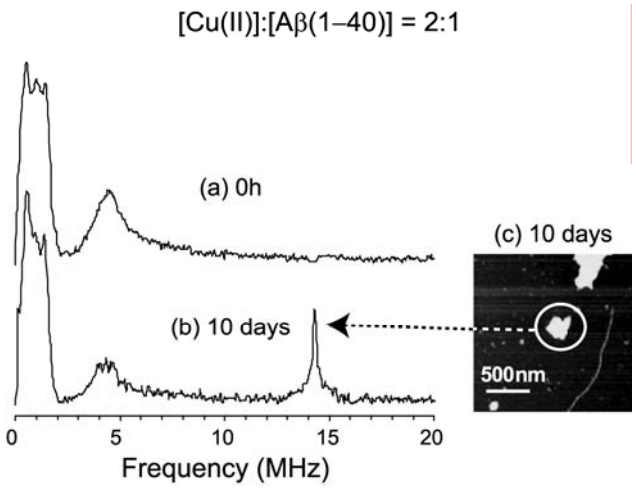

Figure 4-8: Three-pulse ESEEM spectra of Aβ(1–40) at a Cu(II):Aβ molar ratio of 2:1 at incubation times of (a) 0 h (an initial state) and (b) 10 days (a fully aggregated state) in NEM buffer. The proton ESEEM peak at 14.3 MHz emerges in spectrum b. (c) After 10 days, mature fibrils and amorphous aggregates are observed together in an AFM image.

The process of fibril formation involves the interpeptide interaction between two β-sheets in the peptide. At an equimolar Cu(II):Aβ(1–40) ratio, the Cu(II) ion is coordinated with histidine residues on the flexible N-terminal region of Aβ (*134, 135*), providing the characteristic frequencies in the ESEEM spectrum. Therefore, this copper-binding site is not involved with the β-sheet core region and may not affect the interpeptide interaction in order to make a fibril. On the other hand, Aβ(1–40) at a Cu(II):peptide ratio of 2:1 has the second weaker copper-binding site (CW ESR data shown in Figure 4-5) and the site is exposed to water or exchangeable protons on the peptide [ESEEM with Aβ(1–40) in D_2O shown in Figure 4-6]. The second copper-binding site could interfere with the interpeptide interaction in Aβ(1–40), leading to nonfibrillar amorphous aggregates (AFM image shown in Figure 4-8c). Interestingly, Dawson and co-workers have shown that some nanoparticles also inhibit the fibrillization of Aβ by affecting the nucleation step in a concentration-dependent manner (*180*). Thus, it is probable that a relatively high concentration of Cu(II) ions also alters the conformational transition while the nucleation occurs.

● *Effect of Cu(II) ions on the formation of fibrils or amorphous aggregates in Aβ(1–40).*

A simple quantitative analysis for the difference between Aβ(1–40) at Cu(II):Aβ ratios of 1:1 and 2:1 is described in terms of the formation of mature fibrils and amorphous aggregates in Aβ(1–40), respectively. To further investigate this interpretation of the data, we performed a ThT fluorescence assay and a CD experiment.

ThT is a fluorescent dye that specifically binds with the cross β-pleated sheets of amyloid structures (*181, 182*). As shown in Figure 4-9, the fluorescence of ThT for Aβ(1–40) at both Cu(II):Aβ ratios of 1:1 (■) and 2:1 (○) shows a sigmoidal increase with time. The lag time of the

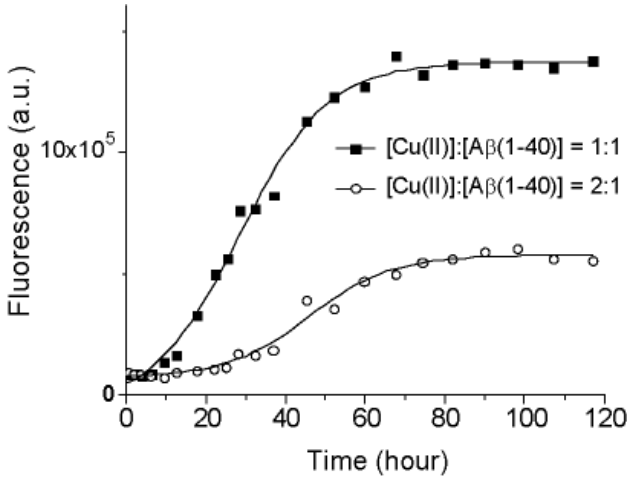

Figure 4-9: Thioflavin T (ThT) fluorescence assays for Aβ(1–40) at Cu(II):Aβ ratios of 1:1 (■) and 2:1 (○) as function of time. An increase of the lag time and a decrease of the amyloid fibril contents are observed at a Cu(II):Aβ ratio of 2:1.

reaction is increased with Aβ(1–40) at a Cu(II):Aβ ratio of 2:1 and the time to proceed to a steady level of fluorescence is also increased with an increase in Cu(II) ion concentration. The final equilibrium level is decreased in Aβ (1–40) at a Cu(II):Aβ ratio of 2:1, indicating that Cu(II) ions may inhibit the fibril formation of the peptide. In Figure 4-1, at a Cu(II):Aβ ratio of 1:1, the TEM and AFM images show the only fibrils that have a linear shape. At a Cu(II):Aβ ratio of 2:1, Aβ(1–40) forms two distinct types of morphologies, linear fibrils and amorphous aggregates. Together, these data suggest that a process that forms granular amorphous aggregates with Cu(II) ions may interfere with the conversion into the fibrillar form.

Using a different assay to assess the β-sheet structure, UV CD spectroscopy, the secondary structure of Aβ(1–40) at two different Cu(II) ion concentrations was monitored. Figure 4-10a shows the CD spectra of Aβ(1–40) at a Cu(II):Aβ molar ratio of 1:1 sampled at an initial state (dashed line) and a fully aggregated state (solid line). The first spectral curve after fibrils have begun to form has a minimum mean residue ellipticity at ~ 200 nm, indicating that the secondary structure of Aβ(1–40) is a random coil at an initial state (*96, 183*). At a fully aggregated state of Aβ(1–40), the CD spectrum has a minimum at ~ 215 nm, which is characteristic of the β-sheet structure (*184, 185*). To examine the conformation with an increased level of β-sheet for Aβ(1–40) at Cu(II):Aβ ratios of 1:1 and 2:1 as a function of time, we monitored a single wavelength, 215 nm. As shown in Figure 4-10b, Aβ(1–40) develops the β-sheet secondary structure at a Cu(II):Aβ ratio of 1:1, supported by a negatively increased mean residue ellipticity at 215 nm in the spectrum. Interestingly, the signal intensity of Aβ(1–40) at 2 molar equivalents of Cu(II) ions to the peptide at 215 nm has a large negative value from the initial point and does not change with time, suggesting that a relatively large amount of β-sheet conformation remains unchanged from the initial state to the end of the aggregation process.

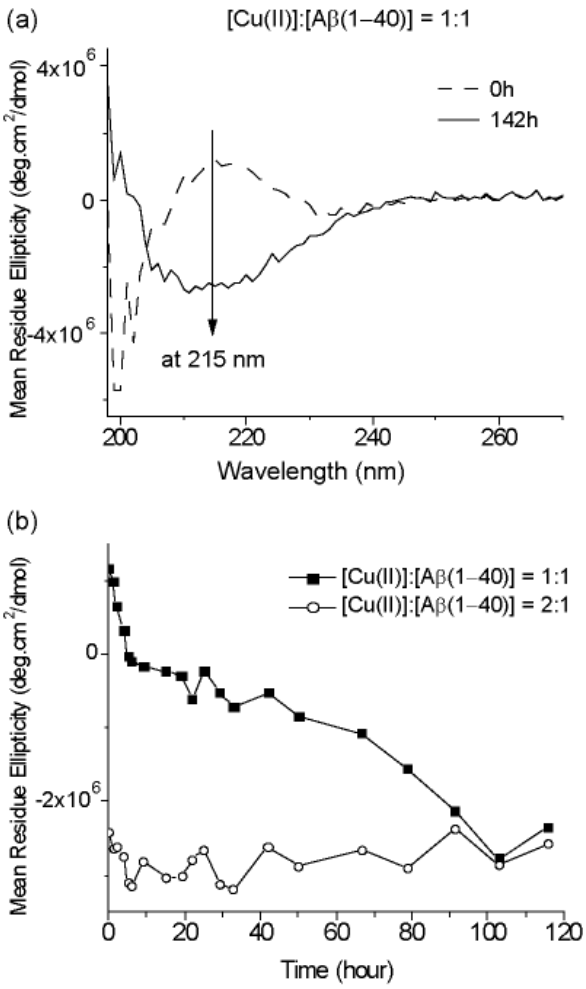

Figure 4-10: (a) UV CD spectra of Aβ(1–40) at a Cu(II):Aβ ratio of 1:1 over time. (b) Mean residue ellipticity at 215 nm as a function of time for Aβ(1–40) at Cu(II):Aβ ratios of 1:1 (■) and 2:1 (○). A decreased mean residue ellipticity at 215 nm indicates the increased level of β-sheet conformation. Peptide concentrations were 28 μM in all experiments.

Using CD spectroscopy, Viles and co-workers have also demonstrated that the secondary structure of the main chain in Aβ becomes more ordered as the Cu(II):peptide ratio increases (*137*). While the CD data can be affected by light scattering caused by large aggregates, the use of a short path length cuvette (0.1 cm) is expected to reduce the chance of scattering. It is also unlikely that the overall qualitative trend in the spectra is significantly altered by light scattering since significant changes are observed over the entire scanned spectral region. The CD data are thus valuable for the qualitative examination of conformational change.

The ThT fluorescence assay and CD experiment measure different aspects of amyloid aggregate formation. The ThT assay directly measures only fibril formation because of the specificity of ThT for amyloid structures; neither monomeric Aβ nor amorphous aggregates significantly enhance the emission intensity of ThT. On the other hand, the CD experiment independently measures the formation of β-sheet structures irrespective of whether the aggregates are amorphous or fibrillar (*186*). When Aβ(1–40) is aggregated at a Cu(II):Aβ ratio of 1:1, the totalamount of β-sheet structure is increased (as measured in the CD experiment) and amyloid fibrils are formed (as measured in the ThT assay) as a function of time. When Aβ(1–40) is aggregated at a Cu(II):Aβ ratio of 2:1, there is a significant amount of β-sheet structure that forms immediately, although there are few amyloid fibrils in the initial part of fibril formation (as measured in the ThT assay or by AFM and TEM). Therefore, in this case, Cu(II) ions induce the aggregates that have the nonfibrillar β-sheet conformation and interfere with the conformational transition into amyloid fibrils.

4.5 SUMMARY

When Aβ(1–40) was prepared in NEM buffer, the AFM and TEM images demonstrated that the aggregation ability of Aβ(1–40) with Cu(II) ions is similar to that of the peptide in Tris buffer. At low concentrations of Cu(II), the aggregates are fibrillar in shape. The presence of Cu(II) ions does not affect the handedness of the Aβ(1–40) helical fibril. At greater than equimolar concentrations of Cu(II) ions, amorphous aggregates result. The ESEEM data for aggregates of Aβ(1–40) in NEM buffer show that as the Cu(II) ion concentration increases the magnitude of the double-quantum ^{14}N ESEEM peak at 4.4 MHz is decreased and the proton ESEEM peak at 14.3 MHz appears. At an equimolar Cu(II):Aβ(1–40) ratio, the Cu(II) ion is coordinated with multi-histidine residues in both monomeric and fibrillar Aβ. The initial copper-binding site breaks up at higher copper concentrations, and a second site that is solvent exposed begins to emerge. In addition, the CW ESR data demonstrate two copper-binding sites in Aβ(1–40). The proton ESEEM peak in Aβ(1–40) at a Cu(II):Aβ ratio of 2:1 was further investigated as the second copper-binding site. The ESEEM experiment with the Aβ(1–40) in D_2O suggests that the second copper-binding site is in the vicinity of water or exchangeable peptide protons. Therefore, the proton ESEEM peaks may be significantly involved in the granular amorphous aggregates of Aβ(1–40), which are shown in the AFM image. ThT fluorescence data also exhibit a weakened ability to form Aβ(1–40) fibrils at 2 equivalents of Cu(II) ions added to the peptide. Taken together, these results suggest that the second copper-binding site in Aβ(1–40) is in the proton-rich environment and interferes with the interpeptide interaction between two different peptide β-sheets, leading to granular amorphous aggregates of the peptide.

4.6 ACKNOWLEDGMENT

The research was supported by an NSF CAREER grant (MCB 0346898) and NSF grant (MCB 0842956). We thank the Peterson Institute of Nanoscience and Engineering (PINSE) for access to a high-resolution field emission transmission electron microscope. We also thank the reviewers for help with the interpretation of some of the changes observed in the ESEEM data.

5.0 SUMMARY

In this research pulsed ESR is applied to measure the average interspin distances between specific sites in order to probe unfolding transition of polyalanine peptides, as well as to gain insight into the role of metal ions in the aggregation of amyloid-β peptide (Aβ).

The alanine-based peptide was synthesized to probe α-helix – random coil protein unfolding transition. Using site-directed spin labeling (SDSL), a methanethiosulfonate spin label (MTSSL) was attached on the cysteine residue. As a doubly spin-labeled peptide, Cu(II), a paramagnetic metal, was coordinated to the well known copper binding sequence, PHGGGW (*46, 53, 95*). The rapidly relaxing electron spin, Cu(II) modulates the electron spin flip rate of nitroxide leading to a reduction in longitudinal relaxation time (T_1) (*26-28*). We measured a value of T_1 in the presence and absence of Cu(II) *at physiological temperatures*, from 270 K to 314 K, by inversion recovery ESR experiment. The enhancement of relaxation rate ($1/T_1$) is used to resolve the average interspin distances, r_{ESR}, between Cu(II) and nitroxide as an alanine-based peptide melts with temperature. The circular dichroism (CD) data demonstrate that the alanine-based peptide has the greatest α-helicity at the lowest temperature and unfolds to random coil structure at higher temperatures. The average distances between Cu(II) and nitroxide decreases from 25 Å in the folded α-helical state to 17 Å in the unfolded state. The results show that the change in interspin distances is clearly in concordance with the change in helicity indicated by CD. Since the molecular dynamic simulation shows an increased distance of the alanine-based

peptide in the PPII geometry, the ESR results suggest that the peptide does not melt into an *extended* PPII structure in the unfolded state. Also, this work describes an application of the pulsed ESR method to monitor unfolding transitions at physiological temperatures in biomolecules.

Electron spin echo envelope modulation (ESEEM) is applied to monitor structural changes associated with misfolding of amyloid-β peptide (Aβ). In Alzheimer's disease (AD), Aβ is the main constituent of the amyloid deposits and a soluble Aβ undergoes a conformational transition into an aggregated, fibrillar form in the misfolding process. We investigated that the copper binding geometry in aggregated Aβ changes with Cu(II) concentration, using three pulse ESEEM method. The three pulse ESEEM experiment detects the modulation of the Cu(II) spin echo from the ^{14}N nuclei (I=1) of surrounding amino acids, and the remote nitrogen of the histidine imidazole provides characteristic frequencies in the ESEEM spectrum (*46, 48, 53*). At low Cu(II):Aβ(1−40) ratios, the ESEEM spectrum shows that the peaks below 2 MHz can be assigned to a nuclear quadrupole interaction (NQI) and the peak around 4 MHz is due to a double quantum (DQ) transition of the remote nitrogen of the histidine imadazole (*46, 48, 53*). This is a direct evidence that Cu(II) is bound to the N-terminal region of Aβ(1–40) that includes three histidines (H6, H13, and H14), as has been also demonstrated by several groups (*134, 135, 137, 169*). As the concentration of Cu(II) increases, these peaks become broader, suggesting that the copper coordination becomes more heterogeneous. Furthermore, a new peak at ~14 MHz becomes observed and dominant. The 14 MHz peak is characteristic of electron-nuclear interactions between the unpaired electron and neighboring proton spins. Transmission electron microscopic (TEM) images of the aggregated state of Aβ(1–40) also demonstrate a transition with an increasing Cu(II) concentration. At low concentrations of Cu(II), the TEM image shows

that Aβ(1–40) forms fibrillar precipitates that have an extensive linear shape, whereas at high Cu(II) concentrations, short and granular aggregates, whose morphologies resemble those of previously described early stage intermediates, are formed (*125, 141*).

Since the continuous-wave (CW) ESR data demonstrate two copper-binding sites in Aβ(1–40), we further investigated the second binding site of the peptide. At a Cu(II):Aβ(1–40) ratio of 1:1, both ESEEM spectra of Aβ(1–40) at 0 h (an initial state) and 10 days (a fully aggregated state) indicate the histidine coordination for the copper-binding site on the N-terminal region of Aβ(1–40). Atomic force microscopy (AFM) images show dispersed monomers or oligomers at 0 h, and mature fibrils at 10 days. This result indicates that the copper coordination environments in Aβ(1–40) between monomers and mature fibrils are not dramatically different each other. In contrast, the ESEEM spectrum for the aggregates of Aβ(1–40) at a Cu(II):Aβ(1–40) ratio of 2:1 shows that the intensity of the DQ transition peak at 4.4 MHz is decreased and the proton ESEEM at 14.3 MHz appears, suggesting that the initial multi-histidine coordination for the copper-binding site breaks up at a higher Cu(II) concentration and a second binding site that is in a proton-rich environment begins to emerge. In addition, the AFM image for the aggregates shows mature fibrils and amorphous aggregates together. Therefore, the proton ESEEM peak may arise from the second copper-binding site, which may be significantly involved in the formation of granular amorphous aggregates. Our ESR and TEM/AFM results demonstrate a correlation between specific Cu(II) coordination and the overall morphology for the aggregated Aβ(1–40). Also, the data suggest that the misfolding mechanism of Aβ(1−40) is strongly dependent on Cu(II) concentration. As a result, this work enhances our understanding of the relationship between the microscopic Cu(II) – Aβ interactions, probed at the atomic level details, and macroscopic structure.

APPENDIX A

CONTRIBUTIONS TO THE ELECTRON SPIN LATTICE RELAXATION RATE

When a spin system is irradiated with the microwave field, the equilibrium population is perturbed. Due to the presence of neighboring spins there exist fluctuating local magnetic fields. These local magnetic fields are time dependent and can therefore induce transitions. Such transitions return the spin system to thermal equilibrium and the process is called spin lattice relaxation.

Microscopically, several mechanisms can contribute to the electron spin lattice relaxation rate ($1/T_{1s}^{0}$). Robinson et al. (*187*) suggested the mechanisms of spin-rotation (SR) interaction, electron-nuclear dipolar (END) interaction, spin diffusion (SD), and Heisenberg exchange by paramagnetic oxygen (OX). Therefore, the total electron spin lattice relaxation rate is given by:

$$\frac{1}{T_{1s}^{\ o}} = \frac{1}{T_{1s}^{\ SR}} + \frac{1}{T_{1s}^{\ END}} + \frac{1}{T_{1s}^{\ SD}} + \frac{1}{T_{1s}^{\ OX}} \qquad \text{(A-1)}$$

where $1/T_{1s}^{SR}$, $1/T_{1s}^{END}$, $1/T_{1s}^{SD}$, and $1/T_{1s}^{OX}$ are the rate of relaxation due to the SR, END, SD, and OX, respectively.

In the presence of another electron spin, the modulation of the electron electron dipolar (EED) interaction provides another mechanism.

$$\frac{1}{T_{1s}} = \frac{1}{T_{1s}^{SR}} + \frac{1}{T_{1s}^{END}} + \frac{1}{T_{1s}^{SD}} + \frac{1}{T_{1s}^{OX}} + \frac{1}{T_{1s}^{EED}} \qquad \text{(A-2)}$$

where $1/T_{1s}^{EED}$ is the rate of relaxation due to the EED. For the peptide, this contribution is just the difference between the experimental relaxation rates of the nitroxide in the absence and the presence of Cu(II). Thus:

$$\left(\frac{1}{T_{1s}} - \frac{1}{T_{1s}^{o}}\right) = \frac{1}{T_{1s}^{EED}} \qquad \text{(A-3)}$$

In principle there are two mechanisms that contribute to $1/T_{1s}^{EED}$. The first is due to the fast relaxation of the paramagnetic metal (cf. equation 2-2 in main text). The second might occur due to modulation of the EED by the overall tumbling of the peptide. The electron spin lattice relaxation rate due to molecular tumbling is defined as (*188*) :

$$\frac{1}{T_{1s}^{EEDR}} = \frac{2}{5}\frac{g^4\beta_e^4}{\hbar^2 r_{ESR}^6} S(S+1)\cdot\left[\frac{\tau_R}{1+\omega^2\tau_R^2} + \frac{4\tau_R}{1+4\omega^2\tau_R^2}\right] \qquad \text{(A-4)}$$

where, g is the g factor, β_e is the Bohr magneton, $\hbar$ is Planck constant (h) divided by 2π, and r_{ESR} is the average interspin distance. Also, ω is the resonant frequency and τ_R is the rotational correlation time of molecule.

If we assume that the enhancement of the spin lattice relaxation rate due to Cu(II) is only due to rotational tumbling of the molecule, $\left(\frac{1}{T_{1s}}-\frac{1}{T_{1s}^{o}}\right)=\frac{1}{T_{1s}^{EEDR}}$. In the case of the proline-based peptide, the values of $\left(\frac{1}{T_{1s}}-\frac{1}{T_{1s}^{o}}\right)$ are determined experimentally (cf. Figure 2-5b in the main text).

To analyze this equation both τ_R and r_{ESR} are required. We anticipate r_{ESR} to be fairly constant for polyproline peptide. Recent, high-field ESR (*189*) and two-dimensional ESR (*43*) results indicate that the ESR lineshapes in such model peptides are mostly dominated by the fast motions of the MTSSL side chain. In particular, Bonora et al. (*43*) determined that the model of microscopic order macroscopic disorder (*190*), wherein the overall tumbling of the biomolecule is slow on the ESR timescale provides a better fit to 2D-ESR results for a smaller peptide (although in a more viscous solvent).

The rotational correlation time, τ_R, for the polyproline peptide may be estimated by using the results of Hanson et al. on a rigid nitroxide TOAC-labeled 16-residue helical peptide in aqueous solution (*191*) and by accounting for the increased volume of this peptide. Based on these results, we estimate that τ_R is 6.1 ns (end-to-end correlation time is 10.2 ns and the parallel one is 2.2 ns) at 274 K. The nitroxyl longitudinal relaxation time (T_{1s}) is weakly dependent on tumbling when τ_R is larger than 3 ns (*187, 192*).

For the polyproline peptide, r_{ESR} is expected to be fairly constant over the temperature range (cf. CD data in Figure A-1a). The temperature dependence of τ_R can be estimated from:

$$\tau_R = \frac{V\eta}{kT} \qquad \text{(A-5)}$$

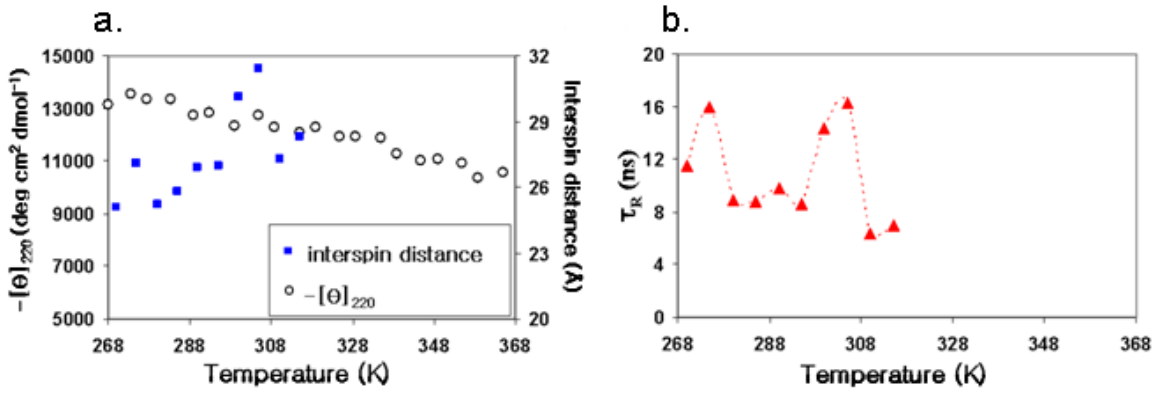

Figure A-1: (a) The estimated interspin distances and (b) rotational correlation time for the proline-based peptide based on modulation of the EED by the overall tumbling of the peptide. The interspin distance, r_{ESR} changes by ~ 6 Å (a) and τ_R does not decreases with temperature (b), indicating that the enhancement of the spin lattice relaxation rate due to Cu(II) may not be due to rotational tumbling of the molecule.

where, V is the volume of the tumbling peptide, η is the viscosity of the solvent, k is the Boltzmann constant, and T is the absolute temperature.

The rotational correlation time, τ_R is estimated to be ~7 ns at 270 K to ~2 ns at 315 K. Therefore, under this assumption, quantitative estimates of r_{ESR} for the proline-based peptide can be obtained by using equation A-4. Over the temperature range, r_{ESR} changes from 25 Å to 31 Å (see Figure A-1a) which is not expected from the stability of the PPII structure in the proline-based peptide (cf. CD results in Figure A-1a).

If we assume a τ_R of 7 ns, and a r_{ESR} of 23 Å (average value expected r_{ESR} for the polyproline data in the main text) $1/T_{1s}^{EEDR}$ overestimates the experimental enhancements by over 65 %. As pointed out by Robinson et al. (*187*), if theory underestimates experimental rates then other mechanisms are possibly involved but if theory overestimates experimental rates then the theory is incorrect. Finally, r_{ESR} was kept fixed and the experimental enhancements and equation A-4 used to measure τ_R. The variation of τ_R obtained using this procedure with temperature is not in accord with expectations, as shown in Figure A-1b (τ_R should decrease monotonically with temperature). Therefore, we anticipate that the rapid T_{1f} of the Cu(II) provides the principle mechanism for the enhancement of nitroxide relaxation rate in these peptides. The distance estimates based on equation 2-2 in the main text are also in good agreement with molecular modeling in the folded state of the peptide and with fluorescence results in the folded and unfolded states (*120*).

BIBLIOGRAPHY

1. Zavoisky, E. (1945) Paramagnetic relaxation of liquid solutions for perpendicular fields. *J. Phys. USSR 9*, 211.

2. Zavoisky, E. (1945) Spin magnetic resonance in paramagnets. *J. Phys. USSR 9*, 245.

3. Kosen, P. A. (1989) Spin labeling of proteins. *Methods in Enzymology 177*, 86-121.

4. Altenbach, C., Marti, T., Khorana, H. G., and Hubbell, W. L. (1990) Transmembrane protein structure: Spin labeling of bacteriorhodopsin mutants. *Science 248*, 1088-1092.

5. Hubbell, W. L., Gross, A., Langen, R., and Lietzow, M. A. (1998) Recent advances in site-directed spin labeling of proteins. *Cur. Op. Struct. Bio. 8*, 649-656.

6. Hubbell, W. L., Cafiso, D. S., and Altenbach, C. (2000) Identifying conformational changes with site-directed spin labeling. *Nature Struct. Bio. 7*, 735-739.

7. Columbus, L., and Hubbell, W. L. (2002) A new spin on protein dynamics. *Trends in Biochemical Sciences 27*, 288-295.

8. Jeschke, G., Wegener, C., Nietschke, M., Jung, H., and Steinhoff, H.-J. (2004) Interresidual distance determination by four-pulse Double Electron-Electron Resonance in an integral membrane protein: The Na^+/proline transporter PutP of *Escherichia coli*. *Biophys. J. 86*, 2551-2557.

9. Hubbell, W. L., and Altenbach, C. (1994) Investigation of structure and dynamics in membrane proteins using site-direxted spin labeling. *Curr. Opin. Struct. Biol. 4*, 566-573.

10. Hubbell, W. L., and Altenbach, C. (1994) Site-directed spin labeling of membrane proteins, in *Membrane Protein Structure: Experimental Approaches* (White, S. H., Ed.), pp 225-249, Oxford University Press.

11. Mchaourab, H. S., Lietzow, M. A., Hideg, K., and Hubbell, W. L. (1996) Motion of Spin-Labeled Side Chains in T4 Lysozyme. Correlation with Protein Structure and Dynamics. *Biochemistry 35*, 7692-7704.

12. Mchaourab, H. S., Oh, K. J., Fang, C. J., and Hubbell, W. L. (1997) Conformation of T4 Lysozyme in Solution. Hinge-Bending Motion and the Substrate-Induced Conformational Transition Studied by Site-Directed Spin Labeling. *Biochemistry 36*, 307-316.

13. Pannier, M., Veit, S., Godt, A., Jeschke, G., and Spiess, H. W. (2000) Dead-time free measurement of dipole-dipole interactions between electron spins. *J. Magn. Reson. 142*, 331-340.

14. Persson, M., Harbridge, J. R., Hammarstrom, P., Mitri, R., Martensson, L. G., Carlsson, U., Eaton, G. R., and Eaton, S. S. (2001) Comparison of electron paramagnetic resonance methods to determine distances between spin labels on human carbonic anhydrase II. *Biophys. J. 80*, 2886-2897.

15. Jeschke, G. (2002) Distance measurements in the nanometer range by pulse EPR. *Chem. Phys. Chem. 3*, 927-932.

16. Borbat, P. P., Mchourab, H. S., and Freed, J. H. (2002) Protein Structure determination using long-distance constraints from double-quantum coherence ESR: Study of T4 Lysozyme. *J. Am. Chem. Soc. 124*, 5304-5314.

17. Narr, E., Godt, A., and Jeschke, G. (2002) Selective measurements of a nitroxide-nitroxide separation of 5 nm and a nitroxide-copper separation of 2.5 nm in a terpyridine based copper(II) complex by pulse EPR spectroscopy. *Angew. Chem. Intl. Ed. 41*, 3907-3910.

18. Jeschke, G. (2002) Determination of the nanostructure of polymer materials by Electron Paramagnetic Resonance spectroscopy. *Macromolecul. Rapid Commun. 23*, 227-246.

19. Schweiger, A., and Jeschke, G. (2001) *Principles of Pulse Electron Paramagnetic Resonance*, Oxford University Press.

20. Saxena, S., and Freed, J. H. (1996) Double quantum Fourier transform electron spin resonance: Distance measurements. *Chem. Phys. Lett. 251*, 102.

21. Saxena, S., and Freed, J. H. (1997) Theory of Double Quantum Two Dimensional Electron Spin Resonance with application to distance measurements. *J. Chem. Phys. 107*, 1317-1340.

22. Borbat, P. P., and Freed, J. H. (1999) Multiple quantum ESR and distance measurements. *Chem. Phys. Lett. 313*, 145-154.

23. Pornsuwan S, Bird, G., Schafmeister, C. E., and Saxena, S. (2006) Flexibility and lengths of bis-peptide nanostructures by ESR. *J. Am. Chem. Soc. 128*, 3876-3877.

24. Bird, G., Pornsuwan S, Saxena, S., and Schafmeister, C. E. (2008) Distance Distributions of End-Labeled Curved Bispeptide Oligomers by Electron Spin Resonance. *ACS Nano 2*, 1857-1864.

25. Stone, K. M., Townsend, J. E., Sarver, J., Sapienza, P. J., Saxena, S., and Jen-Jacobson, L. (2008) Electron Spin Resonance Shows Common Structural Features for Different Classes of EcoRI-DNA Complexes. *Angew. Chem. Int. Ed. 47*, 10192-10194.

26. Kulikov, A. V., and Likhtenshtein, G. I. (1977) The use of spin relaxation phenomena in the investigation of the structure of model and biological systems by the method of spin labels. *Adv. Mol. Relax. and Interact. Proc. 10*, 47-69.

27. Kulikov, A. V., and Likhtenshtein, G. I. (1974) Use of saturation curves for evaluating distances in biological objects by the method of double spin labels. *Biofizika 19*, 420-424.

28. Kulikov, A. V. (1976) Determination of the distance between the spins of the spin-label and paramagnetic center in spin-labeled proteins from the saturation curve parameters of EPR spectra of the labels at 77 K. *Mol. Biol. (Moscow) 10*, 132-141.

29. Levitt, M. (2002) *Spin Dynamics*, John Wiley and Sons, LTD, Chichester.

30. Schwartz, L. J. (1984) Molecular reorientation and time domain electron spin resonance, in *Chemistry*, Cornell University, Ithaca, NY.

31. Schwartz, L. J., Millhauser, G. L., and Freed, J. H. (1986) Two-Dimensional Electron Spin Echoes : Magnetization Transfer And Molecular Dynamics. *Chem. Phys. Lett. 127*, 60-66.

32. Bloembergen, N., Purcell, E. M., and Pound, R. V. (1948) Relaxation Effects in Nuclear Magnetic Resonance Absorption. *Phys. Rev. 73*, 679-712.

33. Bloembergen, N. (1949) On the interaction of nuclear spins in a crystalline lattice. *Physica 15*, 386-426.

34. Bloembergen, N., Shapiro, S., Pershan, P. S., and Artman, J. O. (1959) Cross-relaxation in spin system. *Phys. Rev. 114*, 445-459.

35. Seiter, M., Budker, V., Du, J.-L., Eaton, G. R., and Eaton, S. S. (1998) Interspin distances determined by time domain EPR of spin-labeled high-spin methemoglobin. *Inorganica Chimica Acta 273*, 354-366.

36. Rakowsky, M. H., Zecevic, A., Eaton, G. R., and Eaton, S. S. (1998) Determination of High-Spin Iron(III)-Nitroxyl Distances in Spin-Labeled Porphyrins by Time-Domain EPR. *J. Magn. Reson. 131*, 97-110.

37. Zhou, Y., Bowler, B. E., Lynch, K., Eaton, S. S., and Eaton, G. R. (2000) Interspin distances in spin-labeled Metmyoglobin variants determined by Saturation Recovery EPR. *Biophys. J. 79*, 1039-1052.

38. Borbat, P. P., Crepeau, R. H., and Freed, J. H. (1997) Multifrequency two-dimensional Fourier transform ESR: An X/Ku-Band spectrometer. *J. Magn. Reson. 127*, 155-167.

39. Freed, J. H. (2000) New technologies in Electron Spin Resonance. *Annual Review of Physical Chemistry 51*, 655-689.

40. Borbat, P. P., Costa-Filho, A. J., Earle, K. A., Moscicki, J. K., and Freed, J. H. (2001) Electron spin resonance in studies of membranes and proteins. *Science 291*, 266-269.

41. Costa-Filho, A. J., Shimoyama, Y., and Freed, J. H. (2003) A 2D-ELDOR Study of the Liquid Ordered Phase in Multilamellar Vesicle Membranes. *Biophys. J. 84*, 2619-2633.

42. Costa-Filho, A. J., Crepeau, R. H., Borbat, P. P., Ge, M., and Freed, J. H. (2003) Lipid-Gramicidin Interactions: Dynamic Structure of the Boundary Lipid by 2D-ELDOR. *Biophys. J. 84*, 3364-3378.

43. Bonora, M., Pornsuwan, S., and Saxena, S. (2004) Nitroxide-Relaxation over the Entire Motional Range. *J. Phys. Chem. B 108*, 4196-4198.

44. Calle, C., Eichel, R.-A., Finazzo, C., Forrer, J., Granwehr, J., Gromov, I., Groth, W., Harmer, J., Kalin, M., Lammler, W., Liesum, L., Madi, Z., Stoll, S., Doorslaer, S. V., and Schweiger, A. (2001) Electron Paramagnetic Resonance Spectroscopy. *Chimia 55*, 763-766.

45. Peisach, J., and Blumberg, W. E. (1974) Structural implications derived from the analysis of Electron Paramagnetic Resonance spectra of natural and artificial copper proteins. *Arch. Biochem. Biophys. 165*, 691-708.

46. Aronoff-Spencer, E., Burns, C. S., Avdievich, N. I., Gerfen, G. J., Peisach, J., Antholine, W. E., Ball, H. L., Cohen, F. E., Prusiner, S. B., and Millhauser, G. L. (2000) Identification of the Cu^{2+} binding sites in the N-terminal domain of the Prion protein by EPR and CD spectroscopy. *Biochemistry 39*, 13760-13771.

47. Mims, W. B. (1972) Envelope modulation in spin echo experiments. *Phys. Rev. B 5*, 2409-2419.

48. Mims, W. B., and Peisach, J. (1978) The nuclear modulation effect in electron spin echoes for complexes of Cu^{2+} and imidazole with ^{14}N and ^{15}N. *J. Chem. Phys. 69*, 4921-4930.

49. Mims, W. B. (1972) Amplitudes of superhyperfine frequencies displayed in the electron spin-echo envelope. *Phys. Rev. B 6*, 3543-3545.

50. McCracken, J., Pember, S., Benkovic, S. J., Villafranca, J. J., Miller, R. J., and Peisach, J. (1988) Electron spin-echo studies of the copper binding site in phenylalanine hydroxylase from Chromobacterium violaceum. *J. Am. Chem. Soc. 110*, 1069-1074.

51. Dikanov, S. A., Tsvetkov, Y. D., Bowman, M. K., and Astashkin, A. V. (1982) Parameters of Quadrupole Coupling of 14N Nuclei in Chlorophyll a Cations Determined by the Electron Spin Echo Method. *Chem. Phys. Lett. 90*, 149-153.

52. Deligiannakis, Y., Louloudi, M., and Hadjiliadis, N. (2000) Electron spin echo envelope modulation (ESEEM) spectroscopy as a tool to investigate the coordination environment of metal centers. *Coordin. Chem. Rev. 204*, 1-112.

53. Burns, C. S., Aronoff-Spencer, E., Dunham, C. M., Lario, P., Avdievich, N. I., Antholine, W. E., Olmstead, M. M., Vrielink, A., Gerfen, G. J., Peisach, J., Scott, W. G., and Millhauser, G. L. (2002) Molecular features of the copper binding sites in the octarepeat domain of the Prion protein. *Biochemistry 41*, 3991-4001.

54. Dikanov, S. A., and Tsvetkov, Y. D. (1992) *Electron Spin Echo Envelope Modulation (ESEEM) Spectroscopy*, CRC Press, Boca Raton.

55. Jun, S., Becker, J. S., Yonkunas, M., Coalson, R., and Saxena, S. (2006) Unfoldig of Alanine-Based Peptides Using Electron Spin Resonance Distance Measurements. *Biochemistry 45*, 11666-11673.

56. Larson, R. G., and Singel, D. J. (1993) Double electron-electron resonance spin-echo modulation spectroscopic measurement of electron-spin pair separations in orientationally disordered solids. *J. Chem. Phys. 98*, 5134-5146.

57. Rabenstein, M. D., and Shin, Y. K. (1995) Determination of the distance between spin labels attached to a macromolecule. *Proc. Natl. Acad. Sci. 92*, 8239-8243.

58. Martin, R. E., Pannier, M., Diederich, F., Gramlich, V., Hubrich, H., and Spiess, H. W. (1998) Determination of end-to-end distances in a series of TEMPO diradicals of up to 2.8 nm length with a new four-pulse double electron electron resonance experiment. *Angew. Chem. Intl. Ed. 37*, 2834-2837.

59. Jeschke, G., Pannier, M., Godt, A., and Spiess, H. W. (2000) Dipolar spectroscopy and spin alignment in electron paramagnetic resonance. *Chem. Phys. Lett. 331*, 243-252.

60. Milov, A. D., Tsvetkov, Y. D., Formaggio, F., Crisma, M., Toniolo, C., and Raap, J. (2000) Self-Assembling properties of membrane-modifying peptides studied by PELDOR and CW-ESR spectroscopies. *J. Am. Chem. Soc. 122*, 3843-3848.

61. Eaton, S. S., Moore, K. M., Sawant, B. M., and Eaton, G. R. (1983) Use of the EPR half-field transition to determine the interspin distance and orientation of the interspin vector in systems of two unpaired electrons. *J. Am. Chem. Soc. 105*, 6560-6567.

62. Hustedt, E. J., and Beth, A. H. (1999) Nitroxide spin-spin interactions: Applications to protein structure and dynamics. *Annu. Rev. Biophys. Biomol. Struct. 28*, 129-153.

63. Pannier, M., Schadler, V., Schops, M., Wiesner, U., Jeschke, G., and Spiess, H. W. (2000) Determination of ion cluster sizes and cluster-to-cluster distances in ionomers by four-pulse double electron-electron resonance. *Macromolecules 33*, 7812-7818.

64. Altenbach, C., Oh, K.-J., Trabanino, R. J., Hideg, K., and Hubbell, W. L. (2001) Estimation of inter-residue distances in spin labeled proteins at physiological

temperatures: Experimental strategies and practical limitations. *Biochemistry 40*, 15471-15482.

65. Milov, A. D., Tsvetkov, Y. D., Formaggio, F., Crisma, M., Toniolo, C., and Raap, J. (2001) The secondary structure of a membrane-modifying peptide in a supramolecular assembly studied by PELDOR and CW-ESR spectroscopies. *J. Am. Chem. Soc. 123*, 3784-3789.

66. Liu, Y.-S., Sompornpisut, P., and Perozo, E. (2001) Structure of the KcsA channel intracellular gate in the open state. *Nature Struct. Bio. 8*, 883-887.

67. Perozo, E., Cortes, D. M., Sompornpisut, P., Kloda, A., and Martinac, B. (2002) Open channel structure of MscI and the gating mechanism of mechanosensitive channels. *Nature 418*, 942-948.

68. Schiemann, O., Weber, A., Edwards, T., Prisner, T., and Sigurdsson, S. (2003) Nanometer distance measurements on RNA using PELDOR. *J. Am. Chem. Soc. 125*, 3434-3435.

69. Kweon, D.-H., Kim, C. S., and Shin, Y.-K. (2003) Regulation of neuronal SNARE assembly by the membrane. *Nature Struct. Bio. 10*, 440-447.

70. Bonora, M., Becker, J. S., and Saxena, S. (2004) Suppression of electron spin-echo envelope modulation peaks in double quantum coherence electron spin resonance. *J. Magn. Reson. 170*, 278-283.

71. Borbat, P. P., Davis, J. H., Butcher, S. E., and Freed, J. H. (2004) Measurement of Large Distances in Biomolecules Using Double-Quantum Filtered Refocused Electron Spin-Echoes. *J. Am. Chem. Soc. 126*, 7746-7747.

72. Schiemann, O., Piton, N., Mu, Y., Stock, G., Engels, J. W., and Prisner, T. F. (2004) A PELDOR-based nanometer distance ruler for oligonucleotides. *J. Am. Chem. Soc. 126*, 5722-5729.

73. Xu, Y., Zhang, F., Su, Z., McNew, J. A., and Shin, Y.-K. (2005) Hemifusion in SNARE-mediated membrane fusion. *Nature Struct. Mol. Bio. 12*, 417-422.

74. Subczynski, W. K., Hyde, J. S., and Kusumi, A. (1989) Oxygen Permeability of Phosphatidylcholine-Cholesterol Membranes. *Proc. Natl. Acad. Sci. 86*, 4474-4478.

75. Subczynski, W. K., Pasenkiewicz-Gierula, M., McElhaney, R. N., Hyde, J. S., and Kusumi, A. (2003) Molecular Dynamics of 1-Palmitoyl-2-oleoylphosphatidylcholine Membranes Containing Transmembrane -Helical Peptides with Alternating Leucine and Alanine Residues. *Biochemistry 42*, 3939-3948.

76. Nielsen, R. D., Che, K., Gelb, M. H., and Robinson, B. H. (2005) A Ruler for Determining the Position of Proteins in Membranes. *J. Am. Chem. Soc. 127*, 6430-6442.

77. Milov, A. D., Salikhov, K. M., and Tsvetkov, Y. D. (1972) Spin-lattice relaxation of hydrogen atoms and paramagnetic ions in glassy aqueous solutions of sulfuric acid at 77.deg.K. *Fizika Tverd. Tela 14*, 2211-2215.

78. Rakowsky, M. H., More, K. M., Kulikov, A. V., Eaton, G. R., and Eaton, S. S. (1995) Time-Domain Electron Paramagnetic Resonance as a Probe of Electron-Electron Spin-Spin Interaction in Spin-Labeled Low-Spin Iron Porphyrins. *J. Am. Chem. Soc. 117*, 2049-2057.

79. Voss, J., Hubbell, W. L., and Kaback, H. R. (1995) Distance determination in proteins using designed metal ion binding sites and site-directed spin labeling: application to the lactose permease of Escherichia coli. *Proc. Natl. Acad. Sci. 92*, 12300-12303.

80. Pappu, R. V., and Rose, G. D. (2002) A simple model for polyproline II structure in unfolded states of alanine-based peptides. *Protein Science 11*, 2437-2455.

81. Eker, F., Cao, X., Nafie, L., and Schweitzer-Stenner, R. (2002) Tripeptides Adopt Stable Structures in Water. A Combined Polarized Visible Raman, FTIR, and VCD Spectroscopy Study. *J. Am. Chem. Soc. 124*, 14330-14341.

82. Shi, Z., Olson, C. A., Rose, G. D., Baldwin, R. L., and Kallenbach, N. R. (2002) Polyproline II structure in a sequence of seven alanine residues. *Proc. Natl. Acad. Sci. 99*, 9190-9195.

83. Maiti, N. C., Apetri, M. M., Zagorski, M. G., Carey, P. R., and Anderson, V. E. (2004) Raman Spectroscopic Characterization of Secondary Structure in Natively Unfolded Proteins: alpha-Synuclein. *J. Am. Chem. Soc. 126*, 2399-2408.

84. Schweitzer-Stenner, R., Eker, F., Griebenow, K., Cao, X., and Nafie, L. A. (2004) The Conformation of Tetraalanine in Water Determined by Polarized Raman, FT-IR, and VCD Spectroscopy. *J. Am. Chem. Soc. 126*, 2768-2776.

85. Eker, F., Griebenow, K., Cao, X., Nafie, L. A., and Schweitzer-Stenner, R. (2004) Preferred peptide backbone conformations in the unfolded state revealed by the structure analysis of alanine-based (AXA) tripeptides in aqueous solution. *Proc. Natl. Acad. Sci. 101*, 10054-10059.

86. Asher, S. A., Mikhonin, A. V., and Bykov, S. (2004) UV Raman Demonstrates that alpha-Helical Polyalanine Peptides Melt to Polyproline II Conformations. *J. Am. Chem. Soc. 126*, 8433-8440.

87. Zaman, M. H., Shen, M.-Y., Berry, R. S., Freed, K. F., and Sosnick, T. R. (2003) Investigations into Sequence and Conformational Dependence of Backbone Entropy, Inter-basin Dynamics and the Flory Isolated-pair Hypothesis for Peptides. *J. Mol. Biol. 331*, 693-711.

88. Mu, Y., Kosov, D. S., and Stock, G. (2003) Conformational Dynamics of Trialanine in Water. 2. Comparison of AMBER, CHARMM, GROMOS, and OPLS Force Fields to NMR and Infrared Experiments. *J. Phys. Chem. B 107*, 5064-5073.

89. Garcia, A. E. (2004) Characterization of non-alpha helical conformations in Ala peptides. *Polymer 45*, 669-676.

90. Smyth, E., Syme, C. D., Blanch, E. W., Hecht, L., Vasak, M., and Barron, L. D. (2001) Solution Structure of Native Proteins with Irregular Folds from Raman Optical Activity. *Biopolymers 58*, 138-151.

91. Rucker, A. L., and Creamer, T. P. (2002) Polyproline II helical structure in protein unfolded states: Lysine peptides revisited. *Protein Science 11*, 980-985.

92. Tiffany, M. L., and Krimm, S. (1968) New chain conformations of poly(glutamic acid) and polylysine. *Biopolymers 6*, 1379-1382.

93. Woody, R. W. (1992) Circular dichroism and conformation of unordered polypeptides. *Adv. Biophys. Chem. 2*, 37-79.

94. Zagrovic, B., Lipfert, J., Sorin, E. J., Millett, I. S., vanGunsteren, W. F., Doniach, S., and Pande, V. S. (2005) Unusual compactness of a polyproline type II structure. *Proc. Natl. Acad. Sci. 102*, 11698-11703.

95. Millhauser, G. L. (2004) Copper binding in the Prion protein. *Accounts of Chemical Research 37*, 79-85.

96. Holzwarth, G., and Doty, P. (1965) The Ultraviolet Circular Dichroism of Polypeptides. *J. Am. Chem. Soc. 87*, 218-228.

97. Young, M. A., and Pysh, E. S. (1975) Vacuum Ultraviolet Circular Dichroism of Poly(L-proline) I and II. *J. Am. Chem. Soc. 97*, 5100-5103.

98. Kelly, M. A., Chellgren, B. W., Rucker, A. L., Troutman, J. M., Fried, M. G., Miller, A.-F., and Creamer, T. P. (2001) Host-Guest Study of Left-Handed Polyproline II Helix Formation. *Biochemistry 40*, 14376-14383.

99. Lii, J. H., and Allinger, N. L. (1991) The MM3 Force Field for Amides, Polypeptides and Proteins. *J. Comput. Chem. 12*, 186-199.

100. MacKerell, A. D. (1998) Developments in the CHARMM all-atom empirical energy function for biological molecules., in *216th ACS National Meeting of the American Chemical Society*, J. Am. Chem. Soc., Boston, MA.

101. Barone, V., Bencini, A., Cossi, M., Matteo, A. D., Mattesini, M., and Totti, F. (1998) Assessment of a combined QM/MM approach for the study of large nitroxide systems in vacuo and in condensed phases. *J. Am. Chem. Soc. 120*, 7069-7078.

102. Humphrey, W., Dalke, A., and Schulten, K. (1996) VMD: visual molecular dynamics. *J. Mol. Graph. 14*, 33-38.

103. Kale, L., Skeel, R., Bhandarkar, M., Brunner, R., Gursoy, A., Krawetz, N., Phillips, J., Shinozaki, A., Varadarajan, K., and Schulten, K. (1999) NAMD2: Greater scalability for parallel molecular dynamics. *J. Comput. Phys. 151*, 283-312.

104. Hoover, W. G. (1985) Canonical dynamics: Equilibrium phase-space distributions. *Phys. Rev. A 31*, 1695-1697.

105. Millhauser, G. L. (1992) Selective placement of electron spin labels: new structural methods for peptides and proteins. *Trends in Biochemical Sciences 17*, 448-452.

106. Gaponenko, V., Howarth, J. W., Columbus, L., Gasmi-Seabrook, G., Yuan, J., Hubbell, W. L., and Rosevear, P. R. (2000) Protein global fold determination using site-directed spin and isotope labeling. *Protein Science 9*, 302-309.

107. Becker, J. S., and Saxena, S. (2005) Double Quantum Coherence electron spin resonance on coupled Cu(II)-Cu(II) spins. *Chem. Phys. Lett. 414*, 248-252.

108. Lee, S., Budil, D. E., and Freed, J. H. (1994) Theory of two-dimensional Fourier - transform electron spin resonance for ordered and viscous fluids. *J. Chem. Phys. 101*, 5529-5558.

109. Voss, J., Salwinski, L., Kaback, H. R., and Hubbell, W. L. (1995) A method for distance determination in proteins using a designed metal ion binding site and site-directed spin labeling: Evaluation with T4 lysozyme. *Proc. Natl. Acad. Sci. 92*, 12295-12299.

110. Eaton, S. S., and Eaton, G. R. (2000) Biological Magnetic Resonance, in *Distance Measurements in Biological Systems by EPR* (Berliner, L. J., Eaton, S. S., and Eaton, G. R., Eds.), pp 29-154, Kluwer Academic/Plenum Publisher, New York.

111. Schuler, B., Lipman, E. A., Steinbach, P. J., Kumke, M., and Eaton, W. A. (2005) Polyproline and the "spectroscopic ruler" revisited with single-molecule fluorescence. *Proc. Natl. Acad. Sci. 102*, 2754-2759.

112. Greenfield, N., and Fasman, G. D. (1969) Computed Circular Dichroism Spectra for the Evaluation of Protein Conformation. *Biochemistry 8*, 4108-4116.

113. Chen, Y.-H., and Yang, J. T. (1971) A new approach to the calculation of secondary structures of globular proteins by optical rotatory dispersion and circular dichroism. *Biochem. Biophys. Res. Commun. 44*, 1285-1291.

114. Bierzynski, A., and Baldwin, R. L. (1982) Local secondary structure in ribonuclease A denatured by guanidine • HCl near 1 °C. . *J. Mol. Biol. 162*, 173-186.

115. Chiang, Y.-W., Borbat, P. P., and Freed, J. H. (2005) The determination of pair distance distributions by pulsed ESR using Tikhonov regularization. *J. Magn. Reson. 172*, 279-295.

116. Todd, A. P., and Millhauser, G. L. (1991) ESR spectra reflect local and global mobility in a short spin-labeled peptide throughout the alpha helix-coil transition. *Biochemistry 30*, 5515-5523.

117. Cantor, C. R. (1980) Biophysical Chemistry, in *Biophysical Chemistry* (Cantor, C. R., and Schimmel, P. R., Eds.), W. H. Freeman, San Francisco.

118. Chen, Y.-H., Yang, J. T., and Martinez, H. M. (1972) Determination of the secondary structures of proteins by circular dichroism and optical rotatory dispersion. *Biochemistry 11*, 4120-4131.

119. Lednev, I. K., S.Karnoup, A., Sparrow, M. C., and Asher, S. A. (1999) alpha-Helix Peptide Folding and Unfolding Activation Barriers: A Nanosecond UV Resonance Raman Study. *J. Am. Chem. Soc. 121*, 8074-8086.

120. Gnanakaran, S., Hochstrasser, R. M., and Garcia, A. E. (2004) Nature of structural inhomogeneities on folding a helix and their influence on spectral measurements. *Proc. Natl. Acad. Sci. 101*, 9229-9234.

121. Voss, J., Wu, J., Hubbell, W. L., Jacques, V., Meares, C. F., and Kaback, H. R. (2001) Helix Packing in the Lactose Permease of Escherichia coli: Distances between Site-Directed Nitroxides and a Lanthanide. *Biochemistry 40*, 3184-3188.

122. Voss, J., Hubbell, W. L., and Kaback, H. R. (1998) Helix Packing in the Lactose Permease Determined by Metal-Nitroxide Interaction. *Biochemistry 37*, 211-216.

123. (a) Jun, S., and Saxena, S. (2007) The aggregated state of amyloid-β peptide in vitro depends on Cu^{2+} concentration. *Angew. Chem. Int. Ed. 46*, 3959-3961. (b) Jun, S., and Saxena, S. (2007) The aggregated state of amyloid-β peptide in vitro depends on Cu^{2+} concentration. *Angew. Chem. Int. Ed. 46*, 5263.

124. Klein, W. L., Jr., W. B. S., and Teplow, D. B. (2004) Small assemblies of unmodified amyloid beta-protein are the proximate neurotoxin in Alzheimer's disease. *Neurobiol. Aging 25*, 569-580.

125. Tabner, B. J., El-Agnaf, O. M. A., Turnbull, S., German, M. J., Paleologou, K. E., Hayashi, Y., Cooper, L. J., Fullwood, N. J., and Allsop, D. (2005) Hydrogen peroxide is generated during the very early stages of agregation of the amyloid peptides implicated in Alzheimer disease and familial british dementia. *J. Biol. Chem. 280*, 35789-35792.

126. Bush, A. I., Pettingell, W. H., Multhaup, G., Paradis, M. d., Vonsattel, J.-P., Gusella, J. F., Beyreuther, K., Masters, C. L., and Tanzi, R. E. (1994) Rapid induction of Alzheimer Aβ amyloid formation by zinc. *Science 265*, 1464-1467.

127. Zou, J., Kajita, K., and Sugimoto, N. (2001) Cu^{2+} Inhibits the Aggregation of Amyloid β-Peptide(1–42) in vitro. *Angew. Chem. Int. Ed. 40*, 2274-2277.

128. Miura, T., Suzuki, K., Kohata, N., and Takeuchi, H. (2000) Metal Binding Modes of Alzheimer's Amyloid-β Peptide in Insoluble Aggregates and Soluble Complexes. *Biochemistry 39*, 7024-7031.

129. Yoshiike, Y., Tanemura, K., Murayama, O., Akagi, T., Murayama, M., Sato, S., Sun, X., Tanaka, N., and Takashima, A. (2001) New Insights on How Metals Disrupt Amyloid β-Aggregation and Their Effects on Amyloid-β Cytotoxicity. *J. Biol. Chem. 276*, 32293-32299.

130. Raman, B., Ban, T., Yamaguchi, K. I., Sakai, M., Kawai, T., Naiki, H., and Goto, Y. (2005) Metal Ion-dependent Effects of Clioquinol on the Fibril Growth of an Amyloid β Peptide. *J. Biol. Chem. 280*, 16157-16162.

131. Lovell, M. A., Robertson, J. D., Teesdale, W. J., Campbell, J. L., and Markesbery, W. R. (1998) Copper, iron and zinc in Alzheimer's disease senile plaques. *J. Neurol. Sci. 158*, 47-52.

132. Atwood, C. S., Moir, R. D., Huang, X., Scarpa, R. C., Bacarra, N. M. E., Romano, D. M., Hartshorn, M. A., Tanzi, R. E., and Bush, A. I. (1998) Dramatic Aggregation of Alzheimer Aβ by Cu(II) Is Induced by Conditions Representing Physiological Acidosis. *J. Biol. Chem. 273*, 12817-12826.

133. Sengupta, P., Garai, K., Sahoo, B., Shi, Y., Callaway, D. J. E., and Maiti, S. (2003) The Amyloid β Peptide ($A\beta_{1-40}$) Is Thermodynamically Soluble at Physiological Concentrations. *Biochemistry 42*, 10506-10513.

134. Shin, B.-k., and Saxena, S. (2008) Direct Evidence That All Three Histidine Residues Coordinate to Cu(II) in Amyloid-β_{1-16}. *Biochemistry 47*, 9117-9123.

135. Drew, S. C., Noble, C. J., Masters, C. L., Hanson, G. R., and Barnham, K. J. (2009) Pleomorphic Copper Coordination by Alzheimer's Disease Amyloid-β Peptide. *J. Am. Chem. Soc. 131*, 1195-1207.

136. Kowalik-Jankowska, T., Ruta, M., Wisniewska, K., and Lankiewiez, L. (2003) Coordination abilities of the 1-16 and 1-28 fragments of beta-amyloid peptide towards copper(II) ions : a combined potentiometric and spectroscopic study. *J. Inorg. Biochem. 95*, 270-282.

137. Syme, C. D., Nadal, R. C., Rigby, S. E. J., and Viles, J. H. (2004) Copper Binding to the Amyloid-β(Aβ) Peptide Associated with Alzheimer's Disease. *J. Biol. Chem. 279*, 18169-18177.

138. Karr, J. W., Akintoye, H., Kaupp, L. J., and Szalai, V. A. (2005) N-Terminal Deletions Modify the Cu^{2+} Binding Site in Amyloid-β. *Biochemistry 44*, 5478-5487.

139. Hou, L., and Zagorski, M. G. (2006) NMR Reveals Anomalous Copper(II) Binding to the Amyloid Aβ Peptide of Alzheimer's Disease. *J. Am. Chem. Soc. 128*, 9260-9261.

140. Kulik, L. V., Grigoryev, I. A., Salnikov, E. S., Dzuba, S. A., and Tsvetkov, Y. D. (2003) Electron Spin-Echo Envelope Modulation induced by slow intramolecular motion. *J. Phys. Chem. A 107*, 3692-3695.

141. Walsh, D. M., Lomarkin, A., Benedek, G. B., and Condron, M. M. (1997) Amyloid-β protein fibrillogenesis. *J. Biol. Chem. 272*, 22364-22372.

142. Dong, J., Shokes, J. E., Scott, R. A., and Lynn, D. G. (2006) Modulating Amyloid Self-Assembly and Fibril Morphology with Zn(II). *J. Am. Chem. Soc. 128*, 3540-3542.

143. Stellato, F., Menestrina, G., Serra, M. D., Potrich, C., Tomazzolli, R., Meyer-Klaucke, W., and Morante, S. (2006) Metal binding in amyloid β-peptides shows intra- and inter-peptide coordination modes. *Eur. Biophy. J. 35*, 340-351.

144. Jun, S., Gillespie, J. R., Shin, B.-k., and Saxena, S. (2009) The Second Cu(II)-Binding Site in a Proton-Rich Environment Interferes with the Aggregation of Amyloid-β(1−40) into Amyloid Fibrils. *Biochemistry 48*, 10724-10732.

145. Hardy, J., and Selkoe, D. J. (2002) The amyloid hypothesis of Alzheimer's disease: Progress and problems on the road to therapeutics. *Science 297*, 353-356.

146. McLaurin, J., and Chakrabartty, A. (1996) Membrane Disruption by Alzheimer β-Amyloid Peptides Mediated through Specific Binding to either Phospholipids or Gangliosides: Implications for Neurotoxicity. *J. Biol. Chem. 271*, 26482-26489.

147. Lambert, M. P., Barlow, A. K., Chromy, B. A., Edwards, C., Freed, R., Liosatos, M., Morgan, T. E., Rozovsky, I., Trommer, B., Viola, K. L., Wals, P., Zhang, C., Finch, C. E., Krafft, G. A., and Klein, W. L. (1998) Diffusible, Nonfibrillar Ligands Derived from $A\beta_{1-42}$ are Potent Central Nervous System Neurotoxins. *Proc. Natl. Acad. Sci. U.S.A. 95*, 6448-6453.

148. Carrotta, R., Manno, M., Bulone, D., Martorana, V., and San Biagio, P. L. (2005) Protofibril Formation of Amyloid β-Protein at Low pH via a Non-cooperative Elongation Mechanism. *J. Biol. Chem. 280*, 30001-30008.

149. Karr, J. W., Kaupp, L. J., and Szalai, V. A. (2004) Amyloid-β Binds Cu^{2+} in a Mononuclear Metal Ion Binding Site. *J. Am. Chem. Soc. 126*, 13534-13538.

150. Sarell, C. J., Syme, C. D., Rigby, S. E. J., and Viles, J. H. (2009) Copper(II) Binding to Amyloid-β Fibrils of Alzheimer's Disease Reveals a Picomolar Affinity: Stoichiometry and Coordination Geometry Are Independent of Aβ Oligomeric Form *Biochemistry 48*, 4388-4402.

151. Hilbich, C., Kisters-Woike, B., Reed, J., Masters, C. L., and Beyreuther, K. (1992) Substitutions of hydrophobic amino acids reduce the amyloidogenicity of Alzheimer's disease βA4 peptides. *J. Mol. Biol. 228*, 460-473.

152. Soreghan, B., Kosmoski, J., and Glabe, C. (1994) Surfactant properties of Alzheimer's Aβ peptides and the mechanism of amyloid aggregation. *J. Biol. Chem. 269*, 28551-28554.

153. Tammie L. S. Benzinger, David M. Gregory, Timothy S. Burkoth, Hélène Miller-Auer, David G. Lynn, Robert E. Botto, and Meredith, S. C. (2000) Two-Dimensional Structure of β-Amyloid(10-35) Fibrils. *Biochemistry 39*, 3491-3499.

154. Lu, K., Jacob, J., Thiyagarajan, P., Conticello, V. P., and Lynn, D. G. (2003) Exploiting Amyloid Fibril Lamination for Nanotube Self-Assembly. *J. Am. Chem. Soc. 125*, 6391-6393.

155. Gordon, D. J., Balbach, J. J., Tycko, R., and Meredith, S. C. (2004) Increasing the Amphiphilicity of an Amyloidogenic Peptide Changes the β-Sheet Structure in the Fibrils from Antiparallel to Parallel. *Biophys. J. 86*, 428-434.

156. Atwood, C. S., Scarpa, R. C., Huang, X., Moir, R. D., Jones, W. D., Fairlie, D. P., Tanzi, R. E., and Bush, A. I. (2000) Characterization of Copper Interactions with Alzheimer Amyloid β Peptides: Identification of an Attomolar-Affinity Copper Binding Site on Amyloid β1–42. *J. Neurochem. 75*, 1219-1233.

157. Smith, D. P., Ciccotosto, G. D., Tew, D. J., Fodero-Tavoletti, M. T., Johanssen, T., Masters, C. L., Barnham, K. J., and Cappai, R. (2007) Concentration Dependent Cu^{2+} Induced Aggregation and Dityrosine Formation of the Alzheimer's Disease Amyloid-β Peptide. *Biochemistry 46*, 2881-2891.

158. Fauth, J. M., Schweiger, A., Braunschweiler, A., Forrer, J., and Ernst, R. R. (1986) Elimination of Unwanted Echoes and Reduction of Dead Time in Three-Pulse Electron Spin-Echo Spectroscopy. *J. Magn. Reson. 66*, 74-85.

159. Gemperle, C., Aebli, G., Schweiger, A., and Ernst, R. R. (1990) Phase Cycling in Pulse EPR. *J. Magn. Reson. 88*, 241-256.

160. Hasegawa, K., Yamaguchi, I., Omata, S., Gejyo, F., and Naiki, H. (1999) Interaction between Aβ(1−42) and Aβ(1−40) in Alzheimer's β-Amyloid Fibril Formation in Vitro. *Biochemistry 38*, 15514-15521.

161. Harris, J. R., and Agutter, P. S. (1970) A negative staining study of human erythrocyte ghosts and rat liver nuclear membranes. *J. Ultrastruct. Res. 33*, 219-232.

162. http://rsb.info.nih.gov/ij.

163. Rubin, N., Perugia, E., Goldschmidt, M., Fridkin, M., and Addadi, L. (2008) Chirality of amyloid suprastructures. *J. Am. Chem. Soc. 130*, 4602-4603.

164. Wong, S. S., Harper, J. D., Lansbury, P. T., Jr., and Lieber, C. M. (1998) Carbon Nanotube Tips: High-Resolution Probes for Imaging Biological Systems. *J. Am. Chem. Soc. 120*, 603-604.

165. Harper, J. D., Wong, S. S., Lieber, C. M., and Peter T. Lansbury, J. (1999) Assembly of Aβ amyloid protofibrils: An in vitro model for a possible early event in Alzheimer's disease. *Biochemistry 38*, 8972-8980.

166. Morgan, D. M., Dong, J., Jacob, J., Lu, K., Apkarian, R. P., Thiyagarajan, P., and Lynn, D. G. (2002) Metal Switch for Amyloid Formation: Insight into the Structure of the Nucleus. *J. Am. Chem. Soc. 124*, 12644-12645.

167. Hamada, D., Yanagihara, I., and Tsumoto, K. (2004) Engineering amyloidogenicity towards the development of nanofibrillar materials. *Trends Biotechnol. 22*, 93-97.

168. Dong, J., Canfield, J. M., Mehta, A. K., Shokes, J. E., Tian, B., Childers, W. S., Simmons, J. A., Mao, Z., Scott, R. A., Warncke, K., and Lynn, D. G. (2007) Engineering metal ion coordination to regulate amyloid fibril assembly and toxicity. *Proc. Natl. Acad. Sci. U.S.A. 104*, 13313-13318.

169. Karr, J. W., and Szalai, V. A. (2008) Cu(II) Binding to Monomeric, Oligomeric, and Fibrillar Forms of the Alzheimer's Disease Amyloid-β Peptide. *Biochemistry 47*, 5006-5016.

170. Kosman, D. J., Peisach, J., and Mims, W. B. (1980) Pulsed Electron Paramagnetic Resonance Studies of the Cu(II) Site in Galactose Oxidase. *Biochemistry 19*, 1304-1308.

171. McCracken, J., Pember, S., Benkovic, S. J., Villafranca, J. J., Miller, R. J., and Peisach, J. (1988) Electron-Spin-Echo Studies of the Copper Binding Site in Phenylalanine Hydroxylase from Chromobacterium violaceum. *J. Am. Chem. Soc. 110*, 1069-1074.

172. Jiang, F., McCracken, J., and Peisach, J. (1990) Nuclear quadrupole interactions in copper(II)-diethylenetriamine-substituted imidazole complexes and in copper(II) proteins. *J. Am. Chem. Soc. 112*, 9035-9044.

173. Ponti, A., and Schweiger, A. (1995) Nuclear Coherence-Transfer Echoes in Pulsed EPR. *J. Chem. Phys. 102*, 5207-5219.

174. Kofman, V., Shane, J. J., Dikanov, S. A., Bowman, M. K., Libman, J., Shanzer, A., and Goldfarb, D. (1995) Coordination of Cu(II) to Lipophilic Bis-hydroxamate Binders As studied by One- and Two- Dimensional Electron Spin Echo Spectroscopy. *J. Am. Chem. Soc. 117*, 12771-12778.

175. Kofman, V., Farver, O., Pecht, I., and Goldfarb, D. (1996) Two-Dimensional Pulsed EPR spectroscopy of the Copper Protein Azurin. *J. Am. Chem. Soc. 118*, 1201-1206.

176. Antzutkin, O. N. (2004) Amyloidosis of Alzheimer's Aβ peptides: Solid-state nuclear magnetic resonance, electron paramagnetic resonance, transmission electron microscopy,

scanning transmission electron microscopy and atomic force microscopy studies. *Magn. Reson. Chem. 42*, 231-246.

177. Kony, D. B., Hunenberger, P. H., and van Gunsteren, W. F. (2007) Molecular dynamics simulations of the native and partially folded states of ubiquitin: Influence of methanol cosolvent, pH, and temperature on the protein structure and dynamics. *Protein Sci. 16*, 1101-1118.

178. Guilloreau, L., Damian, L., Coppel, Y., Mazarguil, H., Winterhalter, M., and Faller, P. (2006) Structural and thermodynamical properties of Cu^{II} amyloid-β16/28 complexes associated with Alzheimer's disease. *J. Biol. Inorg. Chem. 11*, 1024-1038.

179. Tougu, V., Karafin, A., and Palumaa, P. (2008) Binding of zinc(II) and copper(II) to the full-length Alzheimer's amyloid-β peptide. *J. Neurochem. 104*, 1249-1259.

180. Cabaleiro-Lago, C., Quinlan-Pluck, F., Lynch, I., Lindman, S., Minogue, A. M., Thulin, E., Walsh, D. M., Dawson, K. A., and Linse, S. (2008) Inhibition of Amyloid β Protein Fibrillation by Polymeric Nanoparticles. *J. Am. Chem. Soc. 130*, 15437-15443.

181. LeVine, H., III. (1993) Thioflavin T interaction with synthetic Alzheimer's disease β-amyloid peptides: Detection of amyloid aggregation in solution. *Protein Sci. 2*, 404-410.

182. Castillo, G. M., Ngo, C., Cummings, J., Wright, T. N., and Snow, A. D. (1997) Perlecan Binds to the β-Amyloid Proteins (Aβ) of Alzheimer's Disease, Accelerates Aβ Fibril Formation, and Maintains Aβ Fibril Stability. *J. Neurochem. 69*, 2452-2465.

183. Perczel, A., and Hollosi, M. (1996) Turns, in *Circular Dichroism and the Conformational Analysis of Biomolecules* (Fasman, G. D., Ed.), pp 285-367, Plenum Press, New York.

184. Greendield, N. J. (2006) Using circular dichroism spectra to estimate protein secondary structure. *Nature protocols 1*, 2876-2890.

185. Whitmore, L., and Wallace, B. A. (2008) Protein secondary structure analyses from circular dichroism spectroscopy: methods and reference databases. *Biopolymers 89*, 392-400.

186. Benseny-Cases, N., Cocera, M., and Cladera, J. (2007) Conversion of non-fibrillar β-sheet oligomers into amyloid fibrils in Alzheimer's disease amyloid peptide aggregation. *Biochem. Biophys. Res. Commun. 361*, 916-921.

187. Robinson, B. H., Haas, D. A., and Mailer, C. (1994) Molecular Dynamics in Liquids: Spin-Lattice Relaxation of Nitroxide Spin Labels. *Science 263*, 490-493.

188. Abragam, A. (1961) The principles of Nuclear Magnetism, in *The principles of Nuclear Magnetism* (Adair, R. K., Edwards, S. F., Ehrenreich, H., smith, C. H. L., and Rees, M., Eds.), pp 264-353, Oxford University Press, New York.

189. Bennati, M., Gerfen, G. J., Martinez, G. V., Griffin, R. G., Singel, D. J., and Millhauser, G. L. (1999) Nitroxide Side-Chain Dynamics in a Spin-Labeled Helix-Forming Peptide Revealed by High-Frequency (139.5-GHz) EPR Spectroscopy. *Journal of Magnetic Resonance 139*, 281-286.

190. Meirovitch, E., Nayeem, A., and Freed, J. H. (1984) Analysis of protein-lipid interactions based on model simulations of electron spin resonance spectra. *J. Phys. Chem 88*, 3454-3465.

191. Hanson, P., Anderson, D. J., Martinez, G., Millhauser, G., Formaggio, F., Crisma, M., Toniolo, C., and Vita, C. (1998) Electron spin resonance and structural analysis of water soluble, alanine-rich peptides incorporating TOAC. *Molecular Physics 95*, 957-966.

192. Owenius, R., Terry, G. E., Williams, M. J., Eaton, S. S., and Eaton, G. R. (2004) Frequency Dependence of Electron Spin Relaxation of Nitroxyl Radicals in Fluid Solution. *J. Phys. Chem. B 108*, 9475-9481.